NEW MATERIALS FOR PHOTOCONDUCTIVE TERAHERTZ ANTENNAS

Dissertation

zur

Erlangung des Doktorgrades der Naturwissenschaften

(Dr. rer. nat.)

dem Fachbereich Physik

der Philipps-Universität Marburg

vorgelegt von

Oday M. Abdulmunem

aus Bagdad / Irak

Marburg, 2017

.

Vom Fachbereich Physik der Philipps-Universität Marburg

als Dissertation angenommen am:

Erstgutachter: Prof. Dr. Martin Koch

Zweitgutacher: Prof. Dr. Martin Hofmann

Tag der mündlichen Prüfung: 19.10.2017

Hochschulkennziffer: 1180

Abstract

In this thesis, we have first introduced a new setup for the reliable characterization of photoconductive antennas to be used in THz time-domain spectroscopy. Using this setup one can benchmark THz antennas with high precision. The intra-day reproducibility error is in the range of 1.9% while the reproducibility within 9 days is 2.6%. This includes not only absolute power stability but also reproducibility of the spectra by eliminating alignment errors that alter the transfer function from sender to receiver. In order to demonstrate the full capabilities of the system, we investigated samples from five LT-GaAs wafers, grown at temperatures between 200°C and 300°C, in a systematic manner. The obtained results are in good agreement with previous studies on the same material system. These results prove that the system allows for quality control of photoconductors with minimum comparison error.

We have also investigated the correlation between THz emission strength and the surface properties of the LT-GaAs photoconductive antenna. The THz characteristics were measured with the highly stable setup mentioned above, which allowed exciting a 10-mm long CPS antenna along the gap without changing the alignment of the optical or THz beam path. The surface properties were quantified regarding roughness and grain size. The roughness was extracted from AFM measurements and the grain size from SEM measurements. A comparison of the THz emission strength in form of the peak-to peak THz amplitude and the surface properties showed a strong nonlinear correlation: a smaller grain size and a smoother surface increase the THz amplitude. These results can be used in the future to optimize the performance of THz antennas.

Additionally, we have successfully prepared TiN-nanoparticles using ultrasonic and pulsed laser ablation techniques. The two techniques provide with a different distribution of Zeta-potential and particle size. Within our experimental conditions, pulsed laser ablation can give lower particle size and greater Zeta-potential. TiN-nanoparticles prepared by these techniques have a high and flat absorbance in the spectral range 600 -1000 nm. LT-GaAs covered with dispersed TiN-nanoparticles has enhanced THz emission when the average particle size is about 62 nm.

More investigations are needed on how to develop preparation and deposition techniques in such a way that control the shape, size, distance between the particles. This may lead to a further improvement of the THz power emitted from such devices.

Finally, we demonstrated that coating with $MnFe_2O_4$ nanoparticles could be used to improve the performance of photoconductive antennas in the THz region. Our experiments demonstrate that coatings with $MnFe_2O_4$–particles provided a new approach to increase the photocurrent density on silicon under CW illumination. In order to understand the effect of $MnFe_2O_4$ nanoparticles on photo-excited silicon, a semiconductor model was proposed to describe this phenomenon. We used this model to calculate the transmission amplitudes of THz pulses transmitted through bare silicon substrates and silicon substrates covered by $MnFe_2O_4$ nanoparticles under laser irradiation with different powers. Because the effect of $MnFe_2O_4$ nanoparticles on silicon significantly provides an enhanced attenuation of terahertz wave, silicon substrates covered by $MnFe_2O_4$ nanoparticles have the potential to be used as an optical modulator in the THz region. This may lead to a cost-efficient component for THz systems operating in transmission mode. Furthermore, $MnFe_2O_4$ nanoparticles could be used for the implementation of novel optical devices.

Zusammenfassung

In dieser Arbeit wird ein neuartiger Aufbau für die zuverlässige Charakterisierung photoleitender Antennen vorgestellt, welche im Bereich der THz-Zeitbereichsspektroskopie verwendet werden. Der Aufbau ermöglicht die Vermessung von THz-Antennen mit hoher Genauigkeit. Die Reproduzierbarkeit der Messergebnisse lässt sich für Messungen innerhalb eines Tages mit einem Fehler im Bereich von 1,9% beziffern. Über eine Zeitspanne von 9 Tagen beträgt der Fehler 2,6%. Dies umfasst nicht nur die Stabilität der absoluten THz-Leistung, sondern auch die Reproduzierbarkeit des Spektrums, die durch die Vermeidung von Justagefehlern, welche die Transferfunktion zwischen Sender und Empfänger verändern würden, sichergestellt wird. Zur Demonstration des vollen Leistungsumfangs des Systems wurden Proben von insgesamt fünf LT-GaAs-Wafern, welche bei Temperaturen zwischen 200°C und 300°C gewachsen wurden, in systematischer Weise untersucht. Die so erzielten Ergebnisse liegen in guter Übereinstimmung mit den Ergebnissen früherer Untersuchungen an demselben Materialsystem. Diese Ergebnisse zeigen, dass das System den Vergleich und die Qualitätskontrolle von Halbleiterproben bei einem minimalen Fehler erlaubt.

Des weiteren wurde die Korrelation zwischen der Stärke des emittierten THz-Signals und den Oberflächeneigenschaften der photoleitenden Antennen auf LT-GaAs-Basis untersucht. Die THz-Eigenschaften wurden mit dem oben erwähnten hochstabilen Messaufbau untersucht, welcher es ermöglicht eine 10mm lange CPS-Antenne entlang des "Gap" anzuregen ohne, dass ein Nachjustieren des THz-Pfads oder des optischen Pfads erfolgt. Die Oberflächeneigenschaften wurden durch die Bestimmung der Rauigkeit und Korngröße quantifiziert. Der Vergleich des emittierten THz-Signals gemessen an seiner Peak-to-Peak-Amplitude und der Oberflächeneigenschaften zeigte eine starke nichtlineare Korrelation: Eine kleinere Korngröße und eine glattere Oberfläche vergrößern die THz-Amplitude. Diese Ergebnisse können in der Zukunft verwendet werden, um die Leistung von THz-Antennen zu optimieren.

In einem weiteren Versuch kamen TiN-Nanopartiekl zum Einsatz, welche durch Ultraschall und gepulste Laser-Ablation hergestellt wurden. Die mittels dieser zwei Techniken hergestellten Nanopartikel besitzen verschiedene Verteilungen des Zeta-Potentials und der Partikelgröße. In den durchgeführten Experimenten zeigten die mittels gepulste Laser-Ablation hergestellten Partikel eine kleinere Partikelgröße und ein höheres Zeta-Potential. TiN-Nanopartikel, die mittels dieser Technik hergestellt wurden, weisen eine starke und zugleich flache Absorption im Spektralbereich von 600-1000 nm auf. LT-GaAs-Proben, welche mit TiN-Nanopartikeln beschichtet wurden, weisen eine erhöhte THz-Emission auf, wenn die Partikelgröße in etwa 62 nm beträgt. Gegenstand weiterer Untersuchungen sollte die Entwicklung einer Technik zur Vorbereitung und Aufbringung der Nanopartikel sein, welche eine Kontrolle der Form, der Größe und des Abstands zwischen den Partikeln erlaubt. Auf diese Weise könnte die von derartigen Bauelementen abgestrahlte THz-Leistung weiter gesteigert werden.

Schließlich wurde gezeigt, dass eine Beschichtung mit $MnFe_2O_4$-Nanopartikeln sich leistungssteigernd auf photoleitende Antennen im THz-Frequenzbereich auswirken kann. Die Experimente zeigen, dass die Beschichtung mit $MnFe_2O_4-$Partikeln einen neuartigen Ansatz darstellt, um die Photostromdichte in Silizium unter kontinuierlicher Anregung zu erhöhen. Zum Verständnis der Auswirkungen von $MnFe_2O_4$-Nanopartikeln auf optisch angeregtes Silizium wur-de ein Modell zur Beschreibung des Phänomens entwickelt. Dieses Modell kommt zum Einsatz, um die transmittierte Amplitude von THz-Pulsen zu berechnen, welche durch pures Silizium transmittiert wurden, und solchen, welche durch mit $MnFe_2O_4$-Nanopartikeln beschichtetes Silizium transmittiert wurden, wobei die Leistung der optischen Anregung variiert wurde. Aufgrund des Effekts, dass sich die Absorption des THz-Signals in den mit $MnFe_2O_4$ beschichteten Silizium-Proben mit der optischen Anregung erhöht, besitzen diese Proben das Potenzial als optischer Modulator im THz-Frequenzbereich verwendet zu werden. Dies könnte zu einem preisgünstigen Bauelement für in Transmissionsgeometrie arbeitende THz-Systeme führen. Außerdem könnten $MnFe_2O_4$-Nanopartikel in neuartigen optischen Bauelementen Verwendung finden.

Acknowledgments

Contents

Chapter 1

Introduction

1.1 The Terahertz Frequency Range

Terahertz (THz) radiation is located in the spectral region $\sim 0.1 - 10$ THz $\sim 3\,mm - 30\,\mu m$, between the millimeter and infrared ranges of the electromagnetic spectrum [1]. Compared with microwave and infrared waves, the wavelength of THz radiation is longer than the infrared wavelength and shorter than the microwave wavelength. As shown in Figure 1.1, a frequency of 10^{12} Hz (1 THz) corresponds to a wavelength of 300 μm (wave-number about 33 cm^{-1} and a period of 1 ps. This wavelength has a photon energy of 4.1 meV which is equivalent to a thermal energy at a temperature of 48 Kelvin [2]
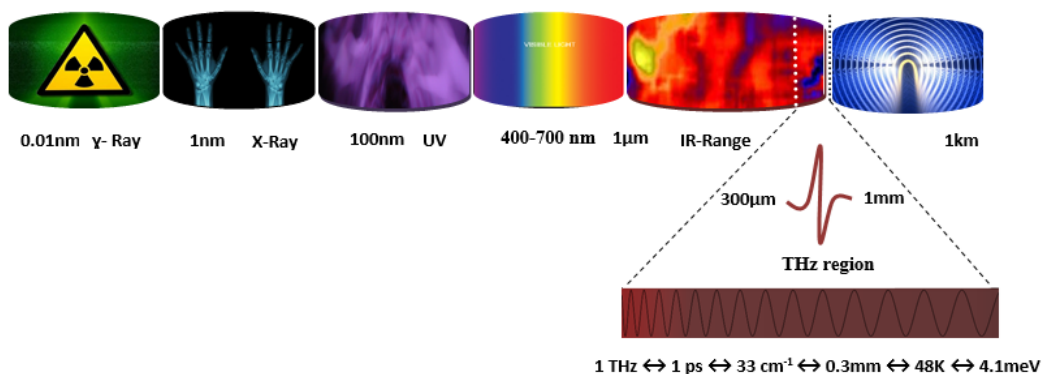
Figure 1.1: Spectrum of electromagnetic radiation with terahertz waves lies between the infrared and microwaves' wavelengths in the range 1mm - 300 μm [3]

1.2 Features of THz waves

Since the THz region lies between the area of millimeter waves and infrared radiation, it has mid-characteristics borrowed from the two bands. These properties can be summarized as follows:

1.2.1 Penetration depth

The wavelength of THz radiation is longer than the infrared wavelength; hence, THz waves typically show less scattering and a better penetration depth ($\sim cm$) compared to infrared waves ($\sim \mu m$). Therefore, many dry and non-metallic materials which are mostly transparent in this range are opaque in the visible spectrum [4].

1.2.2 Resolution

THz waves have shorter wavelengths in comparison to the microwave ones; this gives a better spatial imaging resolution. Near-field microscopy has been used to produce images with resolution about ($\dfrac{\lambda}{106}$) in the microwave range [5].

1.2.3 Safety

In contrast to X-rays, the photon energies in the THz band are much lower. THz radiation is non-ionizing and therefore it could be used for safe imaging. Since high water content prevents transmission type imaging, THz transmission mode imaging is only used for dehydrated samples. [6].

1.2.4 Spectral fingerprint

Inter- and intra-vibrational modes of many molecules lie in THz spectroscopic range. It has been proven that THz TDS spectroscopy can be used to investigate bio-molecules such as DNA [7]

and retinal chromophores [8]. TDS systems with ultrashort pulses can be used as spectrometers that cover a broadband range of frequency from 0.1 to 5 THz or wave-numbers from 3 to 167 cm^{-1}. Additionally, a THz-pulse with an ultrashort pulse duration (approximately 1 ps) represents a broadband light source in the far-infrared (FIR) region and this band is also applicable to transient FIR spectroscopy [9].

1.3 THz Applications

Several applications have been identified for THz systems. In summary, THz radiation has important applications in spectroscopy, astronomy, wireless communication, imaging systems and home security. Since the focus of this thesis is on LT-GaAs antennas, THz applications related to materials spectroscopy and imaging are briefly discussed here.

1.3.1 THz Spectroscopy

Numerous materials have significant absorption lines in the THz spectrum. This is because molecules in these materials can absorb particular photon energies located in the THz range. After the absorption of photons, molecules convert photon energies to vibrational and rotational energies. For example, in water the absorption of THz photon can excite librational modes at 1.95 THz and 6 THz respectively [10]. In ammonia, the absorption of THz evolves rotational modes at 0.572, 1.168 and 1.763 THz [11]. Because of these features, THz spectroscopy became a powerful technique to characterize material properties or check material constituents [12], examine multi-layered materials such as art and clothes which are transparent in THz frequencies [13]. Furthermore, THz waves are used now for monitoring the thickness and moisture content of papers by manufacturers [14] [15].

1.3.2   THz Imaging

- **Biomedical imaging**

  Because THz frequencies have the ability to penetrate up to a few hundred micrometers in human tissues; it is a possible to use these frequencies for superficial detection in some parts of human body such as skin [16], teeth decay [17], breast and mouth cancer [18], and analysis of DNA signatures and protein structures [19].

- **Metal contact imaging**

  The THz pulsed imaging is a very convenient method to take 3D images from the inside of an integrated circuit device as compared to 2D images provided by the X-ray method [20].

- **Diagnostics imaging**

  The terahertz diagnostics include: cereals and chocolate [21], polymers and composites [22], pharmaceutical tablets [23], engine oils [12].

1.4   Historical View

The interest in terahertz science and technology started in the 1960s. This subject was motivated by astrophysicists when they began to study the rotational spectra of some gases that fall into the THz range [24] [25]. In 1974 some researchers [26] used pico-second photoconductivity in silicon to generate and detect some frequencies in the THz range. Subsequently, the interest in this frequency range increased rapidly [27] [28] [29] [30]. Before 1990s, the portion of THz range was the least investigated spectrum of electromagnetic radiation because of the absence of efficient, coherent, and compact THz emitters and detectors [31] [32]. At that time the developments of characterization techniques in semiconductors materials were essential to study the ultrafast carrier dynamics and relaxation processes and to improve the next generations of optoelectronic devices for THz technology [33]. Early research was focused on generating sub-picosecond electrical pulses in semiconductors by Auston [34] [35]. In 1988 it was reported the first dipole antennas that depended on radiation-damaged Silicon-On-Sapphire (RD-SOS) pumped by colliding pulse

mode-locking dye lasers. This type of antenna generated broadband radiation from 100 GHz to 1 THz [36]. The real breakthrough for the use of THz pulses in spectroscopy was the introduction of substrate lenses, making it possible to direct the broadband radiation into a specific direction and then use optics to collimate the "terahertz beams" [37]. The transition from dye lasers to solid state femtosecond lasers like the Titanium-Sapphire laser, further simplified the use of THz technology. In the 1990's new materials became available through molecular beam epitaxy (MBE). Low-temperature grown Gallium Arsenide (LT-GaAs) with its short carries lifetime has excellent properties to be used in a photoswitch [38] and has replaced RD-SOS as material of choice in photoconductive THz-Setups.

1.4.1   The Role of Nanoparticles in Optoelectronic Devices

The study of electromagnetic properties of metal particles have been started in the early time of the twentieth century by the work of Wood [39]and Ritchie [40]. In recent years, this topic has gained renewed interest because of the development of new fabrication techniques of nanostructures with the available tools to characterize these structures using scanning electron microscope, transmission electron microscope (TEM), atomic force microscope (AFM). New fascinating properties emerged from studying the features of the nanoparticles. One important characteristic of metal nanoparticles is the localized surface plasmon resonance (LSPR). LSPR is a collective oscillation of free electrons inside the metal nanoparticles. The plasmonic properties of gold and silver nanoparticles have been studied widely and wildly because of that their LSPR is located in the visible region which has interest in the field of optoelectronic devices and solar cell applications [41]. Another reason is that Au and Ag nanoparticles have biological applications as antibacterial factor and medical applications in cancer treatment. TiN nanoparticles have also plasmonic resonance in the visible region but they have not been as extensively studied as Au and Ag nanoparticles. TiN NPs have been studied for the last two decades due to their both wide range and high absorption in visible and infrared regions and because of being non-toxic material. Because of these unique properties, many researchers have proposed using TiN NPs for medical applications. More details about the nanoparticles will be given in chapter 2.

1.5   Aim and significance of labor

This work is trying to achieve three important aims. The first aim is to build a flexible terahertz time-domain spectroscopic (THZ TDS) system with high stability and repeatability as a technique to study the properties of THz-photoconductive emitters. The system is designed to compare the performance of different THz antennas. The second aim is to find a correlation between growth quality and THz strength emitted from LT-GaAs antenna. Finally, the third aim is to enhance the performance of those antennas using titanium nitride and manganese ferrite nanoparticles.

Chapter 2

Terahertz Time Domain Spectroscopy

2.1   Background

This chapter gives the background knowledge to the topics introduced in the later chapters. To achieve this goal, the chapter briefly reviews the main topics in the thesis such as time domain spectroscopy (TDS), THz antennas, the growth of LT-GaAs and the use of NPs to enhance the performance of THz antennas. The chapter is arranged as follows: firstly, the technique of TDS is introduced; secondly, the Drude-Lorentz model and the theory for THz generation are explained, thirdly, the low-temperature growth of GaAs is discussed, and finally nanoparticles and plasmonic effects are briefly discussed.

2.2   Terahertz technology and Time-domain spectroscopy

The main idea of TDS is to generate and detect terahertz electromagnetic (EM) waves in the time-domain. The time-domain traces are then Fourier transformed to obtain the THz spectrum. The high (S/N) ratio is an important property of TDS systems [42]. Typical THz experiments such as used for imaging [43], tomography [44], or spectroscopy [11] consist of three essential parts: laser source, THz emitter and detector. Systems of this type have been used to investigate the portion of the EM spectrum located between the IR and the microwave regions [45] [46] [47]. Before

1980, there was no reliable source for THz in that region. Therefore, the spectroscopic properties of many materials were unknown at that time. However, the advent of mode-locked lasers with supicosecond pulse durations in the early 1980s opened a new door for THz spectroscopy [48] [49] [50]. The technique that combines ultrashort pulse laser technology with optically triggered antennas is called today THz TDS. Unlike the traditional spectroscopy, this technique detects the time-dependent amplitude of the electric field in EM wave instead of the frequency-dependent amplitude. THz TDS has the ability to investigate the dielectric properties of materials directly without using the Kronig Kramers relation [51] . After that, nonlinear materials (e.g, GaAs wafer) for optical rectification, were also used as emitters or detectors for terahertz radiation [52]. The photoconductive antennas (PCAs) are normally used as emitters and detectors in traditional TDS system. PCAs are based on semiconductors that convert optical light into THz radiation.In order to obtain perfect light absorption, the laser energy ($h\nu$) must be slightly higher than the band gap of the PCA material. The essential parts of a typical THz TDS setup are presented in Figure 2.1.
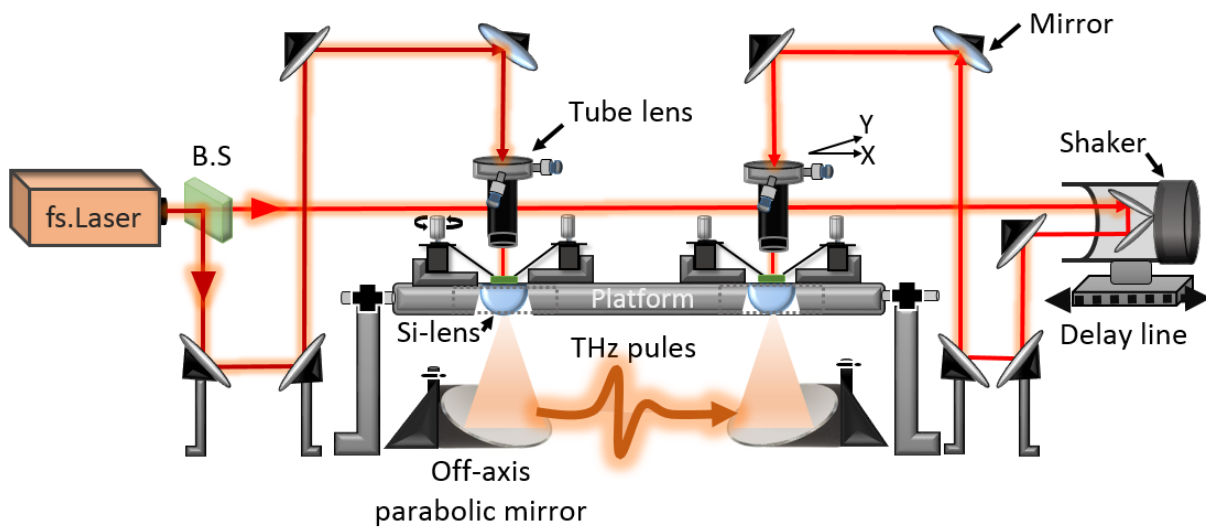
Figure 2.1: Schematic diagram of a typical THz TDS setup. The main parts are: femtosecond laser source, two photoconductive antennas, two silicon lenses attached to the photoconductive antennas, delay-line, shaker, off-axis parabolic mirrors, beam splitter, platform and reflecting mirrors.

Figure 2.1 depicts our novel THz TDS design in which a laser pulse is vertically incident on a coplanar stripline (CPS) antenna [53]. The horizontal part consists of a platform with two Si-lenses and antenna holder stages in "X-Y" directions. The laser paths were aligned such that the foucused laser beams hit the centers of the Si lenses. A beam splitter (B.S.) splits the femtosecond laser pulse in to two pulses: the first pulse excites the emitter and second pulse is utilized to excite

the detector. Therefore, we have two paths namely the emitter and the detector paths. The detector path contains a delay-line with a shaker in order to obtain variable arrival of the optical pulses. The job of the delay-line is to delay the arrival of the optical pulse by a time (τ). In this way, when the THz pulse is emitted at time (t), the detector becomes photoconductive at time (t+τ). The AC current generated at the detector should be measured versus (τ) set-by-step with a step-value (τ) so as to reconstruct the electromagnetic field of the THz pulse. The detector signal, which is connected to the field amplitude of the THz pulse, is traced by a lock-in amplifier and recorded against(τ). The THz spectrum can be obtained using FTT for the detector signal.

2.2.1   Laser Source

More than one type of laser source can be used to excite the antennas in TDS systems. Our pump source is a Ti-Sapphire laser, with a center wavelength of 780 nm, a pulse energy of 10 nJ, and a pulse duration of 150 fs. The repetition rate is 80 MHz. In our TDS setup, the excitation laser power at the biased emitter is 25 mW while it is 18 mW at the detector. The bias voltage is 1-30 Volt.

2.2.2   Structure of photoconductive antenna

Traditional antennas used in TDS THz systems usually contain two metal electrodes deposited on the surface of a semiconductor material using thermal evaporation or sputtering techniques. The job of that contact metallization is to facilitate probe connections for applying voltage to the illuminated antenna gap between the two electrodes as shown in Figure 2.2.
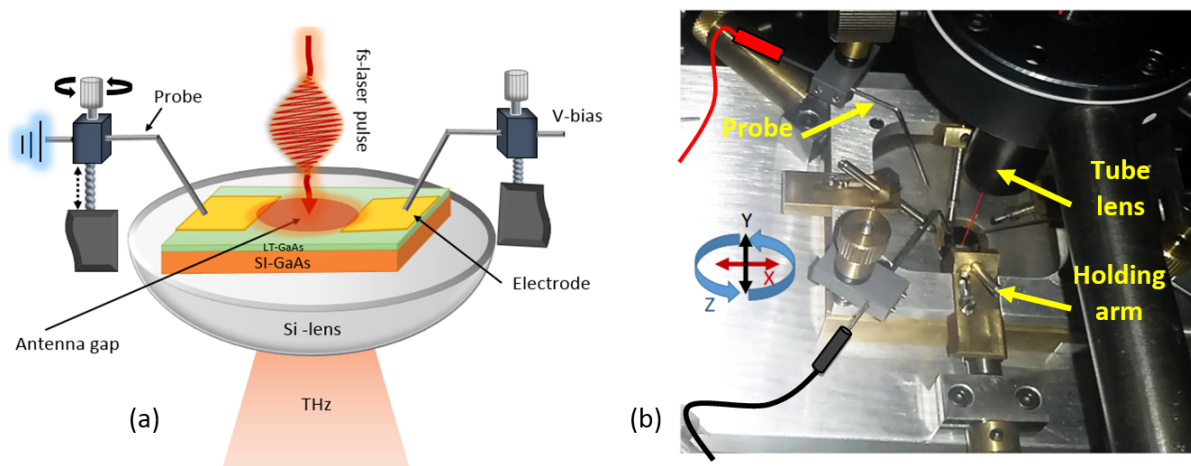
Figure 2.2: Schematic diagram of the LT-GaAs antenna with two gold electrodes and (b) photo of the device holding the THz antenna.

Figure 2.2(a) shows a laser pulse incident on a PCA made from LT-GaAs deposited on semi-insulating GaAs. The laser light induces a fast-rising carrier density in the illuminated area. The free charge carriers are accelerated by the electric field of the applied voltage. As shown later, the current density can be approximated by the Drude-Lorentz model [54]. As shown in Figure 2.2(b) we installed the platform such that the laser beam and THz radiation propagated vertically. This gives our system additional flexibility to change and align the THz antennas (emitter, detector).

The antennas used in this experiment for the emission and detection of THz radiation, have various types' structure and sizes as a (CPS), dipolar, Butterfly and Bow tie. Figure 2.3, shows a photo of these THz antennas.
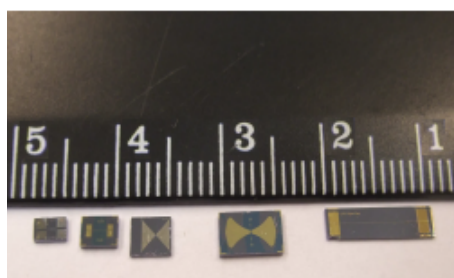
Figure 2.3: Typical antennas used in our TDS system.

2.2.3 THz antenna

Typically emitter and receiver differ in their design. Figure 2.4 shows the two common designs of THz antenna. The different designs of gaps or apertures provide a normal way for THz generation. There are many approaches to design a suitable antenna gap to minimize the impact of both space charge and screening effect on the terahertz antenna performance, which are classified into two categories: large and small antenna gaps. While the influence of large antenna gaps did not lead to a solution such as that of small antenna gaps, therefore the most appropriate solution in the electron-hole separation is to use the small antenna gaps.
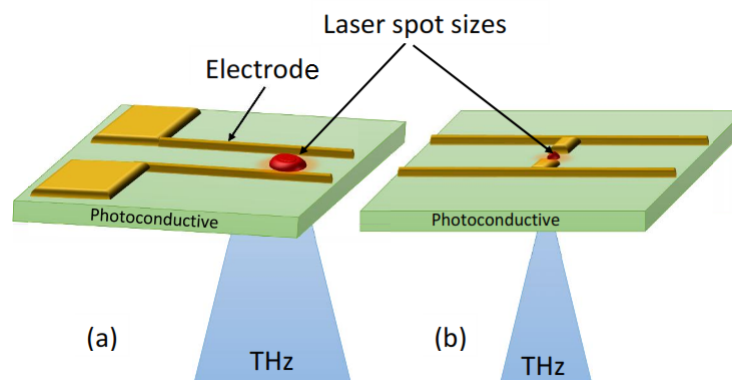
Figure 2.4: Sketch of THz photoconductive antennas (a) large-aperture coplanar strip line (CPS) (b) small gap dipole antenna.

Figure 2.5 shows the measured THz amplitude as a function of time fore a CPS emitter and a dipole receiver antenna, and shows the Fourier transform (FFT) of that pulse to the frequency domain. Both antennas are made from LT-GaAs. The fluctuations to the right side of the pulse in both figures are caused by the absorption and the re-emission of THz radiation by H_2O vapor molecules in the atmosphere of the lab. The width and space of the THz spectrum are determined by a variety of effects which are discussed in the following.

11
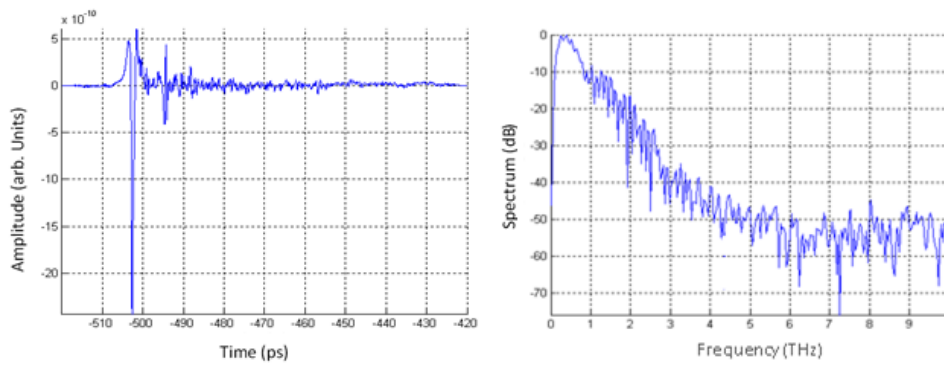
Figure 2.5: THz signal and the FFT data as shown by Teralyzer.

2.3 Drude-Lorentz Model for Photoconductive Antennas

The Drude-Lorentz model is a simple one-dimensional model that can describe the main properties of charge motion in a biased semiconductor [54]. Due to the low effective mass of electrons compared with holes, it is reasonable to assume that electrons in the conduction band are mainly responsible for the current in a GaAs based photoconductor. For a given number of electrons per-unit volume, i.e., n_e electron density, $J_e(t)$ the electron current density as a function of time is given by [54]:

$$J_e(t) = -en_e(t)\upsilon(t) \tag{2.3.1}$$

Here $\upsilon(t)$ is the velocity of the electrons, which is also a function of time. The incident photons on the photoconductor generate a certain number of electrons per-unit time. This is described by the generation rate $G(t)$. Some of the electrons are trapped for instance inside the trapping states in the mid-bandgap, therefore changes in the electron density are described as follows [55]:

$$\frac{dn_e}{dt} = -\frac{n_e}{\tau_{trap.}} + G(t) \tag{2.3.2}$$

Here the generation rate is given by $G(t) = n_\circ exp(-t^2/\triangle t^2)$. $\triangle t$ is the pulse duration of the laser pulse which is in the order of 30-150 fs.

12

Using Newton's second law, the electric force is given by:

$$F = m^* \frac{dv}{dt} = qE_{loc.} - F_R \tag{2.3.3}$$

Where m^* is the effective mass of charge carrier, $q = -e$ for electrons and $q = +e$ for holes ($e = -1.6 \times 10^{-19} As$), $E_{loc.}$ is the local electric field, $F_R = -v/\tau_{relx.}$ is the resistive force which is monotonically scaling with the velocity and inversely proportional to relaxation time $\tau_{relx.}$ (also called scattering time: the time between two successive collisions which is about 30 fs in LT-GaAs). The velocity rate for the excited electron-hole pairs is given by [55]:

$$\frac{dv_{e,h}}{dt} = -\frac{v_{e,h}}{\tau_{relx.}} + \frac{q_{e,h}E_{loc.}}{m^*_{e,h}} \tag{2.3.4}$$

Here $v_{e,h}, q_{e,h}$ are the average velocity and charge of the electrons and holes respectively. The relationship between the localized and bias fields can be written as:

$$E_{loc.} = E_{bias} - \frac{P}{b\varepsilon_r} \tag{2.3.5}$$

Where P is the polarization due to the separation of the electrons and the holes, E_{bias} is the biased electric field, ε_r is the dielectric constant (permittivity), b is a geometrical factor. According to [56] it is $b \approx 3$ for LT-GaAs. The temporal variation of polarization is given by:

$$\frac{dP}{dt} = -\frac{P}{\tau_{rec.}} + J(t) \tag{2.3.6}$$

Where $\tau_{rec.}$ is the recombination time, $J(t)$ is the current density between the two electrodes which is a function of time and it can be defined by:

$$J(t) = env_h + (-e)nv_e \tag{2.3.7}$$

Using Maxwell Equations, the field of THz radiation in the far field region can be given

by [57]:

$$\frac{dE}{dt} = -\left[\frac{A}{4\pi\varepsilon_\circ c^2 z}\right] \cdot \frac{dJ(t)}{dt} \tag{2.3.8}$$

Where A is the area of the gap between the two electrodes. By employing Eq.(2.3.6), we can obtain an expression for the THz field:

$$E_{THz} \propto \frac{\partial J(t)}{\partial t} \propto \left[ev\frac{\partial n}{\partial t} + en\frac{\partial v}{\partial t}\right] \tag{2.3.9}$$

That is to say that the intensity of THz radiation depends essentially on the variation of the current density with time, which is associated with the generation, recombination and acceleration of carriers inside the photoconductive material between the two electrodes. In the above model the geometry of the antenna is ignored.

2.4   Screening Effect

Inside photoconductive THz antennas one typically has screening effects. The applied bias field is screened on a time scale comparable to the pulse duration of the THz radiation [58]. This effect can influence both bandwidth and shape of the emitted pulses. Because we are dealing with Ultrashort pulses in the range of femtoseconds, in many of these models, several effects that accompany longer times scales such as electron hole trapping, Nan-radiative recombination, and diffusion of carriers are ignored.

2.5   Low temperature growth LTGaAs and epitaxial properties

Since 1990s there were many investigations focusing on growing of GaAs layers by molecular beam epitaxy (MBE) at relatively low temperatures (200 – 300 °C). The GaAs prepared in that low range of temperatures is called LT-GaAs. The conventional substrate temperature used to

grow high quality GaAs is in the range of 500 – 600 °C [59]. A good review of the early works in this aspect can be found in the reference [60]. First reports in that direction showed that LT-GaAs layers have unique properties. For example, annealed layers of LT-GaAs revealed a low electrical conductivity of less than $9.4 \ mS/cm$ and short minority carrier lifetimes of less than 1 ps. Consequently, LT-GaAs found applications in the field of fast-response photodetectors, THz devices, generators and other electronic devices as insulating buffer in several types of chips and FET [61]. Growth procedures for LT-GaAs are described in the references [61] [62]. Several investigations were devoted to study structural, electrical and optical properties of as-deposited and annealed LT-GaAs layers [63] [64].

2.6 Studying the morphology of LT-GaAs

2.6.1 Calculation of surface roughness

There are two types of surface roughness: average roughness as known as arithmetic average R_a is the arithmetic mean of all deviations from the centerline over the sampling path. The other type geometric roughness S_q is the root mean square (RMS) roughness. Consider the example in the Figure 2.6 with rough surface.
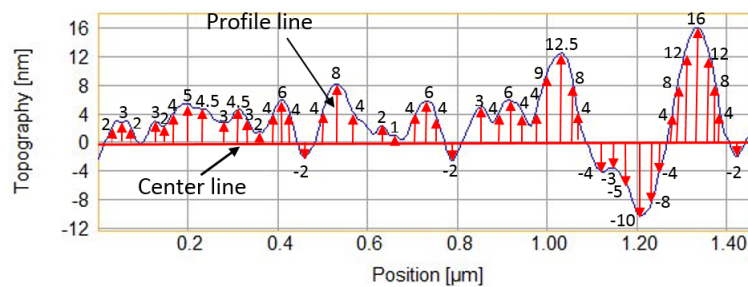
$$S_q = \frac{\sqrt{2^2 + 3^2 + 2^2 + 3^2 + 2^2 + 4^2 + 5^2 + \cdots \ldots \ldots + 2^2}}{48} = 6.0255 \ nm$$

Figure 2.6: Method of calculation of the roughness of the LT-GaAs surface.

2.6.2 Calculation of grain size

In Figure 2.7, the distribution of grain size is analyzed either manually (a) or by commercial software (Image-J) in (b). In order to manually calculate the particle size, we consider only the average length of the two perpendicular axes. For example, at (a) we have calculated the two axes for each shape to be $55.48 \times 29.03\ nm^2$. The (c) and (d) shapes have the same perpendicular lengths and (e) is one of the shapes of the nanoparticles which appeared at mid-surface of the THz antenna [65].
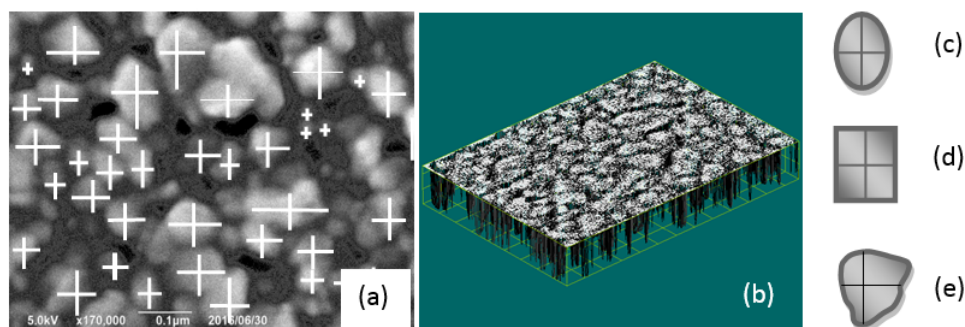
Figure 2.7: (a) Calculation of particle size from SEM image with (b) Image J software calculation of particle size from SEM image of a rough LT-GaAs surface such a (c, d, e) Three different shapes for grains size.

2.6.3 Synthesis of NPs

There are two main approaches to fabricate NPs: Top to down and Bottom to up.

- Top to down: methods involve breaking the bulk material into nanoparticles.

- Bottom to up: building by assembling it from building blocks (such as atom-by-atom, molecule by molecule, or cluster-by- cluster).
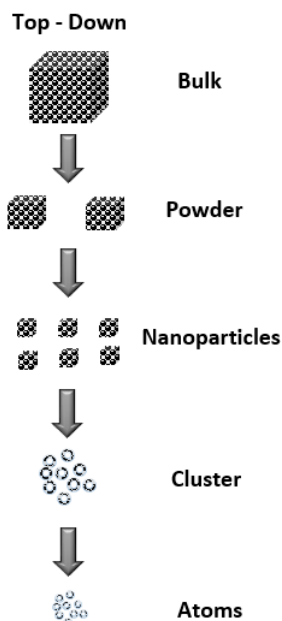
Figure 2.8: Illustration of the common Top – Down method to nanoparticles fabrication.

2.7   Preparation of TiN NPs by Laser Ablation

Pulsed laser ablation in liquids (PLAL) is a technique which has been increasingly used as "top-down" method for the preparation of nanoparticles in liquid medium. The nanoparticles are prepared directly from its targets in the form of pellets or compressed powders. The target, which is immersed in a liquid such as water or ethanol, is exposed to intense laser pulses. This approach was essentially used to produce gold, silver and other noble NPs which cannot be prepared by wet chemical methods [66]. Among other techniques to fabricate NPs [67], PLAL is preferred because it is a low cost method to prepare pure NPs without using any vacuum equipments. Besides NPs are easily collected after the synthesis. The NPs fabricated by PLAL are usually kept in their solutions as a colloidal [68] and they can be safely handled in that form [69]. The most important advantages of PLAL is that it can be used to produce NPs from different materials such as metals, semiconductors and insulators and the properties of the NPs prepared by PLAL can be very well controlled using variable preparations [70]. Other advantages of PLAL over other mechanical and thermal techniques come from the low spot size of laser beam which leads to micro-localization of the laser-material interaction, and this provide the target with a very high heating-cooling rate as large as 1,000 K/ns in a very small volume [71]. One of the advantages of this PLAL method

17

is that the NPs can be prepared using a surface of native target, which involves several other benefits. The disadvantages of PLAL are in many of the cases, the NPs prepared by PLAL are suffering from agglomeration (excessive coalescence of NPs). This problem can be solved using suitable surfactant [72] which may increase the stability of the NPs against agglomeration. However, the presence of surfactant molecules makes the NPs no longer nascent and we consequently lose one's of the most important advantages for which the PLAL is used. Secondly, the yield of NPs prepared by PLAL is usually very low and the particles have a wide size distribution [73]. Therefore, it is important to determine the physical parameter that may lead to a reduction of the size distribution. It has been shown that laser wavelength, pulse duration, ablation time, and laser fluence are among the most important physical parameters to enhance the mono-dispersivity of the NPs [74] [75] [76] [77].

2.8 Morphologies of nanoparticles

NPs can be formed with different shapes and hence they have different names. For example, NPs with spherical shapes are called nano-spheres, in the same way we have nanocubes nanotubes, nanoreefs, nanoflowers, nanoclusters, etc. These shapes are the main elements of NPs morphology. In order to obtain the desired properties of NP, controlling the morphology of NPs plays an important role in that aspect. For example, gold NPs with an anisotropy of the particle shape and size have different plasmon features. Zeta potential and dynamic light scattering measurements are two important experiments which can be used to characterize the NPs in their liquid medium (colloidal phase).

2.8.1 Zeta potential

The Zeta potential term ($\zeta - potential$) or electrokinetic potential is the electric potential difference between the slipping plane and ionic layer around a charged colloid ion, see Figure 2.9. The value of the $\zeta - potential$ determines the electrical charge of particles that are submerged in the liquid and demonstrates the Double-layer properties of a colloidal dispersion [78]. At $\zeta - potential$ values less than ± 10 mV, the particles start to agglomerate. At higher values, the colloid becomes

more stable. More details are outlined in Table 2.1 .
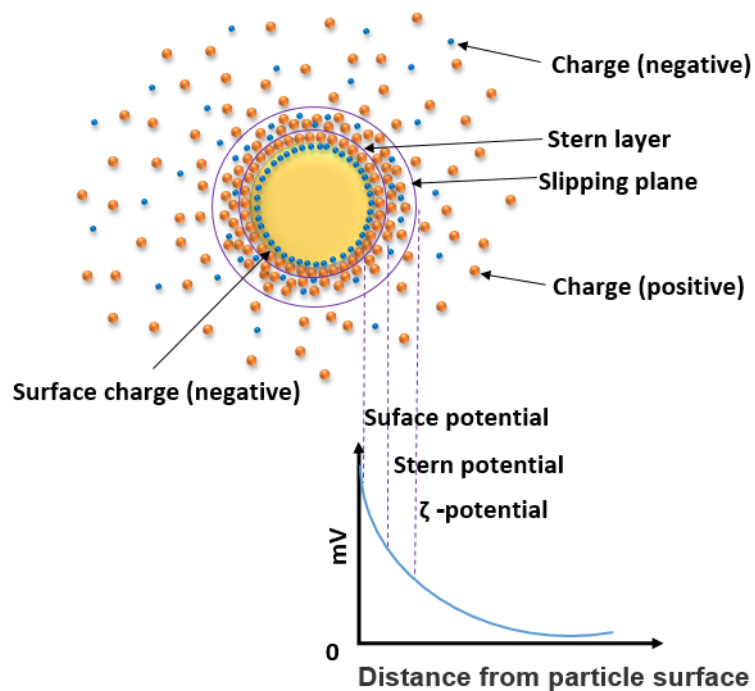
Figure 2.9: Charge concentration and potential difference as a function of distance from the charged surface of a particle attached in a dispersion medium.

Table 2.1: The stability behavior of colloids with low and high $\zeta - potential \pm$ between Zero and 61mV [79].

Zeta potential [mV]	Stability
from 0 to ±5	Agglomeration
from ±10 to ±30	Instability
from ±30 to ±40	Stability
from ±40 to ±60	Good stability
more than ±61	Excellent stability

2.8.2   Dynamic light scattering

Dynamic light scattering (DLS) is a technique used to measure the particle size in the range from less than 5 nm up to several microns. In DLS technique, the data of scattered light from moving particles in gas or liquid are collected. The amount of scattered light is assumed to be essentially dependent on the several parameters such as molecular weight of particle, size, shape and refractive index of both the particle material and the solvent. [80] [81]

2.9   Plasmonic Nanoparticles

Nanoparticles are particles that have dimensions from 1 to 100 nm [82]. Plasmonic nanoparticles refer to nanoparticles produced from noble metals such as gold (Au) and silver (Ag) that exhibit unique optical properties due to their localized surface plasmon resonance (LSPR) [83]. These unique electromagnetic properties of metal nanoparticles have been known since 1902 [84] but renewed interests and applications were emerged in the last decades [85]. Plasmonic nanoparticles such as Au and Ag nanoparticles consist of free electrons moving in a sea of positive ions (lattice). When a metal NP is exposed to light with its resonance frequency, the oscillating EM-field of the light induces a collective oscillation of the free electrons in the conduction band of the metal. In other words, all free electrons are displaced from their original positions. Because these two entities (electrons and lattice ions) have different types of charges, the positive ions apply a restoring force on the electrons and this may result in the electrons to overshoot which may lead to a restoring force in the opposite direction [86]. This effect gives rise to the so called surface plasmon resonance (SPR). A schematic illustrating this effect is depicted in Figure 2.10 for spherical nanoparticles [87].

The SPR induces a strong absorption of the incident light and hence can be measured using any traditional UV-VIS absorption spectrometer. The SPR effect is much stronger for noble metal NPs than for others, while SPR frequency and intensity have an effect on the electron charge density of the NPs surface. The most important factors are NP-metal type, shape, size, composition, and the relative permittivity of the surrounding medium. The problem of light interaction
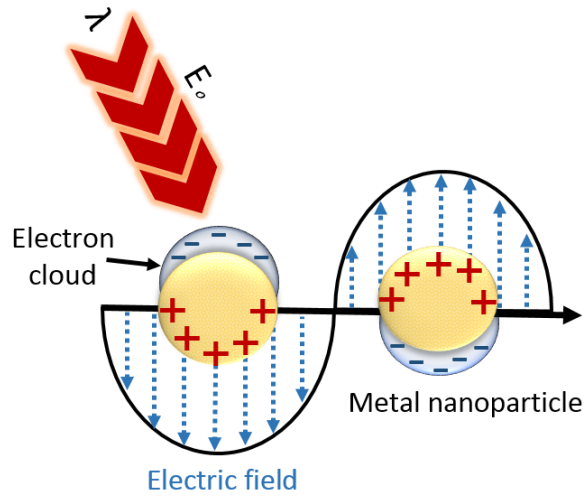
Figure 2.10: The light field with resonance frequency (represented by arrows) is incident on spherical nanoparticles. Displacement of electrons causes plasma oscillations.

with nanoparticles was first theoretically solved by Gustav Mie in 1908 as an effort to explain different colors exhibited from tiny colloidal gold particles suspended in water [88]. In Mie theory, the electromagnetic fields of scattered light have been written as an infinite series of spherical harmonics usually called normal modes of spherical nanoparticle [88]. According to Mie theory, the attenuation of light by nanoparticles is given by the extinction and scattering cross sections defined respectively [89] by the following equations:

$$\sigma_{ext} = \frac{2\pi}{|\overrightarrow{k}|^2} \sum_{\infty}^{n=1} (2n+1)R_e[a_n + b_n] \qquad (2.9.1)$$

$$\sigma_{sca} = \frac{2\pi}{|\overrightarrow{k}|^2} \sum_{\infty}^{n=1} (2n+1)R_e[|a_n|^2 + |b_n|^2] \qquad (2.9.2)$$

Where $\overrightarrow{k}$ is the wave vector of electromagnetic wave, n is the order of the multipole, a_n and b_n are the Mie parameters. When the radius of the particle is much smaller than the light wavelength ($a << \lambda$) the expression for σ_{ext} can be simplified using a quasi-static approximation to give [88]:

$$\sigma_{ext} = 9\frac{\omega}{c}\varepsilon_m^{3/2}V\frac{\varepsilon_2(\omega)}{[\varepsilon_1(\omega) + 2\varepsilon_m]^2 + \varepsilon_2(\omega)^2} \qquad (2.9.3)$$

Where ω is the angular frequency, c the light velocity, *V* the volume of the nanoparticle, ε_m the permittivity of the matrix medium in which the particles are imbedded, $\varepsilon_1(\omega)$ and $\varepsilon_2(\omega)$ are the real and the imaginary parts of the permittivity function defined by $\varepsilon(\omega) = \varepsilon_1(\omega) + i\varepsilon_1(\omega)$. The polarizability of materials, can be given by [90]:

$$\sigma_{ext} = 3\frac{2\pi}{\lambda}\sqrt{\varepsilon_m}Im(\alpha) \tag{2.9.4}$$

Where the polarizability equation is given by [91]:

$$\alpha = 4\pi a^3 \frac{\varepsilon_M - \varepsilon_m}{\varepsilon_M - 2\varepsilon_m} \tag{2.9.5}$$

Where ε_M is relative permittivity of bulk material of the metal particle.

The resonance of LSPR occurs at $\varepsilon_M = 2\varepsilon_m$ where the denominator in the last equation becomes zero.

As an example for using the polarizability equation [91], we consider Au NPs in water. The relative permittivity of gold is complex in the range 500 - 550 nm as given in Table 2.2. In order to estimate the wavelength of LSPR of AuNPs, we used also the data for Au NPs given in Table 2.2.

Table 2.2: The real and the imaginary parts of the complex relative permittivity of gold between 500 nm and 550 nm.

Wavelength (nm)	ε_1	ε_2
500	-2.3	3.6
510	-3.0	3.1
520	-3.7	2.7
530	-4.4	2.4
540	-5.2	2.2
550	-6.0	2.0

Because ε_m is real, the resonance condition $\varepsilon_M = 2\varepsilon_m$ is satisfied when $\varepsilon_1 = 2\varepsilon_m$. For our medium (water) [92], we have $\varepsilon_m = 1.77$, and therefore we require that $\varepsilon_1 = 3.5$. In Table 2.2, this value is between $\varepsilon_1 = -3.0$ and $\varepsilon_1 = -3.7$ and these two values are opposite to $\lambda = 510$ nm and 520 nm this means that this condition is satisfied when $\lambda \approx 517\,nm$ which is the location of LSPR of Au NPs [91].

2.10   Plasmonic light trapping by different mechanisms

The incorporation of plasmonic nanostructures (NS) in certain optoelectronic devices can enhance the performance of these devices due to the light trapping effect. The light trapping leads to strong light interaction in plasmonic NS and the surrounding medium. In the field of solar cells for example, Atwater [93] suggested three different basic configurations of employing plasmonic NS. Figure 2.11 illustrates the situation when NPs are incorporated on the surface of the semiconductor, where the NPs are used to support the light scattering. As has been done in this thesis, most of plasmonic NS-designs explore the incorporation of metal NPs on the top surface of the photoconductive materials. This method provides preferential scattering of incident light in forward direction, in such a way that it increases the angular range, and, hence, it increases the optical path length [93]. The LSPR-effect and, hence its strong light absorption works in certain regions in which strong local electromagnetic field is available. The absorbed power is proportional to the intensity of the local electromagnetic field.
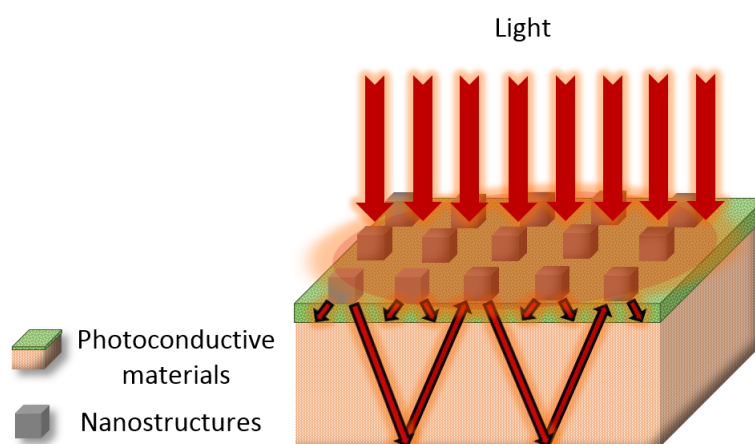
Figure 2.11: Plasmonic NS can be used to enhance light scattering and absorption in solar cells as proposed by Atwater.

Figure 2.12 shows the normalized scattering cross-section (SC) calculated on the basis of the Mie theory for different particle sizes. Four different sizes of spherical shapes are investigated (20, 50, 100, and 200 nm). When the medium is air Figure 2.12(a), the NPs with particle size 100 nm have maximum SC in the wavelength range (350 - 450 nm). The NPs with particle size 200 nm have higher SC with wider scattering band for the wavelengths greater than 450 nm. Figure 2.12(b) shows the effect of medium (Silicon) with a higher refractive index than air: the plasmonic resonances show a red shift. This red-shift is desirable for solar cell devices since high scattering is preferred for longer wavelengths in the visible region which is compatible with the higher intensity of the sun in that spectral region where fundamental absorption of Si ($E_g = 1.1eV$) is located. However, as the particle size increases the light SC will decrease and also multipole resonance oscillations are initiated as shown in Figure 2.12(b). Larger particles have larger surface coverage and this leads to undesirable increased parasitic absorption and reflection. These effects reduce the preferred optical absorption in the active layer of the solar cell device.
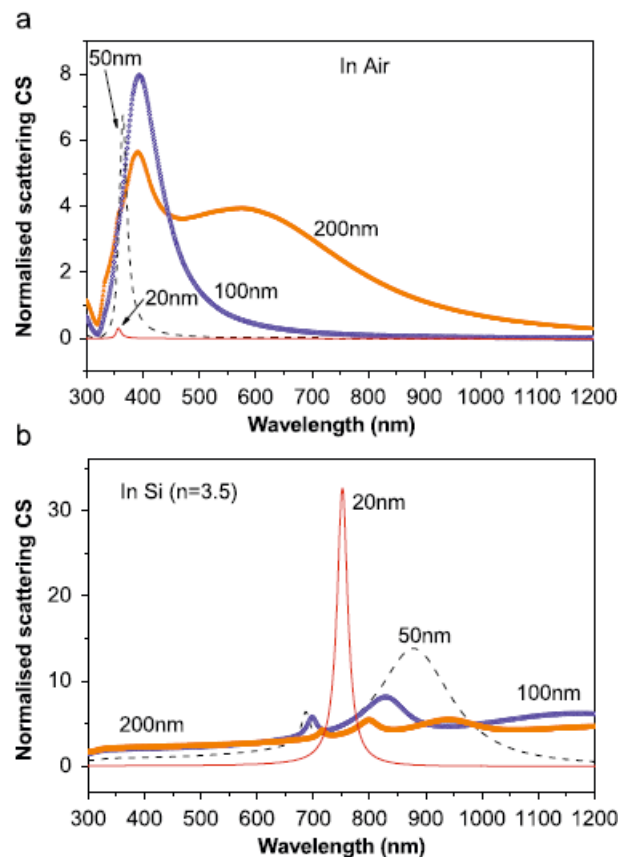
Figure 2.12: The normalized scattering cross-section of different diameter spherical particles vs. wavelength in two different media: (a) Air and (b) Silicon, [41].

Chapter 3

Publications

3.1   List of publications

1. Oday Mazin Abdulmunim, Norman Born, Martin Mikulics, Jan C. Balzer, Martin Koch and Sascha Preu, "High accuracy terahertz time-domain system for reliable characterization of photoconducting antennas", Microwave and optical tehchnology letters, **59**, 468-472 (2017).

2. Abdulmunem, O. M., K. I. Hassoon, J. Völkner, M. Mikulics, K. I. Gries, and Jan C. Balzer. "Photoconductive LT-GaAs Terahertz Antennas: Correlation Between Surface Quality and Emission Strength." Journal of Infrared, Millimeter, and Terahertz Waves, **38**(5):5574-582 (2017).

3. Abdulmunem, Oday, Khaleel Hassoon, Mahmoud Gaafar, Arash Rahimi-Iman, and Jan C. Balzer. "TiN Nanoparticles for Enhanced THz Generation in TDS Systems." Journal of Infrared, Millimeter, and Terahertz Waves, DOI: 10.1007/s10762-017-0412-z, 1-9 (2017).

4. Lai, Weien, Oday Mazin Abdulmunem, Pablo Del Pino, Beatriz Pelaz, Wolfgang J. Parak, Qian Zhang, and Huaiwu Zhang. "Enhanced Terahertz Radiation Generation of Photoconductive Antennas Based on Manganese Ferrite Nanoparticles." Scientific Reports **7**:46261, DOI: 10.1038/srep46261 (2017).

3.2 List of other contributions papers

1. Abdul-Munaim, Ali Mazin and Reuter, Marco and Abdulmunem, Oday Mazin and Balzer, Jan C and Koch, Martin and Watson, Dennis G. "Using Terahertz Time-Domain Spectroscopy to Discriminate among Water Contamination Levels in Diesel Engine Oil." Transactions of the ASABE **59**.3 (2016).

2. Lippert, Sina and Schneider, Lorenz Maximilian and Renaud, Dylan and Kang, Kyung Nam and Ajayi, Obafunso and Kuhnert, Jan and Halbich, Marc-Uwe and Abdulmunem, Oday M and Lin, Xing and Hassoon, Khaleel and others"Influence of the substrate material on the optical properties of tungsten diselenide monolayers." 2D Materials **4**.2, 025045 (2017).

3.3 High Accuracy Terahertz Time domain System for Reliable Characterization of Photoconducting Antennas

O. M. Abdulmunem, Norman Born, Martin Mikulics, Jan Christof Balzer, Martin Koch and Sascha Preu, Microwave and optical tehchnology letters, 59(2):468-472 (2017).

3.3.1 Abstract:

In this work we report on a terahertz time-domain system (THz TDS) to characterize photoconductive THz emitters and detectors, that is designed for highest reproducibility. This system is excellently suited for studying the performance of THz emitter and detector antennas in a systematic manner, either by varying the substrate materials or the geometrical parameters of metallic antenna contacts building a photoconductive switch. After confirming the reproducibility and stability of the system with errors of only 1.9% (over 3 h) and 2.6% (over 9 days), we use the system to compare the performance of five low temperature grown Gallium Arsenide (LT-GaAs) antennas with growth temperatures between 200-300°C.

3.3.2 The author's contribution:

The design of experiments and all the practical steps of this study were carried out by me. Norman Born helped me in the laboratory, with other coauthors of the group in Marburg also having strongly supported the experimental achievements. The antennas was designed and provided by Martin Mikulics. The manuscript was written by Jan Christof Balzer and Sascha Preu and me. All co-authors contributed with discussions and corrections to the manuscript.

1. INTRODUCTION

THz technology has come a long way from its beginnings [1] to recent developments [2]. Applications range from communications [3], over material characterization [4], to the inspection of industrial goods [5]. In particular, the two latter fields circle around THz time-domain spectroscopy (TDS) [6] which is a key technique and is used in many research labs worldwide. It relies on photoconductive antennas which are gated by ultrashort laser pulses (see Refs. [5–8] for details). Alternatively, pulses can be generated and detected in non-linear crystals by optical rectification and electro-optic sampling [9,10], respectively. Yet, photoconductive antennas are more widely used and allow for fiber-coupling [11,12]. While lasers are abundant today, engineering the photoconductive material is still of key importance and an ongoing research field with a long tradition. Early materials were ion-implanted silicon-on-sapphire [13,14], and semi-insulating GaAs[15] before LT GaAs was discovered [16], which is still to date one of the most efficient photoconductive materials. It features up to GΩ/square dark resistance, carrier lifetimes as low as ∼150 fs with still a moderate mobility of a few 100 cm^2/Vs [17]. While a short carrier lifetime is not very relevant for pulsed THz generation, it is particularly important for detection [18] and for continuous-wave (CW) operation [19]. A yet remaining difficulty is achieving higher carrier mobilities for improving the photocurrent yield without affecting the short lifetime. Modern materials research tries to solve this requirement and expand the operation to other laser wavelengths such as 1550 nm (telecom band) by development of new, more exotic materials and structures. These include ion-implanted photoconductors [20], inclusion of rare earth semimetals in GaAs or InGaAs [21–23], and formation of quantum wells and superlattice structures [24,25]. Other groups focus on the development of new photoconductive materials such as BiGaAs [26], GaAsSb [27], or InGaAsP [28]. Furthermore, the impact of the metallization has been explored [29].

In order to evaluate the performance of various photoconductive materials, their output power and output spectra must be compared. This is particularly the case for LTG-GaAs, where the material quality is strongly growth temperature- and annealing temperature-dependent with a fairly narrow temperature window where the lifetime is still in the sub-picosecond range [30] but the mobility reaches values above a few 100 cm^2/Vs. These growth and annealing temperatures have to be calibrated for each growth system, individually. Usually, in comparison experiments, the devices are not packaged, neither pigtailed, which is too costly and time-consuming. Unfortunately, pulsed THz systems are extremely alignment-sensitive. A small misalignment, e.g., of the device relative to the silicon lens, can easily reduce the transmitted THz power by half an order of magnitude or alter the transmission function from sender to receiver, resulting in a suppression of specific frequency components, altering the transmitted spectra.

While most articles present mostly a singular measurement of record data with no study of reproducibility and repeatability, only very few groups focus on systematic evaluation of the THz performance of a larger number of samples. This is a required

HIGH ACCURACY TERAHERTZ TIME-DOMAIN SYSTEM FOR RELIABLE CHARACTERIZATION OF PHOTOCONDUCTING ANTENNAS

Oday Mazin Abdulmunem,[1] **Norman Born,**[1] **Martin Mikulics,**[2] **Jan Christof Balzer,**[1] **Martin Koch,**[1] **and Sascha Preu**[3]
[1] Faculty of Physics and Material Sciences Center, Philipps-Universität Marburg, Marburg D-35032, Germany; Corresponding author: jan.balzer@physik.uni-marburg.de and preu@imp.tu-darmstadt.de
[2] Peter Grünberg Institut (PGI-9), Forschungszentrum Jülich, Jülich D-52425, Germany
[3] Terahertz Systems Technology, Department of Electrical Engineering and Information Technology, Technical University Darmstadt, Rundeturmstrasse. 12, Darmstadt D-64283, Germany

ABSTRACT: *We report on a terahertz (THz) time-domain system to characterize photoconductive THz emitters and detectors, that is designed for highest reproducibility. This system is excellently suited for studying the performance of THz sources and detectors in a systematic manner, either by varying the substrate materials or the geometrical parameters of metallic antenna contacts building a photoconductive switch. After confirming the reproducibility and stability of the system with errors of only 1.9% (over 3 h) and 2.6% (over 9 days), we use the system to compare the performance of five low temperature grown (LT) GaAs wafers with growth temperatures between 200°C and 300°C.*
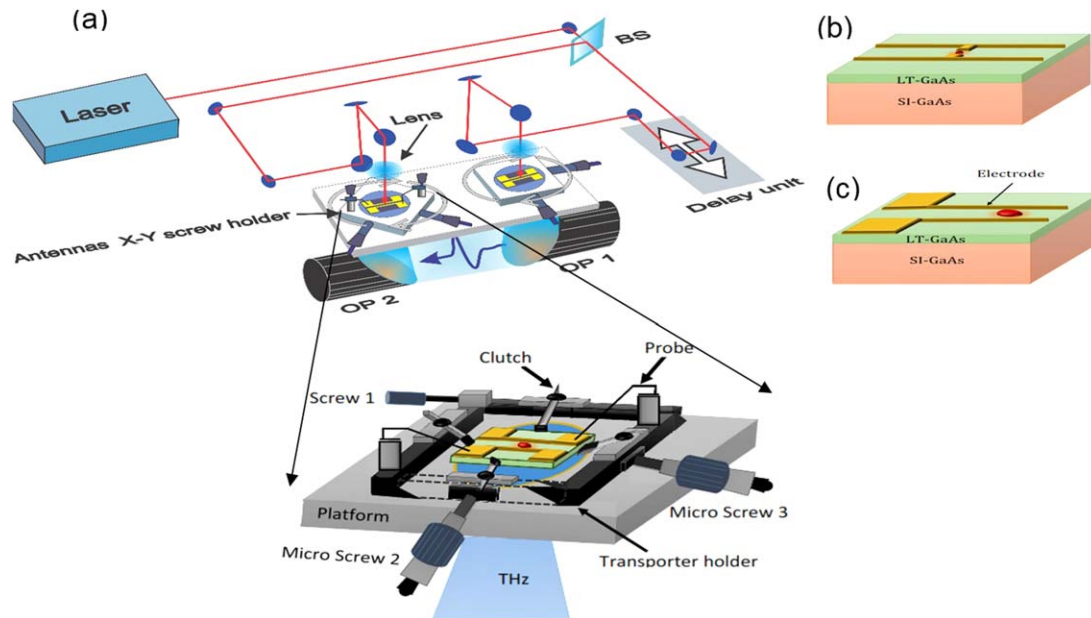
Figure 1 (a) Schematic drawing of photoconductor characterization setup. b) Layout of the photoconductive antennas as described in the text. c) Layout of the coplanar stripline antenna with a stipline spacing of 200 μm. [Color figure can be viewed at wileyonlinelibrary.com]

procedure for commercial applications where reproducibility and repeatability is a must.

In this article, we demonstrate a setup that is designed to allow for highest repeatability with a systematic error of the transmitted electric field in the few percent range. In order to demonstrate the full capabilities of the system, we evaluate systematically the performance of five LT GaAs wafers that were grown at temperatures between 200°C and 300°C in steps of 25°C.

2. HIGH ACCURACY TDS SYSTEM

The setup is illustrated in Figure 1 (a). It is based on a 780 nm mode-locked Ti:sapphire laser (Tsunami, Spectra-Physics) with a pulse duration of 150 fs and a repetition rate of 80 MHz. The laser pulse is split in two arms with 25 mW laser power for the emitter arm and 17 mW for the receiving photoconductor arm. A delay line is included in one arm. Each beam is guided onto a focusing lens. Both source and detector photoconductor are placed on top of a silicon lens in an aplanatic configuration (diameter: 10 mm, hyperhemispherical offset including chip thickness of 500 μm: 1.4 mm) that is mounted on a high precision 3D alignment stage in order to position the devices in the focal point of the optical lenses. The laser is used for prealignment of the THz path. For this purpose silicon lenses and antennas are replaced by 25 μm-sized pinholes. The transmitted laser beam is then guided by two parabolic mirrors from the source pinhole to the receiver pinhole where it overlaps with the

receiver laser beam. Therefore, the maximum alignment tolerance is only the size of the pinhole of 25 μm, i. e. a fraction of the THz wavelength. This ensures high alignment accuracy. After the alignment procedure, the silicon lenses are inserted with their center aligned to the laser spot. As long as the devices are well aligned to the center of the silicon lenses, the THz beam will follow the same path as the laser beam. To ensure a high reproducibility, the devices are mounted on a xy-stage, while the silicon lens is fixed.

The devices are connected by probe needles, allowing for fast sample exchange. The THz source is biased with a square-wave voltage of up to 50 V at a modulation frequency of 8.6 kHz for lock-in detection (Model 7625, Signal Recovery). The setup is operated under ambient conditions without nitrogen purging.

The parameters of the photoconductors used for testing the system are summarized in Table 1. The samples are grown on the <100> surface of a semi-insulating GaAs substrate in a Varian Mod Gen II molecular beam epitaxy system [31]. The low temperature growth of 1.5 μm thick LT GaAs was followed by an in situ anneal at 600°C for 10 minutes under As overpressure. The lifetime of the photo-generated carriers in LT GaAs was studied using femtosecond time-resolved reflectivity measurements by an all optical pump/probe system featuring $\sim$70 fs temporal resolution [32]. The lowest growth temperature of 200°C led to a carrier lifetime in the range of 150 fs while the lifetime of the 300°C sample was in the range of 270 fs. However, measurements at several positions on the wafers showed

TABLE 1 DC materials properties of the photoconductive samples. The photocurrent responsivity was measured under pulsed operation using the 780 nm laser as described in the text

Sample	T200	T225	T250	T275	T300
Growth T [°C]	200	225	250	275	300
DC Resistance [MΩ/$\square$]	495 ± 23	362 ± 5	202 ± 18	114 ± 4	110 ± 2
Responsivity at 10 V [A/W]	5.2×10^{-5}	7.6×10^{-5}	9.7×10^{-5}	1.5×10^{-4}	2.0×10^{-4}

Excitation with a CW laser at 850 nm yielded about 37 ± 5 times higher responsivities.
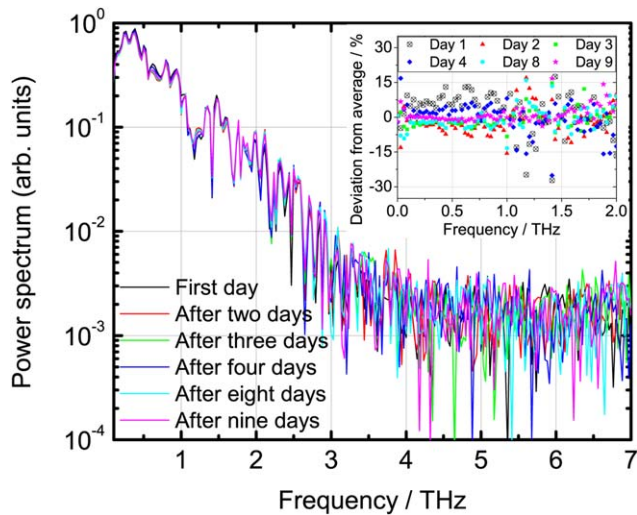
Figure 2 Frequency spectra of device T275 measured on several days with a source bias of 30 V, source laser power of 25 mW, and detector laser power 17 mW. Between individual measurements the device was removed from the setup and subsequently remounted again. Inset: fluctuations of the measured power spectral density with respect to the average. For this measurement, the emitter uses a coplanar stripline antenna while the receiver uses an H-dipole. [Color figure can be viewed at wileyonlinelibrary.com]

fluctuations of the carrier lifetime in the range of 50 fs for all samples, with no clear trend at intermediate growth temperatures. This further strengthens the requirement of a measurement system for direct comparison of sample performance of processed photoconductors with little systematic error.

Such short carrier lifetimes are optimally suited for THz generation and detection. H-dipoles with a geometry as depicted in Figure 1(b) (gap size $5 \times 10~\mu m^2$, dipole length 200 μm, wiring length and width of 1 mm and 20 μm, respectively) are processed with UV contact lithography, followed by metallization with Ti/Au=10 nm/300 nm, for most measurements. For some measurements, also coplanar stripline (CPS) antennas with a CPS spacing of 200 μm were used [see Fig. 1(c)].
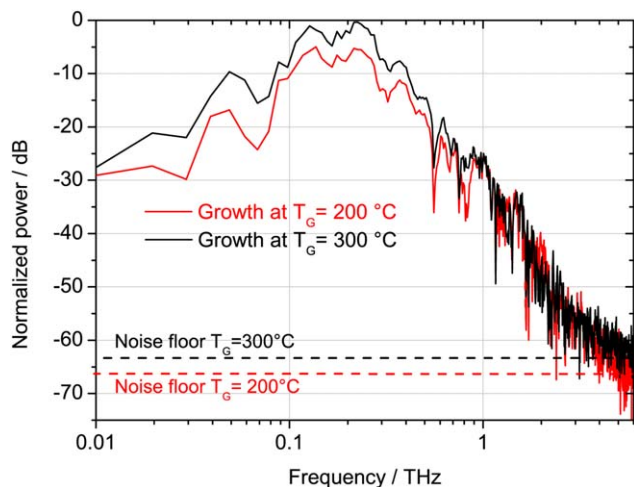
We demonstrate the excellent performance of the setup by remounting the same device and comparing the peak-peak field amplitude of the pulses. The 3 h repeatability error is 1.9% ± 0.2% (standard deviation). The same comparison over a time span of nine days yields a standard deviation of 2.6%. The slightly larger value for the long-term measurement may be due to laser power or humidity variations. The standard deviation of 2.6% in THz field corresponds to a standard deviation of 5.2% in THz power.

For comparing the performance of various samples, in particular the frequency-dependent roll-off behavior, it is important that not only the amplitude is stable but also that all frequency components are imaged the same way: a misalignment in the THz path has a severe impact on the frequency characteristic. Figure 2 shows the spectra recorded at each day with excellent agreement between individual measurements. The device was removed and remounted for each measurement. The inset shows the deviation from the average in the range of 0.1 THz – 2 THz, where most of the power is concentrated and the dynamic range is greater than 15 dB in order to exclude noise contributions. The deviation shows no frequency dependence. Hence, the setup offers excellent reproducibility and is therefore well suited to compare the spectral performance of photoconductors.

3. APPLICATION FOR MATERIAL CHARACTERIZATION

Material characterization is highly important in order to evaluate the quality of the photoconductors. Material parameters obtained from DC measurements are often insufficient to determine the THz performance. For instance, the photoconductive gain, which could be determined from DC photocurrents, differs strongly for pulsed and CW measurements (see Table 1). Hall data on highly resistive samples are often afflicted to large error bars. Saturation effects cannot be determined by DC characterization at all. Only a direct comparison of emitted and detected THz spectra allows for evaluation of the device performance, requiring a stable setup with sufficient repeatability of the measurements. In order to demonstrate the high stability of the presented system, we therefore compare the THz performance of the five samples under test. Figure 3 shows the spectra for T200 and T300 when used as detectors. At low frequencies, the detected field

Figure 3 T200 and T300 used as detectors. The spectra are averaged over five measurements. T300 shows a higher response at low frequencies and approaches that of T200 at frequencies around 1 THz. [Color figure can be viewed at wileyonlinelibrary.com]
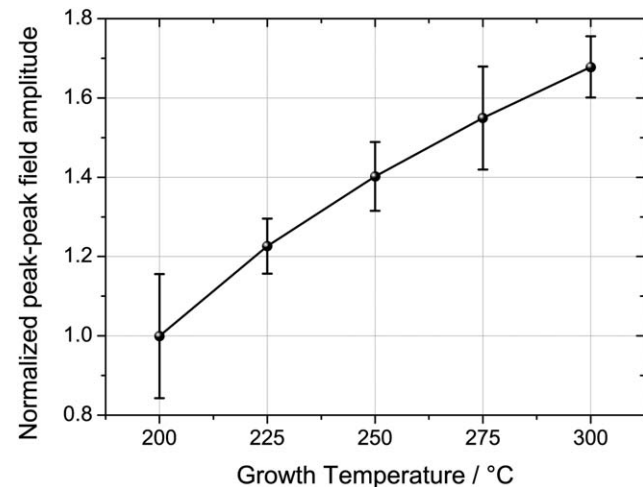

Figure 4 Normalized peak to peak amplitudes of various emitters as a function of growth temperature. The emitter antennas were characterized while the detector remains unchanged. Each growth temperature was measured on five individual samples

amplitude, E_{THz}, is proportional to the photoconductive gain, g, as $E_{THz} \sim I_{THz} \sim gP_L$, with the laser power P_L. Sample T300 has about 5 dB higher sensitivity at low frequencies (<200 GHz). This shows that T300 has 2.5 dB (factor 1.78) higher gain, which is in agreement with the expected longer carrier lifetime, τ_{rec}, for elevated growth temperatures, since $g \sim \tau_{rec}$. The sensitivities of both samples become comparable at frequencies above ~ 1 THz. Since the detection process is a convolution of the laser pulse and the material response [33], the finite carrier lifetime ($\tau_{rec} \sim 150$ fs) will indeed have an impact on the spectra approximately at 1 THz where the sensitivities of both detectors converge [18]. Further, the noise floor of T300 is 2.63 dB (factor 1.83) higher than that of T200, potentially attributed to the lower device resistance (see Table 1). The better performance of T300 at low THz frequencies is almost compensated by the smaller noise level of T200. Therefore, T200 is better suited as detector for most applications. In contrast, T300 should perform very well as THz source.

This is confirmed by a comparison of all samples when used as emitters as shown in Figure 4. The peak-peak amplitude increases by a factor of 1.68 for sample T300 as compared to sample T200. This is in perfect agreement with the gain increase found from implementation as detector and with the literature [34].

4. CONCLUSION

We have presented a setup for a systematic study of THz photoconductors under pulsed operation. The intra-day reproducibility error is in the range of 1.9% while the reproducibility within 9 days is 2.6%. This includes not only absolute power stability but also reproducibility of the spectra by eliminating alignment errors that alter the transfer function from sender to receiver. In order to demonstrate the full capabilities of the system, we investigated samples from five LT GaAs wafers, grown at temperatures between 200°C and 300°C, in a systematic manner. The obtained results are in good agreement with previous studies on the same material system. The system allows for quality control of photoconductors with minimum comparison error.

REFERENCES

1. A. Mitsuishi, Progress in far-infrared spectroscopy: Approximately 1890 to 1970, J Infrared Milli Terahz Waves 35 (2013), 243–281.

2. K.-E. Peiponen, A. Zeitler, and M. Kuwata-Gonokami (Eds): Terahertz spectroscopy and imaging, Springer, Berlin/Heidelberg, 2013.

3. T. Kürner and S. Priebe, Towards THz communications-status in research, standardization and regulation, J Infrared Milli Terahz Waves 35 (2013), 53–62.

4. C. Jördens, M. Scheller, S. Wietzke, D. Romeike, C. Jansen, T. Zentgraf, K. Wiesauer, V. Reisecker, and M. Koch, Terahertz spectroscopy to study the orientation of glass fibres in reinforced plastics, Compos Sci Technol 70 (2010), 472.

5. P.U. Jepsen, D.G. Cooke, and M. Koch, Terahertz spectroscopy and imaging—Modern techniques and applications, Laser Photon Rev 5 (2011), 124.

6. D. Grischkowsky, S. Keiding, M. van Exter, and C. Fattinger, Far-infrared time-domain spectroscopy with terahertz beams of dielectrics and semiconductors, J Opt Soc Am B 7 (1990), 2006–2015.

7. P.U. Jepsen, R.H. Jacobsen, and S.R. Keiding, Generation and detection of terahertz pulses from biased semiconductor antennas, J Opt Soc Am B 13 (1996), 2424–2436.

8. M. Tani, S. Matsuura, K. Sakai, and S. Nakashima, Emission characteristics of photoconductive antennas based on low- temperature-grown GaAs and semi-insulating GaAs, Appl Opt 36 (1997), 7853–7857.

9. Q. Wu and X.C. Zhang, Free space electro-optic sampling of terahertz beams, Appl Phys Lett 67 (1995), 3523.

10. C. Winnewisser, P.U. Jepsen, M. Schall, V. Schyja, and H. Helm, Electro-optic detection of THz radiation in LiTaO$_3$, LiNbO$_3$ and ZnTe, Appl Phys Lett 70 (1997), 3069.

11. R.J.B. Dietz, N. Vieweg, T. Puppe, A. Zach, B. Globisch, T. Göbel, P. Leisching, and M. Schell, All fiber-coupled THz-TDS system with kHz measurement rate based on electronically controlled optical sampling, Opt Lett 39 (2014), 6482–6485.

12. S. Busch, T. Probst, M. Schwerdtfeger, R. Dietz, J. Palací, and M. Koch, Terahertz transceiver concept, Opt Exp 22 (2014), 16841–16846.

13. D.H. Auston, K.P. Cheung, and P.R. Smith, Picosecond photoconducting Hertzian dipoles, Appl Phys Lett 45 (1984), 284–286.

14. C. Fattinger and D. Grischkowsky, Terahertz beams, Appl Phys Lett 54 (1989), 490–492.

15. J.E. Pedersen, V.G. Lyssenko, J.M. Hvam, P. Uhd Jepsen, S.R. Keiding, C.B. Sorensen, and P.E. Lindelof, Ultrafast local field dynamics in photoconductive THz antennas, Appl Phys Lett 62 (1993), 1265–1267.

16. E.R. Brown, K.A. McIntosh, K.B. Nichols, and C.L. Dennis, Photomixing up to 3.8 THz in low-temperature grown GaAs, Appl Phys Lett 66 (1995), 285–287.

17. E.R. Brown, THz generation by photomixing in ultrafast photoconductors, Int J High Speed Electron Syst 13 (2003), 497–545.

18. E. Castro-Camus, L. Fu, J. Lloyd-Hughes, H.H. Tan, C. Jagadish, and M.B. Johnston, Photoconductive response correction for detectors of terahertz radiation, J Appl Phys Lett 104 (2008), 053113.

19. S. Preu, G.H. Döhler, S. Malzer, A.C. Gossard, and L.J. Wang, Tunable, continuous-wave photomixer sources and applications, J Appl Phys 109 (2011), 061301.

20. J. Mangeney, THz photoconductive antennas made from ion-bombarded semiconductors, J Infrared Milli Terahz Waves 33 (2012), 455.

21. D.C. Driscoll, M.P. Hanson, A.C. Gossard, and E.R. Brown, Ultrafast photoresponse at 1.55 μm in InGaAs with embedded semimetallic ErAs nanoparticles, Appl Phys Lett 86 (2005), 051908.

22. S. Preu, M. Mittendorff, H. Lu, H.B. Weber, S. Winnerl, and A.C. Gossard, 1550 nm ErAs:In(Al)GaAs large area photoconductive emitters, Appl Phys Lett 101 (2012), 101105.

23. C.W. Berry, M.R. Hashemi, S. Preu, H. Lu, A.C. Gossard, and M. Jarrahi, High power terahertz generation using 1550 nm plasmonic photomixers, Appl Phys Lett 105 (2014), 011121.

24. R.J.B. Dietz, M. Gerhard, D. Stanze, M. Koch, B. Sartorius, and M. Schell, THz generation at 1.55 μm excitation: six-fold increase in THz conversion efficiency by separated photoconductive and trapping regions, Opt Exp 19 (2011), 25911.

25. R.J.B. Dietz, B. Globisch, M. Gerhard, A. Velauthapillai, D. Stanze, H. Roehle, M. Koch, T. Göbel, and M. Schell, 64 µW pulsed THz emission from growth optimized InGaAs/InAlAs heterostructures with separated photoconductive and trapping regions, Appl Phys Lett 103 (2013), 061103.

26. V. Paebutas, et al. Terahertz time-domain-spectroscopy system based on femtosecond Yb:fiber laser and GaBiAs photoconducting components, Appl Phys Lett 97 (2010), 031111.

27. J. Sigmund, C. Sydlo, H.L. Hartnagel, N. Benker, H. Fuess, F. Rutz, T. Kleine-Ostmann, and M. Koch, Structure investigation of LTG-GaAsSb as a new material for photoconductive THz antennas, Appl Phys Lett 87 (2005), 252103.

28. O. Hatem, J.R. Freeman, J.E. Cunningham, P.J. Cannard, M.J. Robertson, E.H. Linfield, A.G. Davies, and D.G. Moodie, Generation of Terahertz radiation from Fe-doped InGaAsP using 800 nm to 1550 nm pulsed laser excitation, J Infrared Milli Terahz Waves (2015), 1–11.

29. N. Vieweg, M. Mikulics, M. Scheller, K. Ezdi, R. Wilk, H.W. Hübers, and M. Koch, Impact of the contact metallization on the performance of photoconductive THz antennas, Opt Exp 16 (2008), 19695.

30. I.S. Gregory, C. Baker, W.R. Tribe, M.J. Evans, H.E. Beere, E.H. Linfield, A.G. Davies, and M. Missous, High resistivity annealed

low-temperature GaAs with 100 fs lifetimes, Appl Phys Lett 83 (2003), 4199.

31. M. Mikulics, X. Zheng, R. Adam, R. Sobolewski, and P. Krodos, High-speed photoconductive switch based on low-temperature GaAs transferred on SiO$_2$-Si substrate, IEEE Photon Technol Lett 15 (2003), 528–530.

32. M. Mikulics, M. Marso, I.C. Mayorga, R. Gusten, S. Stanček, P. Kováč, S. Wu, X. Li, M. Khafizov, R. Sobolewski, E.A. Michael, R. Schieder, M. Wolter, D. Buca, A. Förster, P. Kordoš, and H. Lüth, Photomixers fabricated on nitrogen-ion-implanted GaAs, Appl Phys Lett 87 (2005), 041106.

33. S. Preu, A unified derivation of the Terahertz spectra generated by photoconductors and diodes, J Infrared Milli Terahz Waves 35 (2014), 998–1010.

34. J. Darmo, T. Müller, W. Parz, J. Kröll, G. Strasser, and K. Unterrainer, Few-cycle terahertz generation and spectroscopy of nanostructures, Phil Trans R Soc Lond A 362 (2004), 251–262.

3.4 Photoconductive LT-GaAs Terahertz Antennas: Correlation Between Surface Quality and Emission Strength

O.M. Abdulmunem, K. I. Hassoon, J. Völkner, M. Mikulics, K.I. Gries, K. Volz, J.C. Balzer, J. Infrared Milli Terahz Waves, 38(5):574–582, DOI:10.1007/s10762-016-0353-y (2017).

3.4.1 Abstract:

We investigate the influence of the surface properties of a low-temperature-grown GaAs photoconductive antenna on the THz emission strength, using a specially designed THz TDS system. The system allows us to excite six different positions along the 10 μm gap of a coplanar stripline antenna with a length of 10 mm without changing the alignment of the optical or THz beam path. A comparison to the surface roughness and the grain size which are extracted from an atomic force and a scanning electron microscope is given.

3.4.2 The author's contribution:

The experimental part of this publication was conducted by me. The final results achieved in cooperation with K. I. Hassoon, J. Völkner and K. I. Gries related to SEM and FAM experimental work and helped to writing the corresponding sections in the manuscript. The manuscript was written by K. I. Hassoon, J.C. Balzer and me. In fact all co-authors contributed to this publication and helped to write and improve the manuscript.

CrossMark

Photoconductive LT-GaAs Terahertz Antennas: Correlation Between Surface Quality and Emission Strength

O. M. Abdulmunem[1] · K. I. Hassoon[2] · J. Völkner[3] ·
M. Mikulics[4] · K. I. Gries[1] · J. C. Balzer[1]

Abstract We investigate the influence of the surface properties of a low-temperature-grown GaAs photoconductive antenna on the terahertz (THz) emission strength, using a specially designed THz time-domain spectroscopy system. The system allows us to excite six different positions along the 10 μm gap of a coplanar stripline antenna with a length of 10 mm without changing the alignment of the optical or THz beam path. A comparison to the surface roughness and the grain size which are extracted from an atomic force and a scanning electron microscope is given.

1 Introduction

Terahertz (THz) time-domain spectroscopy (TDS) has proven to be a useful tool for basic research in physics [1–3]. Furthermore, many applications for real world problems have been demonstrated [4–9]. A key element of most THz TDS is the photoconductive antenna. It converts the bandwidth of a near-infrared femtosecond laser into the THz frequency range and needs a low carrier lifetime. At first, photoconductive antennas were fabricated on the basis of radiation-damaged silicon-on-sapphire in order to realize a low carrier lifetime [10]. Later,

✉ J. C. Balzer
jan.balzer@physik.uni-marburg.de

1   Department of Physics and Materials Science Center, Philipps-University of Marburg, Hans-Meerwein-Straße 6, 35032 Marburg, Germany

2   Department of Applied Sciences, University of Technology, Baghdad, Iraq

3   Faculty of Physics, Philipps University Marburg, Renthof 7, 35037 Marburg, Germany

4   Peter Grünberg Institute (PGI-9), Forschungszentrum Jülich GmbH, 52425 Jülich, Germany

low-temperature-grown (LT) GaAs became popular [11]. Since then, several other semiconductor systems have been explored and optimized [12–14], in particular for the excitation with lower photon energies. Nevertheless, LT-GaAs is still a key material. Besides, it is used for the fabrication of photomixers which are essential in systems for continuous-wave THz spectroscopy [15–17].

LT-GaAs is typically grown by molecular beam epitaxy (MBE) at a relatively low temperature in the range of $0.34 < T/T_m < 0.38$, where T and T_m are the absolute growth and melting temperatures, respectively [18]. Among other semi-insulating materials, LT-GaAs has a very short carrier lifetime and a high breakdown electric field [19]. It has a weaker crystallinity than GaAs grown at regular temperatures. In particular, the low-temperature growth can lead to polycrystalline grains or pyramid-like structures accompanied by stacking faults and dislocations [20].

In the past, there have been many attempts to optimize the material quality of LT-GaAs [21] and the antenna structures [22] including metallization [23]. One aspect has not been investigated yet: material inhomogeneities which can arise during growth could lead to varying emission strength on the wafer. This is the aspect we studied in the framework of this work. For this, we have built a setup to test THz antennas with high reproducibility. If the antenna structure contains a dipole with a gap, the excitation is restricted to the small gap area which does not allow a systematic characterization of the material. Hence, we prefer to investigate a coplanar stripline (CPS) as emitter antenna. This gives us the opportunity to vary the position of the optical excitation spot between the striplines. By doing so, regions of different growth quality can be explored. The results are then compared to atomic force microscopy (AFM) and scanning electron microscope (SEM) images in order to investigate if there is a correlation between THz performance and surface properties of the semiconductor material.

2 Experimental Setup

Traditional CPS antennas used for THz generation have a relatively simple design. In our case, they are fabricated from a semi-insulating photoconductor with two metal electrodes which are spaced several microns apart as shown in Fig. 1. The metal strips or electrodes have typically a width between 5 and 25 μm and a length of several millimeters. In order to study the THz performance of the antenna for multiple regions, we used a CPS antenna with long striplines. However, our approach is also suitable for shorter CPS antennas since the optical spot size is small compared to the length of regular antennas.

Fig. 1 Schematic of the used CPS antenna. The striplines are 10 mm long and the gap is 10 μm wide. For further investigations, we divided the antenna into six different measurement positions along the gap: P1–P6. For the position between P2 and P3, no complete data set could be acquired due to technical issues
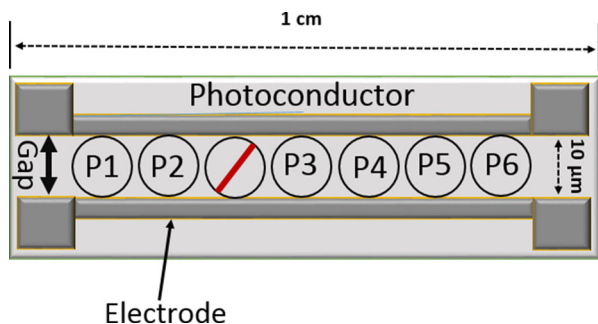
Figure 1 shows a schematic of the CPS antenna. We investigated the antenna at six different positions within the gap. We denote them as P1 to P6, where P3 corresponds to the central position along the striplines. Note that there have been technical issues preventing the acquisition of a full set of data between P2 and P3 as indicated in Fig. 1. On the one hand, we determined the amplitude of the emitted THz pulse. On the other hand, we investigated the structural quality of the material at these positions using AFM and SEM.

The device structure to be tested consists of an LT-GaAs active layer which was grown on a 2-in. semi-insulating GaAs wafer by molecular beam epitaxy (MBE) technique using a Varian GEN-II equipment [24]. They were prepared as follows: at first, a 300-nm thick AlAs layer was grown on top of the semi-insulating GaAs substrate, followed by a 1.5-µm thick LT-GaAs layer grown at a substrate temperature of 200 °C (thermocouple reading only). The structures were in situ isothermally annealed at 600 °C for 10 min under local As overpressure.

A standard Ti/Au 10/170 nm layer system was used for metallization [25]. The length of the stripe lines was 10 mm, while the gap measured 10 µm. The current–voltage (I–V) characteristics with and without 850 nm continuous-wave light illumination of the LT-GaAs CPS antennas were measured immediately after the fabrication. The I–V curves exhibited an ohmic behavior in the bias range from 1 V to below 80 V. Space-charge effects were not observed, which indicates an efficient suppression of the high-field region near the contacts. The dark currents were 2×10^{-9} A at ~10 V and $\leq 10^{-7}$ A at 100 V. The breakdown voltage was in the range of (270–300) kV/cm, similar to what we have observed for our other LT-GaAs-based devices [26].

The measurements were performed with a THz TDS system which was built to characterize photoconductive THz emitters and detectors in a systematic manner with high repeatability. Figure 2 shows a schematic of the setup which is built vertically (in contrast to most THz TDS systems) which allows an easy exchange of photoconductive antennas. The THz path contains two parabolic mirrors. The system is driven by a 780-nm mode-locked Ti:sapphire laser with a pulse duration of 150 fs and a repetition rate of 80 MHz. Both emitter and detector antennas are placed on top of a hemispherical silicon lens that is mounted on a high precision stage which allows for 3D alignment in order to position the devices in the focal point of the optical beam. While the silicon lens is fixed, the devices which are contacted by metallic needles are mounted on an XY stage. This setup can reproduce measurements of the THz amplitude with a higher accuracy than 3% even if the sample is demounted and mounted several times over several days. A detailed description of the setup is given elsewhere [27].

The emitter antenna which is biased by a square-wave voltage of 30 V and illuminated with an average power of 25 mW can be freely moved on top of the silicon lens by using micrometer screws. Figure 2a shows the situation where the laser spot is positioned in the center of the CPS antenna (P3). Figure 2b depicts schematically what happens if the antenna is moved to the left side: now a different position is illuminated (P4), while the alignment of the THz path including the silicon lens is unchanged. In this way, the antenna can be systematically scanned, with the lateral resolution given by the spot size. As for the detector antenna, we use a dipole antenna excited by 18 mW average power.

For AFM measurements, an SPM5500-AFM instrument (Agilent) was used. It was operated in tapping mode at ambient conditions applying HQ:NSC15/AlBS cantilevers (MikroMasch) with the nominal resonance frequency of 325 kHz. Special care had to be taken to avoid temporal collection of superficial nanosized contaminants present on the sample surface that were readily attracted to the tip and in the consequence made structures appear multiple and/or blurred.
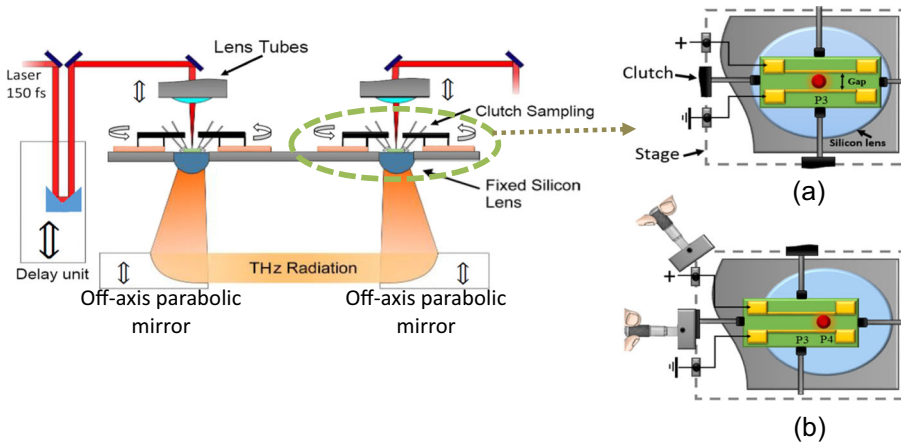
Fig. 2 Overview of the used THz TDS system. The vertical orientation of the setup enables the possibility to move the antenna in relation to the optical excitation. **a** and **b** illustrate the scanning along the gap of the emitter antenna, while the detector antenna is unchanged

SEM secondary electron images have been acquired using a JEOL JIB 4601F working with an acceleration voltage of 5 kV.

3 Results

In this section, we will present our results from the aforementioned THz setup and compare them with topographic results obtained from the AFM and SEM measurements. As described before, all measurements originate from the same sample at different positions. Since we want to see if there is a correlation between the THz emission strength and the surface properties of the photoconductive antenna, we have to assure that we have a spatial overlap between the different measurement methods. Therefore, we use the central position of the antenna as a reference point. From this point, we move the antenna parallel to the stripe lines by exact 1.14 mm to the left and right. The distance was measured by the scale of the micrometer screw. In this way, we measured complete THz TDS traces for the six different positions. In order to verify the system stability, 20 traces were measured over a period of 20 min. As a measure of the THz emission strength, we considered the peak-to-peak (PTP) value of the measured traces. During all measurements, the average laser power was kept constant to 25 mW (18 mW) for the emitter (detector). The results of the stability measurements for the six different measurement positions are depicted in Fig. 3.

From these measurements, it can be seen that the system is stable within the time window of 20 min. The highest standard deviation of approximately 2% was measured for position P3. The periodic fluctuations in the traces can be attributed to the cycle of the air conditioning used in the laboratory: Even a small change in environmental temperature can slightly misalign the optical part of the THz TDS system and hence influence the signal amplitude. Further, all positions show different mean PTP THz amplitudes which can be attributed to the properties of the semiconductor at that specific position. The lowest value was measured to be 0.472 nA for position P3, and the highest value was measured to be 0.756 nA for position P6. That means that the surface conditions of the antenna structure have a considerable impact on the strength

Fig. 3 Measured PTP amplitude of the THz trace over a duration of 20 min for the six different positions. It can be seen that the highest value was measured for region P6, while the lowest value was measured for region P3. The overall stability of the system is quite high since the highest standard deviation is less than 2%
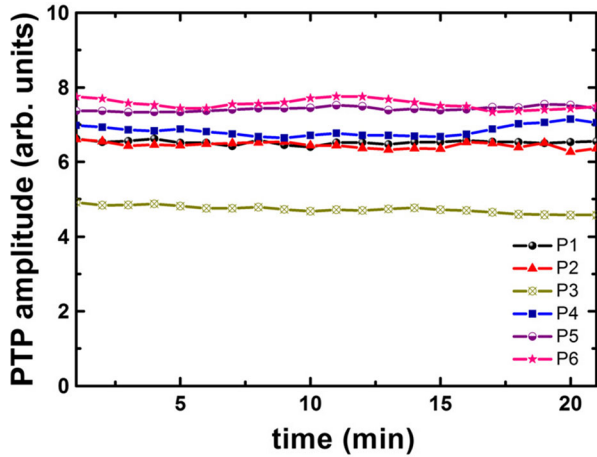
of the emitted THz radiation which is in our case larger than 60% in PTP THz amplitude. Detailed information on the mean PTP THz amplitude, variance, and standard deviation are given in Table 1.

As a next step, we were interested in the surface properties of the antenna. The surface roughness for the six different regions of the antenna was characterized by means of AFM. In addition, SEM images were taken in order to estimate the grain size. The images taken by AFM can be seen in the top row of Fig. 4.

The AFM images have a size of 2 μm × 2 μm, and the scale bar represents 500 nm. The surface height is encoded in color. On the base of these images, the root mean square (RMS) roughness for each position on the antenna was calculated. The values for RMS roughness are given in Table 1. Position P3 has with 8.5 nm the highest roughness, while section P6 has the lowest one. Additionally, an exemplary line scan (fine white line in the AFM images in Fig. 4) for each position is depicted in Fig. 5a to illustrate different height profiles. The line scans were chosen individually for each image to display average and distinct features of the topography.

Besides the height profile, the grain size is of interest. The grain size was calculated from the SEM images, which were taken at two different magnifications. For region P3, the SEM image with the lower magnification shows a crack and a feature which could be a cavity. Further SEM images which are not shown in Fig. 4 exhibited also surface defects.

Table 1 Mean PTP THz amplitude (M_t), variance (V_t), standard deviation (S_d), geometric roughness (S_q), and mean grain size (G_s) for the six different measurement zones. M_t, V_t, and S_d extracted from the THz TDS measurements. The surface roughness was calculated from the AFM images and the grain size from the SEM images

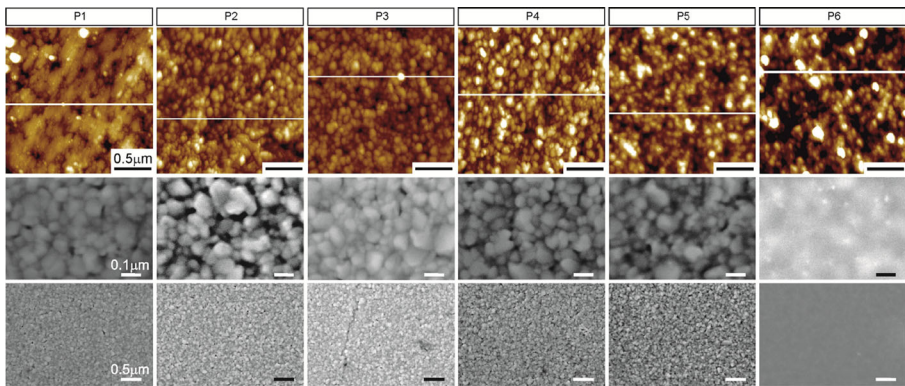| Position	M_t (nA)	$V_t \times 10^{-2}$(nA)^2	S_d (nA)	S_q (nm)	G_s (nm)
P1	0.652	0.00293	0.00542	5.82	40
P2	0.644	0.00705	0.00840	5.12	56
P3	0.472	0.00917	0.00958	8.5	64
P4	0.683	0.00210	0.00458	6.97	54
P5	0.742	0.00382	0.00618	5.17	34
P6	0.756	0.00162	0.00402	4.96	26

Fig. 4 AFM (*first row*) and SEM (*second and third rows*) images taken for the six different measurement positions. The magnification for the images presented in a row is the same. The *fine white lines* in the AFM images represent the line scans

The determination of the grain size was done mostly manually or by the program ImageJ [28]. Two perpendicular lines were fitted into each grain in order to determine its size. The arithmetic mean of both lines corresponds to the assumed grain size. Figure 5b shows the distribution of the grain size for region P2. It can be seen that the grain size follows a normal distribution and can hence be fitted by a Gaussian function. In this case, the mean value for the grain size is 56 nm with a standard deviation of 5.65 nm. The information about the mean grain size of each region can be found in Table 1. Again, the largest mean grain size was found for region P3, while the lowest grain size was found for position P6. Note that the AFM (2 μm × 2 μm) and SEM (3.6 μm × 2.5 μm) images capture only the central part of the excited area since the spot size was around 9 μm.

A quantitative comparison of the measured surface and THz properties is given in Fig. 6. The mean PTP THz amplitude (black line, triangle) has its minimum for position P3, where the roughness (red line, circle) and grain size (blue line, square) have their maximum. The highest
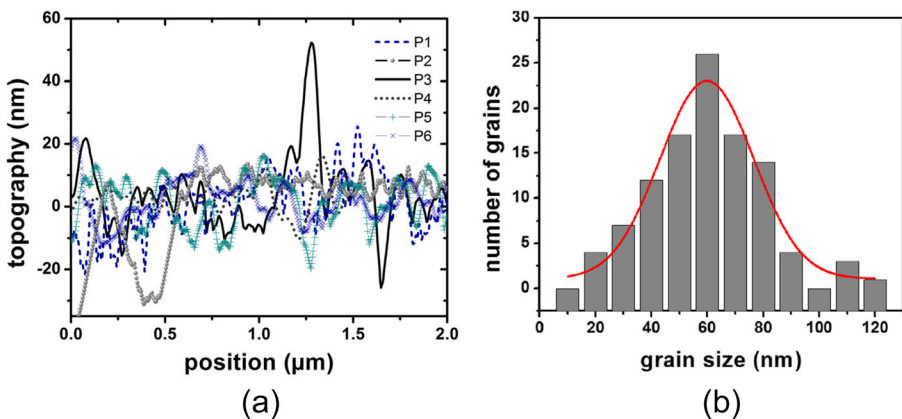

Fig. 5 **a** Exemplary illustration of the topography of the six regions extracted from the AFM images. The RMS roughness given in Table 1 was calculated from the complete image. **b** Distribution of the grain size obtained from the SEM data for position P2 with a Gaussian fit. The mean grain size is 56 nm with a standard deviation of 8.35 nm
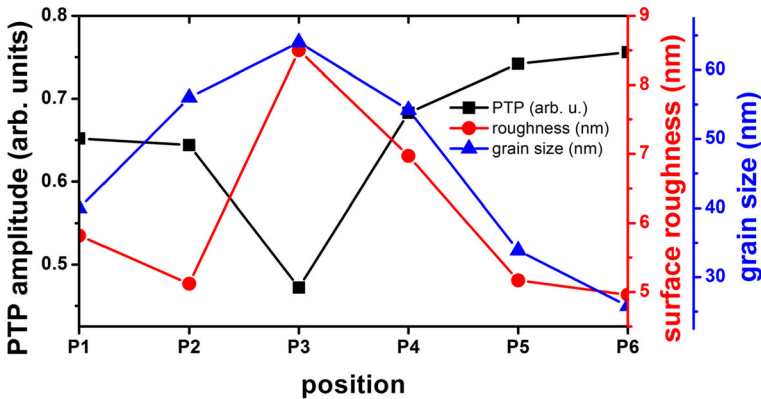
Fig. 6 Comparison of the PTP THz amplitude (*black squares*), the topographical roughness extracted from the AFM images (*red circles*), and the grain size extracted from the SEM images (*blue triangles*). It can be seen that a strong THz signal corresponds to a small grain size and a small roughness

PTP THz amplitude was measured for position P6 which coincides with the smallest grain size and the lowest roughness. This correlation can be seen for all six positions. An interesting feature can be observed for P1. A comparison between positions P1 and P2 reveals that an increase in surface roughness can be compensated by a reduction in grain size: the PTP THz amplitude slightly increases from position P2 to P1, although the roughness increases.

These results reveal a clear correlation between the surface properties of a semiconductor used for a photoconductive antenna and the emitted THz intensity. In particular, high THz intensities are favored by a smooth surface with small grains.

According to a theoretical model for polycrystalline materials, the barrier height, Φ_{BH}, between different grains is given by $\Phi_{BH} = qNG_s^2/8\varepsilon$, where q, N, G_s, and ε are the elementary charge, the concentration of impurity atoms, the grain size, and the permittivity [29], respectively. The current density, J_{th}, which is a key parameter for the THz PTP amplitude, can be described as $J_{th} \propto \exp[-q\Phi_{BH}/k_BT]$, where k_B is the Boltzmann constant and T the temperature.

(a)   (b)
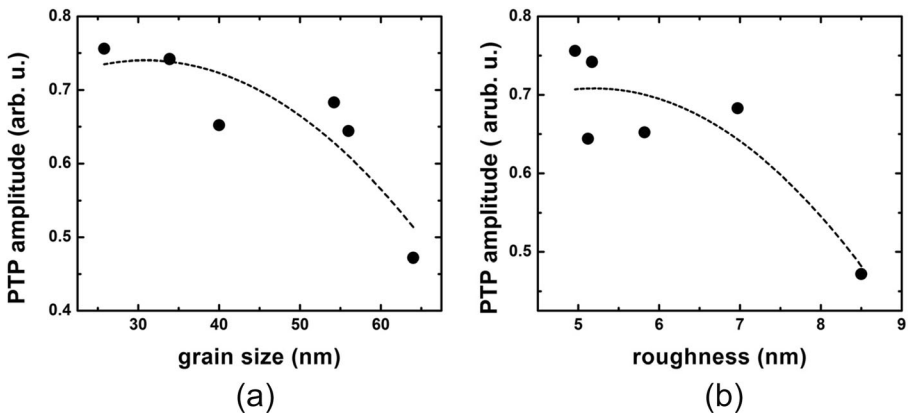
Fig. 7 The THz PTP amplitude as a function of the grain size (**a**) and the roughness (**b**). The *dashed lines* correspond to a second-order polynomial fit and serves as a guide to the eye

From this empirical formula follows that there is a nonlinear correlation between the PTP amplitude and the grain size which favors small grain sizes.

In order to illustrate this relation, Fig. 7a shows the THz PTP amplitude as a function of the grain size. As the above described model predicts, a lower grain size leads to higher THz PTP amplitude. The relation is nonlinear and seems to saturate for small grain sizes. This behavior is also supported by the model. A similar trend is evident for the relation between the THz PTP amplitude and the roughness, as depicted in Fig. 7b. The dashed line in both figures is a second-order polynomial fit which serves as a guide to the eye.

4 Conclusions

In this paper, we investigated the correlation between THz emission strength and the surface properties of an LT-GaAs photoconductive antenna. The THz characteristics were measured with a highly stable setup, which allowed exciting a 10-mm long CPS antenna along the gap without changing the alignment of the optical or THz beam path. The surface properties were quantified by the roughness and the grain size. The roughness was extracted from AFM measurements and the grain size from SEM measurements. A comparison of the THz emission strength in form of the PTP THz amplitude and the surface properties showed a strong nonlinear correlation: a smaller grain size and a smoother surface increase the PTP THz amplitude. These results can be used in the future to optimize the performance of THz antennas.

References

1. S. Leinß, T. Kampfrath, K. V. Volkmann, M. Wolf, J. T. Steiner, M. Kira, S. W. Koch, A. Leitenstorfer, and R. Huber, Terahertz coherent control of optically dark paraexcitons in Cu2O, Phys. Rev. Lett. **101**, 246401 (2008).
2. S. Wietzke, C. Jansen, M. Reuter, T. Jung, D. Kraft, S. Chatterjee, B. M. Fischer, and M. Koch, Terahertz spectroscopy on polymers: A review of morphological studies, J. Mol. Struct. **1006**, 41–51 (2011).
3. I. Ivanov, M. Bonn, Z. Mics, and D. Turchinovich, Perspective on terahertz spectroscopy of graphene, EPL Europhysics Lett. **111**, 67001 (2015).
4. M. Herrmann, M. Tani, K. Sakai, and R. Fukasawa, Terahertz imaging of silicon wafers, J. Appl. Phys. **91**, 1247–1250 (2002).
5. S. Wietzke, C. Jördens, N. Krumbholz, B. Baudrit, M. Bastian, and M. Koch, Terahertz imaging: A new non-destructive technique for the quality control of plastic weld joints, J. Eur. Opt. Soc. **2**, 2–6 (2007).
6. C. Jördens and M. Koch, Detection of foreign bodies in chocolate with pulsed terahertz spectroscopy, Opt. Eng. **47**, 37003 (2008).
7. A. Soltani, S. F. Busch, P. Plew, J. C. Balzer, and M. Koch, THz ATR Spectroscopy for Inline Monitoring of Highly Absorbing Liquids, J. Infrared, Millimeter, Terahertz Waves **37**, 1001–1006 (2016).
8. M. Reuter, O. M. Abdulmunem, J. C. Balzer, M. Koch, and D. G. Watson, Using Terahertz Time-Domain Spectroscopy to Discriminate among Water Contamination Levels in Diesel Engine Oil, Trans. ASABE **59**, 795–801 (2016).
9. R. Gente, S. F. Busch, E.-M. Stubling, L. M. Schneider, C. B. Hirschmann, J. C. Balzer, and M. Koch, Quality Control of Sugar Beet Seeds With THz Time-Domain Spectroscopy, IEEE Trans. Terahertz Sci. Technol. **6**, 1–3 (2016).
10. P. R. Smith, D. H. Auston, and M. C. Nuss, Subpicosecond photoconducting dipole antennas, IEEE J. Quantum Electron. **24**, 255–260 (1988).
11. Y. Cai, I. Brener, J. Lopata, J. Wynn, L. Pfeiffer, J. B. Stark, Q. Wu, X. C. Zhang, and J. F. Federici, Coherent terahertz radiation detection: Direct comparison between free-space electro-optic sampling and antenna detection, Appl. Phys. Lett. **73**, 444 (1998).
12. N. Vieweg, F. Rettich, A. Deninger, H. Roehle, R. Dietz, T. Göbel, and M. Schell, Terahertz-time domain spectrometer with 90 dB peak dynamic range, J. Infrared, Millimeter, Terahertz Waves **35**, 823–832 (2014).

13. M. Suzuki and M. Tonouchi, Fe-implanted InGaAs photoconductive terahertz detectors triggered by 1.56 μm femtosecond optical pulses, Appl. Phys. Lett. **86**, 163504 (2005)

14. S. Preu, M. Mittendorff, H. Lu, H. B. Weber, S. Winnerl, and A. C. Gossard, 1550 nm ErAs:In(Al)GaAs large area photoconductive emitters, Appl. Phys. Lett. **101**, 101105 (2012).

15. E. R. Brown, K. A. McIntosh, F. W. Smith, K. B. Nichols, M. J. Manfra, C. L. Dennis, and J. P. Mattia, Milliwatt output levels and superquadratic bias dependence in a low-temperature-grown GaAs photomixer, Appl. Phys. Lett. **64**, 3311 (1994).

16. S. Matsuura, M. Tani, and K. Sakai, Generation of coherent terahertz radiation by photomixing in dipole photoconductive antennas, Appl. Phys. Lett. **70**, 559 (1997).

17. R. Wilk, F. Breitfeld, M. Mikulics, and M. Koch, Continuous wave terahertz spectrometer as a noncontact thickness measuring device, Appl. Opt. **47**, 3023 (2008).

18. D. A. Murdick, X. W. Zhou, and H. N. G. Wadley, Low-temperature atomic assembly of stoichiometric gallium arsenide from equiatomic vapor, J. Cryst. Growth **286**, 197–204 (2006).

19. S. Gupta, M. Y. Frankel, J. A. Valdmanis, J. F. Whitaker, G. A. Mourou, F. W. Smith, and A. R. Calawa, Subpicosecond carrier lifetime in GaAs grown by molecular beam epitaxy at low temperatures, Appl. Phys. Lett. **59**, 3276 (1991).

20. Z. Liliental-Weber, H. J. Cheng, S. Gupta, J. Whitaker, K. Nichols, and F. W. Smith, Structure and carrier lifetime in LT-GaAs, J. Electron. Mater. **22**, 1465–1469 (1993).

21. S. Verghese, K. a. McIntosh, and E. R. Brown, Optical and terahertz power limits in the low-temperature-grown GaAs photomixers, Appl. Phys. Lett. **71**, 2743 (1997).

22. M. Tani, S. Matsuura, K. Sakai, and S. Nakashima, Emission characteristics of photoconductive antennas based on low-temperature-grown GaAs and semi-insulating GaAs, Appl. Opt. **36**, 7853 (1997).

23. N. Vieweg, M. Mikulics, M. Scheller, K. Ezdi, R. Wilk, H. W. Hübers, and M. Koch, Impact of the contact metallization on the performance of photoconductive THz antennas, Opt. Express **16**, 19695 (2008).

24. M. Mikulics, Xuemei Zheng, R. Adam, R. Sobolewski, and P. Kordos, High-speed photoconductive switch based on low-temperature GaAs transferred on SiO/sub 2/-Si substrate, IEEE Photonics Technol. Lett. **15**, 528–530 (2003).

25. M. Mikulics, S. Wu, M. Marso, R. Adam, A. Forster, A. van der Hart, P. Kordos, H. Luth, and R. Sobolewski, Ultrafast and highly sensitive photodetectors with recessed electrodes fabricated on low-temperature-grown GaAs, IEEE Photonics Technol. Lett. **18**, 820–822 (2006).

26. M. Mikulics, E. A. Michael, R. Schieder, J. Stutzki, R. Güsten, M. Marso, A. van der Hart, H. P. Bochem, H. Lüth, and P. Kordoš, Traveling-wave photomixer with recessed interdigitated contacts on low-temperature-grown GaAs, Appl. Phys. Lett. **88**, 41118 (2006).

27. O. M. Abdulmunem, N. Born, M. Mikulics, J. C. Balzer, M. Koch, and S. Preu, High Accuracy Terahertz Time-Domain System for Reliable Characterization of Photoconducting Antennas, Microw. Opt. Technol. Lett. **59**, 468–472 (2017).

28. C. A. Schneider, W. S. Rasband, and K. W. Eliceiri, NIH Image to ImageJ: 25 years of image analysis, Nat. Methods **9**, 671–675 (2012).

29. J. Y. W. Seto, The electrical properties of polycrystalline silicon films, J. Appl. Phys. **46**, 5247 (1975).

3.5 TiN Nanoparticles for Enhanced THz Generation in TDS systems

3.5.1 Abstract:

By virtue of the surface plasmon resonance effect, plasmonic nanoparticles (NPs) can localize the light field and significantly enhance the performance of some optoelectronic devices. In this work, NPs are employed for an enhanced generation of terahertz radiation from LT-GaAs-based antennas. Therefore, we have prepared plasmonic Titanium Nitride Nanoparticles (TiN NPs) by direct ultrasonication (ULS) and pulsed laser ablation (PLA) techniques. The Zeta potential, particle size, and absorbance were used to characterize the NPs in their colloidal forms in a comparison to commercial Au NPs. A layer of poly-dispersed TiN NPs prepared by PLA and deposited on the surface of an LT-GaAs device shows a significant improvement of terahertz signal generation from these devices with an enhancement of the peak to peak amplitude of 100%.

3.5.2 The author's contribution:

I conducted the experimental part of this publication, being strongly supported by other members of the Marburg group. The manuscript was written by Khaleel Hassoon, Jan Balzer and me. Mahmoud Gaafar, Arash Rahimi-Iman and all co-authors contributed with important ideas, fruitful discussions and corrections to the manuscript. The topics highlighted are mainly by Khaleel Hassoon and me.

CrossMark

TiN Nanoparticles for Enhanced THz Generation in TDS Systems

Oday Abdulmunem [1,2] · Khaleel Hassoon [1] ·
Mahmoud Gaafar [3,4] · Arash Rahimi-Iman [1] ·
Jan C. Balzer [1]

Abstract By virtue of the surface plasmon resonance effect, plasmonic nanoparticles (NPs) can localize the light field and significantly enhance the performance of some optoelectronic devices. In this work, NPs are employed for an enhanced generation of terahertz radiation from LT-GaAs-based antennas. Therefore, we have prepared plasmonic TiN NPs by direct ultrasonication (ULS) and pulsed laser ablation (PLA) techniques. The zeta potential, particle size, and absorbance were used to characterize the NPs in their colloidal forms in a comparison to commercial Au NPs. A layer of polydispersed titanium nitride (TiN) NPs prepared by PLA and deposited on the surface of an LT-GaAs device shows a significant improvement of terahertz signal generation from these devices with an enhancement of the peak to peak amplitude of 100%.

Keywords THz time-domain spectroscopy · Nanoparticles · Photoconductive antenna

1 Introduction

Terahertz technology is a rapidly developing field. Several application areas are foreseen for this technology. One application area will be short-range indoor communication with THz carrier waves [1–3]. Another one is spectroscopy and imaging for security, material science, art

---

✉ Jan C. Balzer
  jan.balzer@physik.uni-marburg.de

[1] Department of Physics and Materials Sciences Center, Philipps-Universität Marburg, Hans-Meerwein-Straße 6, 35032 Marburg, Germany

[2] Department of Physics, Faculty of Science, Al-Mustansiriya University, Baghdad, Iraq

[3] Institute of Optical and Electronic Materials, Hamburg University of Technology, Eißendorfer Str. 38, 21073 Hamburg, Germany

[4] Department of Physics, Faculty of Science, Menoufia University, Menoufia, Egypt

conservation, monitoring of industrial production processes, and plant physiology [4–9]. THz spectroscopy is mostly based on the use of photoconductive antennas (PCA) which are driven by ultrashort laser pulses. This approach has first been introduced by Smith and coworkers in 1988 [10]. The first PCAs used radiation damaged silicon-on-sapphire as a base material. Later, low-temperature-grown (LT)-GaAs became the standard material for excitation with a wavelength around 800 nm [11–14]. Consequently, there have been many attempts to optimize the material quality of LT-GaAs. Furthermore, the impact of the antenna structure has been studied [15]. This also includes the metallization [16]. Besides, many other semiconductor material systems have been explored and optimized [17–20]. Simultaneously, PCAs have been modeled, as the theoretical understanding is a key to the improvement of these devices [21–25].

However, little attempts have been made to utilize plasmonic nanoparticles (PNP) for the enhancement of the optical absorption of the excitation laser. In contrast, PNPs have already been used to enhance the localized surface plasmon resonance in the domain of optoelectronic devices: Pillai et al. observed an eightfold enhancement in electroluminescence from silicon-on-insulator (SI) light-emitting diodes at 900 nm using Ag NPs [26]. Moreover, Derkacs et al. showed an increase of 8.1% in the short-circuit current density and of 8.3% in the energy conversion efficiency in amorphous silicon p-i-n solar cells using Au NPs [27], to give an example. These improvements are caused by transmission of electromagnetic radiation arising from forward scattering by surface plasmon-polariton modes in Au NPs deposited on the amorphous silicon film. The use of plasmonics in the domain of photovoltaic devices has been detailed in a review by Atwater and Polman [28]. In total, both Au and Ag NPs have attracted attention as PNPs with significant localized surface plasmon resonance (LSPR). Although the LSPR of gold and silver NPs is strong, their absorption bandwidth is narrow and the peaks of plasmonic absorption are located far from 800 nm which is a typical excitation wavelength for LT-GaAs-based PCAs. Various efforts have been made to broaden the absorption range of gold and silver NPs [29, 30]. However, Au and Ag NPs are still unsuited for most near-infrared applications. In order to take advantage of LSPR in the field of THz TDS systems, it is necessary to find a material for NPs that absorbs the wavelength of the excitation laser (around 800 nm for LT-GaAs) as much as possible. In their search for alternatives to the commonly used Au and Ag NPs in the and near-infrared (NIR), Guler et al. have found that titanium nitride (TiN) NPs can support a field enhancement comparable to that of Au NPs [31]. This renders TiN NPs an attractive alternative for Au and Ag NPs. According to these findings, putting the proper nanoparticle material with appropriate particle size on the surface of LT-GaAs can localize the electric field of the laser in the forward direction and hence increase the absorption of the substrate. Furthermore, TiN PNPs combine the benefits of showing a high absorbance in the broad range of visible and near-infrared light and featuring a non-toxic composition [32].

Recently, Jooshesh et al. have demonstrated enhanced THz radiation by employing plasmonic structures on the surface of LT-GaAs antennas [33]. The aim of the work was to enhance the two-photon absorption from a 1550-µm fiber laser. More recently, $MnFe_2O_4$ NPs were also used to enhance the THz generation of PCAs [34]. This shows the strong interest in the employment of NPs for improved THz generation from available emitters. In this context, we introduce PNPs made of TiN for an enhanced generation of THz radiation from LT-GaAs-based antennas and demonstrate the improved performance in a THz TDS system. The enhancement ratio of the device's THz signal generation is 100% for a pump power of 20 mW. As part of our study, we have prepared TiN PNPs by direct ultrasonication (ULS)

and pulsed laser ablation (PLA) techniques and compared their features with Au counterparts. To achieve NP-enhanced antennas, we deposited a polydispersed layer of TiN PNPs on the surface of LT-GaAs.

2 Experimental Part

TiN PNPs were prepared using two methods: direct ULS and PLA in water. ULS involved a TiN nanopowder (20 ± 5 nm) from *PlasmaChem*, which was dissolved directly in double-distilled water (DDW). For this technique, the cavitation effect was used to dissociate the NPs using *Branson* ultrasonication equipment (130 W) for 1 h. For the PLA technique, NPs made of TiN were synthesized from a TiN target located in DDW at room temperature as described in the following. The respective TiN target was produced via compression (6 N) of the aforementioned TiN nanopowder. The target was fixed at the bottom of a rotatable (40 rpm) glass vessel containing 1.5 ml of DDW. Ablation of NPs was achieved using the output of a mode-locked Ti:Sa laser (type *SpectraPhysics Tsunami*) operating with a repetition rate of 80 MHz, exhibiting pulses of 150 fs in duration, and with its spectrum centered at a wavelength of 780 nm. The laser beam was focused on the TiN target using a convex lens of 60 mm focal length to produce sufficient laser fluence for the ablation process. The typical laser beam diameter on the target amounted to 40 μm, corresponding to an average power density of 320 W/cm^2. Figure 1 shows the experimental setup of the PLA system in a schematic representation. In our experiments, we used a commercial bow-tie (PCA 403-10-08-01 from Batop) antenna, with an 85 μm × 256 μm gap, a 6.0 mm × 3.5 mm chip size, and a 4.8-mm antenna length.

The growth of the antenna structure took place in a molecular beam epitaxy (MBE) system at a relatively low temperature (300 °C). The thickness of the LT-GaAs layer grown on top of the semi-insulating (SI) GaAs substrate is 300 nm. The structures were in situ isothermally annealed at 400 °C for 15 min under local As overpressure. A thin film of Au was directly deposited onto the surface of the LT-GaAs to realize emitter electrodes, without using an anti-
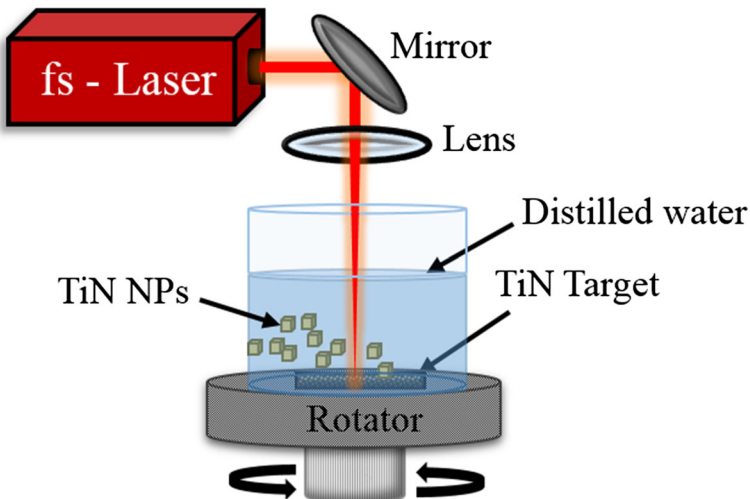

Fig. 1 Schematic diagram of the experimental setup used for the preparation of TiN NPs by laser ablation

reflection coating. The same aforementioned procedures and materials were adopted to fabricate the dipole detector, but with a Ti/Au (10/170 nm, respectively) structure and 5-μm gap between the electrodes.

Here, Au NPs in 0.1 mM of phosphate-buffered saline (PBS) solution purchased from *Sigma-Aldrich* were considered as a reference plasmonic NP dispersion. The absorbance in the region between 400 and 1000 nm of synthesized colloidal TiN and Au NPs were measured using a UV-Vis spectrophotometer (type *Agilent*). The average particle size and zeta potential for the TiN colloidal particles were characterized with a *Malvern* Nanosizer and Zetasizer, respectively. A layer of polydispersed TiN NPs is deposited on the surface of the bow-tie antenna using the drop-casting method. SEM measurements were performed with a *JEOL* SEM system (model *JIB 4601F*).

3 Results and Discussion

The zeta potential (ζ) is an essential parameter that determines the stability of colloidal dispersions. For example, NPs in liquids are considered to be quite stable when $|\zeta| \geq 40$ mV while NPs with $|\zeta| \leq 10$ mV tend to be unstable and likely experience serious agglomeration. Figure 2c shows normalized distributions of the ζ-potential for TiN NPs prepared by both the ULS and the PLA techniques as well as for Au NPs obtained in PBS solution. The corresponding three distributions exhibit peaks at the ζ-potential -1, -21, and -29 mV with a full width at half maximum (FWHM) 8, 21, and 24 mV, respectively. Besides the high correlation between the particle size and zeta potential, Fig. 2 reveals a significant impact of the preparation method on both particle size and distribution.

The negative sign for TiN and Au NPs represents the negative surface charge of these nanoparticles' cores. It is clear that TiN NPs prepared by ULS are almost neutral and tend to be agglomerated or coagulated with time. It seems that TiN NPs prepared by PLA are more stable against agglomeration than those prepared by ULS. Surfactants such as SDS, CTAB, and Tween 80 can be added to increase the stability of these colloids [31, 32]. However, in order to avoid agglomeration effects, we deposited the achieved TiN NPs directly without delay on the surface of LT-GaAs without using any surfactant.

Normalized particle size distributions for TiN and Au NPs calculated from dynamic light scattering (DLS) are shown in Fig. 2a. It is obvious that the ULS and PLA techniques provide two different distributions of the particle size. In general, TiN NPs prepared by PLA under our conditions provided us NPs with lower average size and narrower FWHM of the size distribution. The average particle size, z, for TiN NPs prepared by PLA (ULS) corresponded
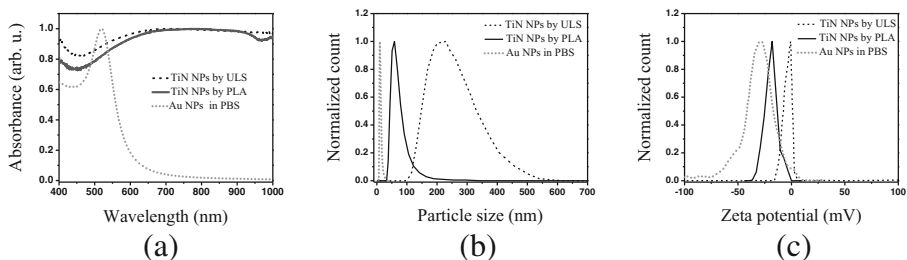

Fig. 2 Difference between the preparation of TiN nanoparticles using ultrasonication (ULS) and pulsed laser ablation (PLA). **a** Spectral dependence of absorbance, **b** particle size, and **c** zeta potential

to 59 nm (224 nm), with the distribution FWHM amounting to 37 nm (179 nm). The peak of the particle size, d, in Fig. 2b is of the same order as the average size, whereas $d = 59$ nm (229 nm). Table 1 summarizes the important parameters extracted from Fig. 2.

To complete the characterization of the considered NPs, absorbance data is shown for TiN and Au NPs in Fig. 1c. Although Au NPs exhibit a strong absorbance peak at 520 nm, this spectral position and width of this peak are incompatible with the operation wavelength of Ti:Sa lasers, the optimum working point of which lies typically at 780–800 nm. This explains why the Au NPs were categorically ruled out as suitable NPs at this stage of our research work. Moreover, another significant reason is given by the fact that colloidal Au islands have shown a negative effect on the terahertz signal when deposited on coplanar transmission lines.

In addition, the data presented in Fig. 2c reveals that the LSPR resonance for our TiN NPs is very broad in comparison to that of Au NPs. More interestingly, TiN NPs feature a high and relatively flat absorbance along the whole spectral range from 600 to 1000 nm. This well qualifies TiN NPs as broadband plasmonic NPs which can be used to enhance the absorption of light in the visible and near-infrared region (NIR). Moreover, unlike Au NPs, TiN NPs with their broadband LSPR resonance are very well suited for TDS systems driven by Ti:Sa lasers. Previous near-field simulations showed that TiN NPs can support high field enhancement and strong absorption in the NIR region. However, it will be discussed later that there are some limitations set for the maximum generalized scattering efficiency [31].

As shown schematically in Fig. 3, we deposited our PLA produced TiN NPs in the gap between the two electrodes of our PCA using a regular micropipette. Here, a bow-tie antenna is used as a source of THz radiation. The measurements of the THz signal were performed using a modified THz TDS setup which is built in a vertical geometry to allow for convenient and flexible antenna exchange. The details of our THz TDS system are presented elsewhere [35].

Figure 4a shows an optical microscope image of the LT-GaAs bow-tie antenna on which a layer of TiN NPs is deposited on its top part. A scanning electron microscope (SEM) image depicting a part of this region can be seen in Fig. 4). In our lab experiments, we observed that TiN NPs tend to be agglomerated at the boundaries of the antenna structure. However, it is clear that the particles are more homogeneously distributed in the area between the two electrodes. The selected area is magnified by a factor of 30,000 using the SEM to get more insight into the particles' sizes, spatial distribution, and surface morphology. The image shows that TiN NPs deposited on the surface of LT-GaAs exhibit different sizes and shapes. However, the average particle size extracted from SEM images is in good agreement with the extracted data from the DLS which is presented in Fig. 2b. Furthermore, the distance between the particles can be also determined from this figure. Exemplarily, a processed image of a small part of the recorded image is shown in Fig. 4c. We used the software Image-J in order to

Table 1 Overview of important parameters of the NPs

Parameter (unit)	TiN NPs by ULS	TiN NPs by PLA	Au NPs in PBS
Peak zeta potential (mV)	−0.8	−21	−29
Average zeta potential (mV)	−2.7	−21	−38
ζ-FWHM (mV)	8	21	24
Peak particle size (nm)	229	59	10
Average particle size (nm)	224	62	11
z-FWHM (nm)	179	37	6
Plasmonic resonance (nm)	625–919	661–913	520

Fig. 3 Schematic representation of the bow-tie PCA with a large area of excitation of the gap between the electrodes, on which TiN nanoparticles are located
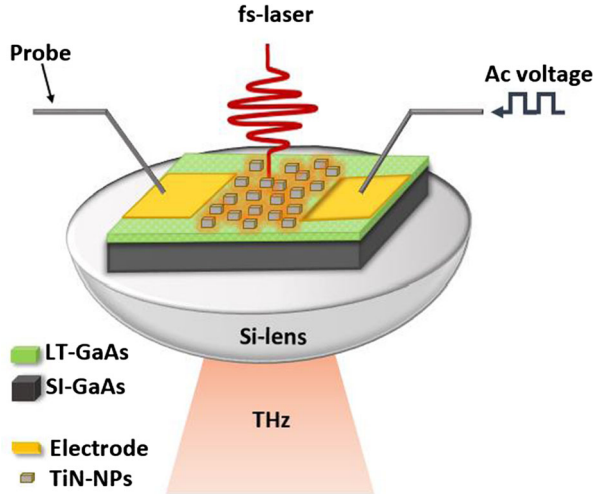
determine the average distance between the particles. The distance between the particles was subdivided into five groups. Each group covers a distance of 100 nm. The resulting histogram
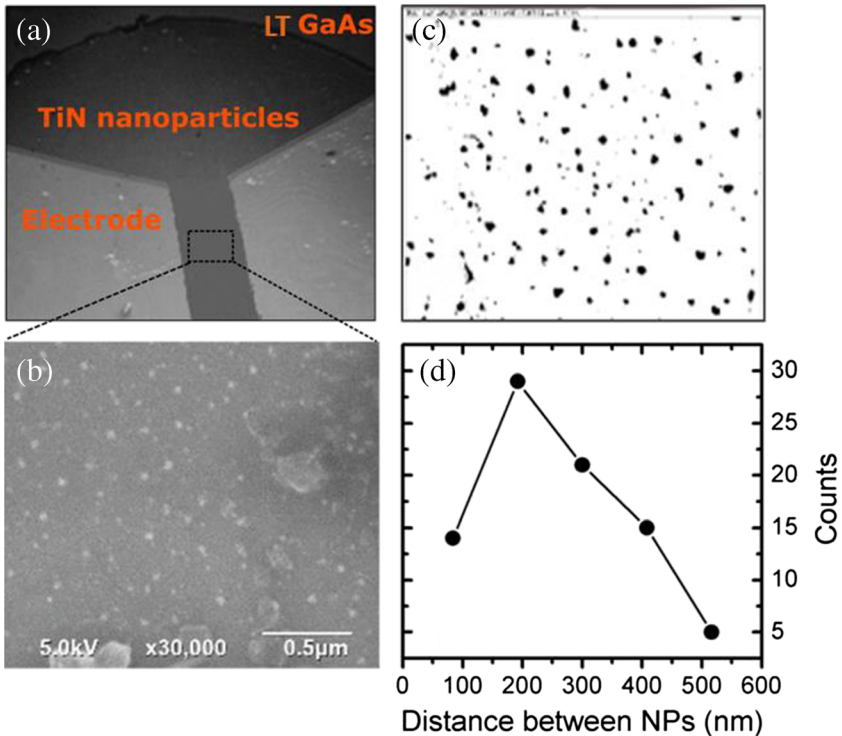

Fig. 4) Optical microscope image of the 85-μm bow-tie antenna on LT-GaAs substrate and **b** scanning electron microscope (SEM) image of the gap region. **c** Processed version of the image section (**b**) using the Image-J software. **d** Histogram (counts) of the distance (in nm) between the deposited TiN nanoparticles obtained from (**c**)
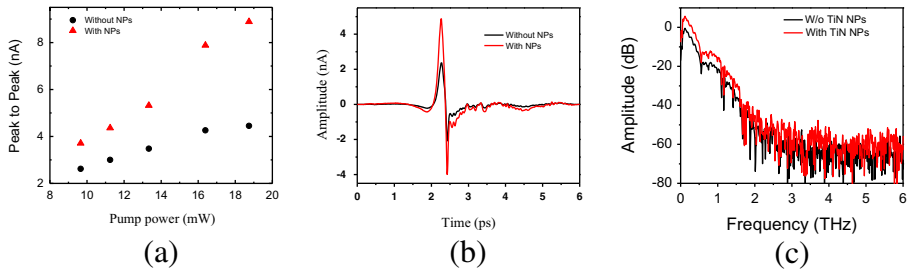
Fig. 5 **a** Peak to peak THz current as a function of fs-pump power with (*red circles*) and without (*black squares*) TiN NPs. **b** Time-domain waveforms and **c** THz power spectra of THz pulses emitted from bow-tie PCA with and without TiN NPs, respectively. As the detector antenna, we used a dipole antenna as described in Ref. [36]

is depicted in Fig. 4d. It can be seen that the distance between the NPs is up to 600 nm, while most particles are separated by approximately 200 nm.

As the next step, we investigated the influence of the NPs on the THz generation. First, we characterized the antenna without any NPs. Afterward, we deposited the NPs on the antenna without changing the alignment. This is possible due to our vertical measurement setup [35]. Figure 5a shows the peak-to-peak (PTP) transient current values for different pump powers with and without TiN NPs. Over the complete range of pump power, the antenna with NPs showed an enhanced THz emission. The TiN NPs prepared by PLA had an average particle size of 67 nm. For a pump power of 20 mW, an enhancement of 100% regarding the PTP field amplitude is obtained (c.f. Fig. 5a). Figure 5b shows an exemplary measured THz trace in the time-domain with (red curve) and without (black curve) NPs. The increased PTP amplitude is clearly visible. The corresponding spectra are depicted in Fig. 5c. It can be seen that the spectral amplitude has a better SNR for frequencies below 1.5 THz. The overall detected bandwidth is unchanged since it is mainly limited by the antenna structure of the dipole detector.

According to the results of near-field simulations [37], a particle size in the range from 60 to 200 nm leads to a maximum scattering efficiency of a laser wavelength around 780 nm. Bigger particles in the range from 120 to 250 nm lead to a high absorption of the NPs. This is an undesirable effect because less of the laser intensity reaches the LT-GaAs layer. Further, the strong absorption can lead to thermal melting of the nanoparticles for high excitation powers.

On the other hand, the previously mentioned theoretical calculations using near-field approximations predict that a higher enhancement should be observed for a larger particle size such as our particles prepared by ULS [31]. However, we did not observe this in our experiment. This may have several reasons. First, these calculations do not consider the distance between the NPs which seems to be important for this type of plasmonic structure. Second, the calculation assumes monodispersed particle size, while we have polydispersed TiN NPs with high FWHM as shown in Fig. 2b. Third, these predictions depend on Mie theory which assumes spherical shapes and this is not compatible with the cubic structure of TiN NPs observed in TEM images [32].

4 Conclusions

We have successfully prepared TiN NPs by both ULS and PLA techniques. The two methods provide NPs with a different distribution of their zeta potential and particle size. Within our

experimental conditions, a lower particle size and greater zeta potential were reached by PLA. In contrast to Au NPs, TiN NPs prepared by us exhibited a high and flat absorbance in the spectral range of 600–1000 nm. An LT-GaAs PCA covered with dispersed TiN NPs showed an enhancement of the THz emission of 100% compared to the antenna without NPs, for a pump power of 20 mW. This was achieved for an average particle size of approximately 60 nm. Our study motivates further investigations on how to develop preparation and deposition techniques in such a way that we obtain full control of the resulting shape, size, and distance between the NPs. We expect that such optimization may lead to further enhancement of the THz signal when using such devices.

References

1. R. Piesiewicz, M. Jacob, M. Koch, J. Schoebel, and T. Kürner, "Performance analysis of future multigigabit wireless communication systems at THz frequencies with highly directive antennas in realistic indoor environments," IEEE J. Sel. Top. Quantum Electron. 14, 421–430 (2008).
2. T. Schneider, "Ultrahigh-Bitrate Wireless Data Communications via THz-Links; Possibilities and Challenges," J. Infrared, Millimeter, Terahertz Waves 36, 159–179 (2015).
3. I. Kallfass, F. Boes, T. Messinger, J. Antes, A. Inam, U. Lewark, A. Tessmann, and R. Henneberger, "64 Gbit/s Transmission over 850 m Fixed Wireless Link at 240 GHz Carrier Frequency," J. Infrared, Millimeter, Terahertz Waves 36, 221–233 (2015).
4. J. L. Johnson, T. D. Dorney, and D. M. Mittleman, "Interferometric imaging with terahertz pulses," IEEE J. Sel. Top. Quantum Electron. 7, 592–599 (2001).
5. C. Jördens and M. Koch, "Detection of foreign bodies in chocolate with pulsed terahertz spectroscopy," Opt. Eng. 47, 37003 (2008).
6. E. Castro-Camus and M. B. Johnston, "Conformational changes of photoactive yellow protein monitored by terahertz spectroscopy," Chem. Phys. Lett. 455, 289–292 (2008).
7. A. J. L. Adam, P. C. M. Planken, S. Meloni, and J. Dik, "TeraHertz imaging of hidden paint layers on canvas," Opt. Express 17, 3407 (2009).
8. R. Gente, S. F. Busch, E.-M. Stubling, L. M. Schneider, C. B. Hirschmann, J. C. Balzer, and M. Koch, "Quality Control of Sugar Beet Seeds With THz Time-Domain Spectroscopy," IEEE Trans. Terahertz Sci. Technol. 6, 1–3 (2016).
9. A. Soltani, S. F. Busch, P. Plew, J. C. Balzer, and M. Koch, "THz ATR Spectroscopy for Inline Monitoring of Highly Absorbing Liquids,". J Infrared, Millimeter, Terahertz Waves 37, 1001–1006 (2016).
10. P. R. Smith, D. H. Auston, and M. C. Nuss, "Subpicosecond photoconducting dipole antennas," IEEE J. Quantum Electron. 24, 255–260 (1988).
11. J. K. Luo, H. Thomas, D. V. Morgan, and D. Westwood, "Transport properties of GaAs layers grown by molecular beam epitaxy at low temperature and the effects of annealing," J. Appl. Phys. 79, 3622 (1996).
12. Y. Cai, I. Brener, J. Lopata, J. Wynn, L. Pfeiffer, J. B. Stark, Q. Wu, X. C. Zhang, and J. F. Federici, "Coherent terahertz radiation detection: Direct comparison between free-space electro-optic sampling and antenna detection," Appl. Phys. Lett. 73, 444–446 (1998).
13. S. Verghese, K. A. McIntosh, and E. R. Brown, "Optical and terahertz power limits in the low-temperature-grown GaAs photomixers," Appl. Phys. Lett. 71, 2743 (1997).
14. G. Segschneider, F. Jacob, T. Löffler, H. G. Roskos, S. Tautz, P. Kiesel, and G. Döhler, "Free-carrier dynamics in low-temperature-grown GaAs at high excitation densities investigated by time-domain terahertz spectroscopy," Phys. Rev. B 65, 125205 (2002).
15. M. Tani, S. Matsuura, K. Sakai, and S. Nakashima, "Emission characteristics of photoconductive antennas based on low-temperature-grown GaAs and semi-insulating GaAs," Appl. Opt. 36, 7853 (1997).
16. N. Vieweg, M. Mikulics, M. Scheller, K. Ezdi, R. Wilk, H. W. Hübers, and M. Koch, "Impact of the contact metallization on the performance of photoconductive THz antennas," Opt. Express 16, 19695 (2008).
17. M. Suzuki and M. Tonouchi, "Fe-implanted InGaAs photoconductive terahertz detectors triggered by 1.56 μm femtosecond optical pulses," Appl. Phys. Lett. 86, 163504 (2005).
18. S. Preu, M. Mittendorff, H. Lu, H. B. Weber, S. Winnerl, and A. C. Gossard, "1550 nm ErAs:In(Al)GaAs large area photoconductive emitters," Appl. Phys. Lett. 101, 101105 (2012).
19. J. Mangeney, "THz photoconductive antennas made from ion-bombarded semiconductors," J. Infrared, Millimeter, Terahertz Waves 33, 455–473 (2012).

20. R. J. B. Dietz, B. Globisch, M. Gerhard, A. Velauthapillai, D. Stanze, H. Roehle, M. Koch, T. Göbel, and M. Schell, "64 µw pulsed terahertz emission from growth optimized InGaAs/InAlAs heterostructures with separated photoconductive and trapping regions," Appl. Phys. Lett. 103, 1–5 (2013).

21. P. U. Jepsen, R. H. Jacobsen, and S. R. Keiding, "Generation and detection of terahertz pulses from biased semiconductor antennas," J. Opt. Soc. Am. B 13, 2424 (1996).

22. E. Castro-Camus, J. Lloyd-Hughes, and M. B. Johnston, "Three-dimensional carrier-dynamics simulation of terahertz emission from photoconductive switches," Phys. Rev. B - Condens. Matter Mater. Phys. 71, 1–7 (2005).

23. K. Ezdi, B. Heinen, C. Jördens, N. Vieweg, N. Krumbholz, R. Wilk, M. Mikulics, and M. Koch, "A hybrid time-domain model for pulsed terahertz dipole antennas," J. Eur. Opt. Soc. 4, (2009).

24. S. Preu, "A Unified Derivation of the Terahertz Spectra Generated by Photoconductors and Diodes," J Infrared, Millimeter, Terahertz Waves 35, 998–1010 (2014).

25. S. Ghorbani, M. Bashirpour, M. Forouzmehr, M. R. Kolahdouz, and M. Neshat, "Simulation of THz photoconductive antennas loaded by different metallic nanoparticles," in *2016 Fourth International Conference on Millimeter-Wave and Terahertz Technologies (MMWaTT)* (IEEE, 2016), pp. 62–64.

26. S. Pillai, K. R. Catchpole, T. Trupke, G. Zhang, J. Zhao, and M. A. Green, "Enhanced emission from Si-based light-emitting diodes using surface plasmons," Appl. Phys. Lett. 88, 161102 (2006).

27. D. Derkacs, S. H. Lim, P. Matheu, W. Mar, and E. T. Yu, "Improved performance of amorphous silicon solar cells via scattering from surface plasmon polaritons in nearby metallic nanoparticles," Appl. Phys. Lett. 89, 93103 (2006).

28. H. A. Atwater and A. Polman, "Plasmonics for improved photovoltaic devices," Nat. Mater. 9, 865–865 (2010).

29. S. Link and M. A. El-Sayed, "Size and Temperature Dependence of the Plasmon Absorption of Colloidal Gold Nanoparticles," J. Phys. Chem. B 103, 4212 (1999).

30. K. S. Lee and M. A. El-Sayed, "Gold and silver nanoparticles in sensing and imaging: Sensitivity of plasmon response to size, shape, and metal composition," J. Phys. Chem. B 110, 19220–19225 (2006).

31. U. Guler, G. V. Naik, A. Boltasseva, V. M. Shalaev, and A. V. Kildishev, "Performance analysis of nitride alternative plasmonic materials for localized surface plasmon applications," Appl. Phys. B Lasers Opt. 107, 285–291 (2012).

32. U. Guler, S. Suslov, A. V. Kildishev, A. Boltasseva, and V. M. Shalaev, "Colloidal Plasmonic Titanium Nitride Nanoparticles: Properties and Applications," Nanophotonics 4, 269–276 (2015).

33. A. Jooshesh, V. Bahrami-Yekta, J. Zhang, T. Tiedje, T. E. Darcie, and R. Gordon, "Plasmon-Enhanced below Bandgap Photoconductive Terahertz Generation and Detection," Nano Lett. 15, 8306–8310 (2015).

34. W. Lai, O. Mazin Abdulmunem, P. del Pino, B. Pelaz, W. J. Parak, Q. Zhang, and H. Zhang, "Enhanced Terahertz Radiation Generation of Photoconductive Antennas Based on Manganese Ferrite Nanoparticles," Sci. Rep. 7, 46261 (2017).

35. O. M. Abdulmunem, N. Born, M. Mikulics, J. C. Balzer, M. Koch, and S. Preu, "High accuracy terahertz time-domain system for reliable characterization of photoconducting antennas," Microw. Opt. Technol. Lett. 59, 468–472 (2017).

36. O. M. Abdulmunem, K. I. Hassoon, J. Völkner, M. Mikulics, K. I. Gries, and J. C. Balzer, "Photoconductive LT-GaAs Terahertz Antennas: Correlation Between Surface Quality and Emission Strength," J. Infrared, Millimeter, Terahertz Waves (2017).

37. U. Guler, V. M. Shalaev, and A. Boltasseva, "Nanoparticle plasmonics: Going practical with transition metal nitrides," Mater. Today 18, 227–237 (2015).

3.6 Enhanced Terahertz Radiation Generation of Photoconductive Antennas Based on Manganese Ferrite Nanoparticles

Weien Lai, Oday Mazin Abdulmunem, Pablo del Pino, Beatriz Pelaz, Wolfgang J. Parak,Qian Zhang and Huaiwu Zhang, Scientific Report, 7:46261, DOI: 10.1038/srep46261 (2017).

3.6.1 Abstract:

This paper presents a significant effect of Manganese Ferrite nanoparticles ($MnFe_2O_4$) NPs on the increase of the surface photoconductivity of semiconductors. Herein, the optical characterization of photo-excited carriers of silicon coated with $MnFe_2O_4$ NPs was studied by using THz time-domain spectroscopy (THz-TDs). We observed that silicon coated with $MnFe_2O_4$ NPs provided a significantly enhanced attenuation of THz radiation in comparison with bare silicon substrates under laser irradiation. However, the experimental results were assessed in the context of a surface band structure model of semiconductors. In addition, photoconductive antennas coated with $MnFe_2O_4$ NPs significantly improved the efficiency of THz radiation generation and signal to noise ratio of the THz signal. This work demonstrates that coating with $MnFe_2O_4$ NPs could improve the overall performance of THz systems, and $MnFe_2O_4$ NPs could be further used for the implementation of novel optical devices.

3.6.2 The author's contribution:

All experiments were performed by Weien Lai and me. Weien Lai and Qian Zhang designed the research work, and the nanoparticles were prepared by Qian Zhang. The manuscript was written by Weien Lai, Pablo del Pino,Qian Zhang and me. Wolfgang Parak, Pablo del Pino, Beatriz Pelaz, and Huaiwu Zhang revised the manuscript. All the authors contributed to the mechanism analysis and reviewed the manuscript.

SCIENTIFIC REPORTS

OPEN

Enhanced Terahertz Radiation Generation of Photoconductive Antennas Based on Manganese Ferrite Nanoparticles

Weien Lai[1,2], Oday Mazin Abdulmunem[2], Pablo del Pino[3], Beatriz Pelaz[3], Wolfgang J. Parak[2,4], Qian Zhang[2,4] & Huaiwu Zhang[5]

This paper presents a significant effect of manganese ferrite nanoparticles ($MnFe_2O_4$ NPs) on the increase of the surface photoconductivity of semiconductors. Herein, the optical characterization of photo-excited carriers of silicon coated with $MnFe_2O_4$ NPs was studied by using THz time-domain spectroscopy (THz-TDs). We observed that silicon coated with $MnFe_2O_4$ NPs provided a significantly enhanced attenuation of THz radiation in comparison with bare silicon substrates under laser irradiation. The experimental results were assessed in the context of a surface band structure model of semiconductors. In addition, photoconductive antennas coated with $MnFe_2O_4$ NPs significantly improved the efficiency of THz radiation generation and signal to noise ratio of the THz signal. This work demonstrates that coating with $MnFe_2O_4$ NPs could improve the overall performance of THz systems, and $MnFe_2O_4$ NPs could be further used for the implementation of novel optical devices.

Since nanoscale materials started to routinely appear in the literature almost two decades ago[1], nanotechnology based on nanoparticles (NPs) has attracted interest by many researchers from very diverse areas, such as biology, physics, chemistry, engineering, materials science, and medicine. Recent developments based on nanomaterials have found a variety of uses in industry and life science, such as waste treatment, solar cells[2], optoelectronics, light generation[3], biomedicine[4,5], *in-vitro* diagnostic reagents[6], and biological labeling[7], amongst others. These multifaceted applications mainly originate from specific size-related physicochemical properties present in many nanomaterials. When the size of bulk materials is reduced down to the nanoscale, the relative number of surface atoms to the total number of atoms in the material drastically increases[8]. Compared to bulk materials with ordered crystalline structure, the surface atoms of nanomaterials present weak and unsaturated bonding states, which drastically influence their surface properties. For instance, surface atoms of NPs present in general high chemical reactivity for catalytic processes. Besides the high surface-to-volume ratio which is present in all NPs, some NP materials also possess particular size-related properties when scaled down to the nanoscale. This is for example true for the case of localized surface plasmons (*e.g.*, plasmonic NPs[9]), fluorescence (*e.g.*, quantum dots, QDs[10]), superparamagnetism (*e.g.*, magnetic NPs[11]), photocatalysis (*e.g.*, titanium dioxide NPs[12]), *etc.*

Recently, nanotechnology has extended into the field of terahertz (THz) technology. THz technology has become increasingly attractive because of its potential applications[13–16]. For the application of THz technology, a THz system requires two main components: an emitter and a detector[16–19]. THz emitters can be produced by various techniques, such as photoconductive (PC) antennas[17,18,20], superconductor[21] and nonlinear crystals[22]. However, in comparison with other techniques[21–24], PC antennas are key players due to their high efficiency. In

[1]Academy of Photoelectric Technology, HeFei University of Technology, HeFei, 230009, China. [2]Faculty of Physics, Philipps-Universität Marburg, Renthof 7, Marburg, 35032, Germany. [3]Centro Singular de Investigación en Química Biológica e Materiales Moleculares (CiQUS), and Departamento de Física de Partículas, Universidade de Santiago de Compostela, Santiago de Compostela, 15782, Spain. [4]Institute of Nano Biomedicine and Engineering, Key Laboratory for Thin Film and Microfabrication Technology of the Ministry of Education, Department of Instrument Science and Engineering, School of Electronic Information and Electrical Engineering, Shanghai Jiao Tong University, 800 Dongchuan RD, Shanghai, 200240, China. [5]State Key Laboratory of Electronic Films and Integrated Devices, University of Electronic Science and Technology of China, Chengdu, 610054, China. Correspondence and requests for materials should be addressed to Q.Z. (email: qianzhang0130@sjtu.edu.cn)
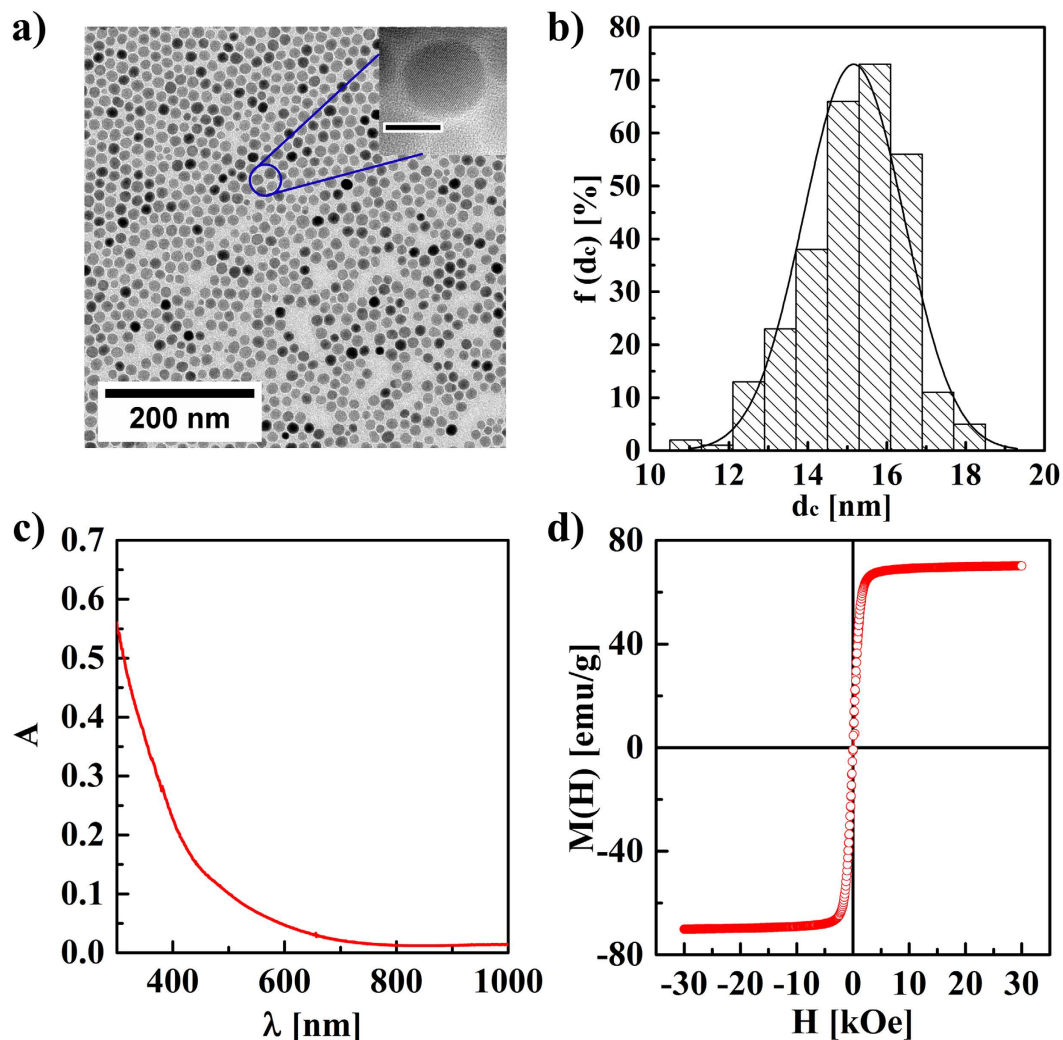
Figure 1. (**a**) TEM bright field image of $MnFe_2O_4$ NPs (scale bar: 200 nm). The insert shows a HRTEM image of one individual NP (scale bar: 15 nm). (**b**) The corresponding histogram for the distribution frequency of the core diameter $f(d_c)$, as produced by analysis of the TEM image with the free software ImageJ is based on analyzing >300 NPs. The mean diameter of the inorganic cores was determined to be $d_c = 15.06 \pm 1.2$ nm. (**c**) UV-Vis absorption spectra $A(\lambda)$ of $MnFe_2O_4$ NPs in chloroform. (**d**) Magnetization versus magnetic field M(H) curve of $MnFe_2O_4$ NPs, measured at 300 K using a SQUID magnetometer. The saturation magnetization was found to be about $M_s = 72$ emu/g.

general, PC antennas are fabricated on semiconductor substrates, such as low-temperature-grown GaAs[19,25]. In order to improve their performance, a significant body of work has been focused on optimizing the structures and substrates for PC antennas[26–28]. However, most of these PC antennas have complex structures, which rely on sophisticated fabrication techniques. Therefore, one key scientific challenge is to improve the performance of PC antennas by cost-effective simple methods[26,29–32]. In this work, the effect of coating a silicon substrate with $MnFe_2O_4$ NPs on its PC properties was investigated. Based on this an approach to improve the performance of PC antennas by utilizing a coating based on $MnFe_2O_4$ NPs is presented. $MnFe_2O_4$ NPs are low-cost materials, present high-stability and environmental compatibility, which makes this type of coatings a potential candidate for industrial applications.

Results and Discussion

Synthesis and characterization of manganese ferrite nanoparticles (MnFe₂O₄ NPs).

Monodisperse $MnFe_2O_4$ NPs were synthesized *via* thermal decomposition as described in the Methods Section, based on a previously published protocol[11]. The resulting $MnFe_2O_4$ NPs were well dispersed in organic solvents, having long-time colloidal stability. The elemental components in the $MnFe_2O_4$ NPs were determined by inductively coupled plasma mass spectrometry (ICP-MS), confirming that the Mn:Fe ratio was approximately 1:2 (*cf.* Table S1 in the Supporting Information). The transmission electron microscopy (TEM) and high-resolution TEM images (HRTEM) in Fig. 1a demonstrate that the $MnFe_2O_4$ NPs present an uniform size and spherical structure. The size distribution of the NPs was analyzed by using the software ImageJ, yielding a diameter of inorganic core
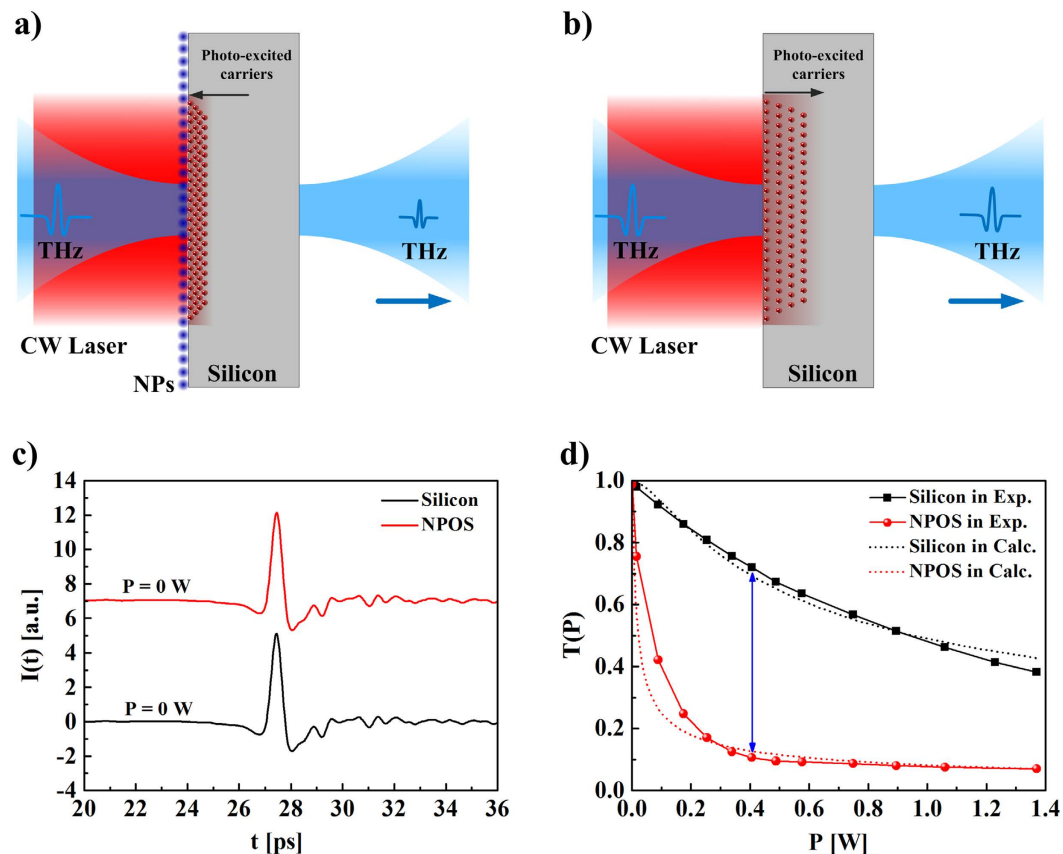
Figure 2. Schematic representation of a THz pulse transmitted through a NPOS substrate (**a**) and a bare silicon substrate (**b**) under CW laser irradiation. (**c**) Waveforms of THz pulses I(t) transmitted through silicon and NPOS substrates. (**d**) Amplitude transmissions T(P) of the THz pulses transmitted through the silicon and NPOS substrates under laser irradiation with different lased powers P. The dotted lines represent fits to the experimental data.

(d_c) of 15 nm with variation $\sigma < 5\%$ (Fig. 1b). The hydrodynamic diameter of the $MnFe_2O_4$ NPs dispersed in chloroform was measured by dynamic light scattering (DLS), indicating a narrow size distribution (*cf.* Figure S1 in the Supporting Information). The absorption spectrum of the $MnFe_2O_4$ NPs was measured by UV-Vis absorption spectrophotometry (Fig. 1c). The spectra indicate that the NPs have no specific absorption in the NIR spectral region. The magnetic properties of the $MnFe_2O_4$ NPs were measured by a superconducting quantum interference device (SQUID), and the resulting magnetization *versus* magnetic field curve M(H) is shown in Fig. 1d. This curve exhibits a smooth loop without hysteresis loss, with a saturated magnetization value (M_s) of 72 emu/g. Thus, the $MnFe_2O_4$ NPs exhibit excellent superparamagnetic behavior.

Optical characterization of MnFe₂O₄ NPs on silicon (NPOS) under laser irradiation. NPOS substrates were fabricated by spin-coating of the $MnFe_2O_4$ NPs on high resistivity silicon as substrate (details are described in Methods Section, SEM images are shown in Figure S2). A bare silicon substrate without NPs was used as control. To study the optical properties of NPOS substrate under laser irradiation (continuous wave (CW) excitation at 808 nm), THz time-domain spectroscopy (THz-TDS) in transmission mode was simultaneously performed, as shown in Fig. 2. The spot diameter of the CW laser was about 4 mm, fully overlapping with the THz beam on the surface of the samples. The THz beam was directed to the sample at normal incidence by a focusing lens, as shown in Fig. 2. The frequency bandwidth in the THz system was limited to 2.5 THz, since outside this frequency range the signal was too weak to obtain an acceptable signal-to-noise ratio. The optical properties of the NPOS substrate were investigated by changing the irradiation power of the CW laser. In addition, in order to understand the THz response of NPs under laser irradiation, a bare quartz substrate and a NPs-coated quartz substrate were used as control group.

For THz transmission measurements under laser irradiation, the THz signals transmitted through the samples consisted of pulsed waveforms. The waveforms of THz pulses transmitted through the silicon and NPOS substrates under the laser irradiation with different powers are shown in Figure S9 (*cf.* Figure S9 in the Supporting Information). The amplitudes of the THz pulses transmitted through the NPOS substrates, as well as the amplitudes of the THz pulses transmitted through bare silicon substrates, decreased as expected upon increasing the power of the laser irradiation. Furthermore, under no laser irradiation, the waveform of THz pulse transmitted through the NPOS substrate was almost identical to the one of the bare silicon substrate, as shown in
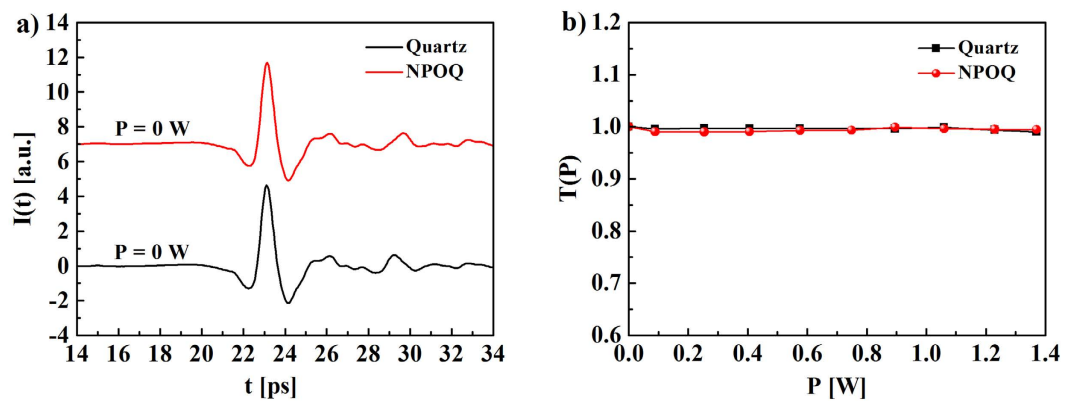
Figure 3. (**a**) Waveforms of THz pulses transmitted through quartz and MnFe$_2$O$_4$ NPs on quartz (NPOQ) substrates. (**b**) Amplitude of the transmissions of the THz pulses transmitted through quartz and NPOQ substrates under laser irradiation with different laser powers, demonstrating that the NPs do not absorb THz excitation.

Fig. 2. This demonstrates that the absorption of MnFe$_2$O$_4$ NPs in the THz frequency range is negligible. Moreover, under no laser irradiation (P = 0), the waveform of THz pulses transmitted through NPOQ substrates was almost identical to the one through bare quartz substrates, as shown in Fig. 3a. The coefficients of the transmissions of THz pulses transmitted through NPOQ substrates, as well as the one transmitted through bare quartz substrates, was almost identical and constant ($T \approx 1$) upon increasing the power of the laser irradiation, as shown in Fig. 3b. This demonstrates that the absorption of MnFe$_2$O$_4$ NPs at 808 nm wavelength of CW laser excitation is negligible.

To account for the differences of THz transmissions between NPOS and bare silicon substrates under laser irradiation, we further compared the amplitudes of the THz pulses transmitted through NPOS substrates with the ones transmitted through bare silicon substrates. The amplitudes of both pulses were normalized with respect to the amplitude of the THz pulse transmitted through bare silicon under no laser irradiation. We found that in both cases, the amplitudes of the transmissions slowly decreased by increasing the power of the laser irradiation, as shown in Fig. 2d. The transmission-dropping in the case of the NPOS substrate was significantly higher than in the bare silicon substrate. When the power of laser irradiation was about $P \approx 0.41$ W, the transmission change ($|\Delta T_{NPOS}/T^0_{Si}| \cdot 100\% \approx 90\%$) in NPOS substrate was significantly higher than the transmission change ($|\Delta T_{Si}/T^0_{Si}| \cdot 100\% \approx 28\%$) of the bare silicon substrate, as shown in Fig. 2d. On the other hand, the amplitude transmissions through NPOS were in a good agreement with that predicted by simulations obtained by a theoretical model based on band theory, which is described in the Supporting Information. The proposed modeling and the experiments on bare silicon substrates yielded similar results, except for low irradiation powers (P < 0.2 W). We speculate that this discrepancy may arise from partial beam blocking by the NPOS substrates, resulting in a less efficient production of photo-excited carriers. Yet for laser irradiation above P = 0.2 W, the effect of the aforementioned phenomenon is negligible. Since the amplitude of the THz pulse transmitted through a sample is inherently correlated with the conductivity of the conducting layer of the sample, for the same irradiation power, the conductivity in a NPOS substrate is significantly higher than in a bare silicon substrate. This explains the higher density of photo-excited carriers in NPOS as compared to bare silicon substrates. In parallel, we also investigated THz transmission amplitudes through different NPOS substrates based on a series of different NPs under laser irradiation with different powers P (*cf.* Figures S3, S4 and S5 in the Supporting Information), and we compared different magnetic NPs with similar size to exclude the effect of magnetic response of NPs on the photoconductivity of the semiconductors (*cf.* Figures S7 and S8 in the Supporting Information). We found that all NP-coated silicon substrates slightly decreased the transmissions as compared to bare silicon substrates with increasing the laser power. However, the NPOS substrates based on MnFe$_2$O$_4$ NPs exhibited the biggest effect of all tested NPs, which could be explained by the properties of materials tested here in the Supporting Information. Hence, our experiments demonstrate that coating with MnFe$_2$O$_4$ NPs significantly provides an enhanced attenuation of THz radiation in comparison with bare silicon substrates under laser irradiation.

Performance of MnFe$_2$O$_4$ NP coated PC antennas. PC antennas were used to verify the potential application of MnFe$_2$O$_4$ NPs in the THz region. The PC antenna used herein consisted of a simple stripline structure of metal film and a low-temperature-grown GaAs substrate. A schematic of the PC antenna used herein is shown in Fig. 4. A femtosecond (fs) pulsed laser (central wavelength of 780 nm, 155 fs pulse duration) was used to pump the PC antenna to generate THz radiation. The PC antenna was biased with an AC voltage of frequency. First, the fs laser was focused on the uncoated PC antenna to generate THz radiation as reference signal. Equivalently, the NPs-coated antenna was used to generate THz radiation as sample signal. These measurements were performed 6 times, to ensure the reproducibility of the experimental results.

From this experiment, it is observable that, under equal pumping conditions, the amplitude of the THz signal from the NP-coated PC antenna (sample signal) was significantly higher than that of the reference signal (uncoated antenna), as illustrated in Fig. 4c. Likewise, in the time-frequency transformation, the signal-to-noise ratio of the NP-coated antenna was improved as compared to the uncoated antenna, as shown in Fig. 4d. The
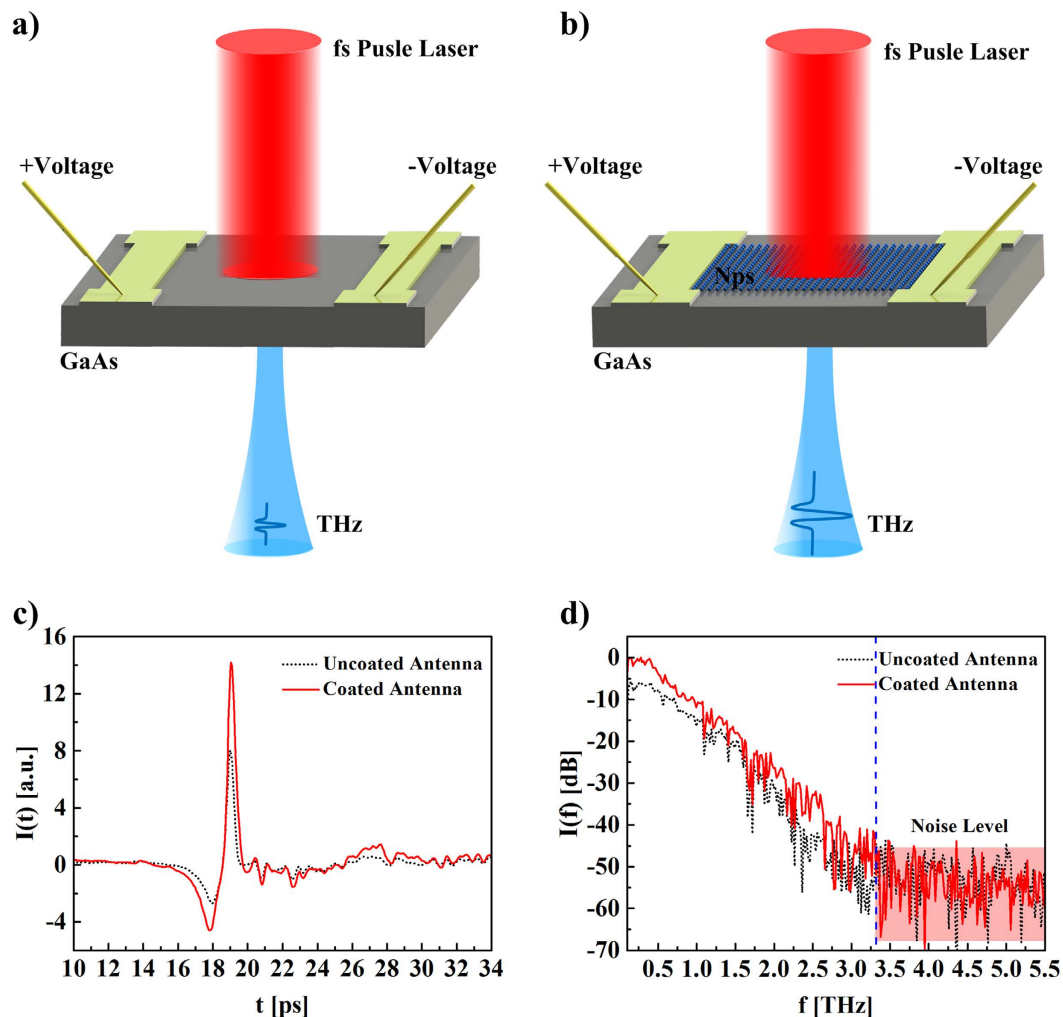
Figure 4. Experimental schematic of THz pulses generated from (**a**) an uncoated PC antenna and (**b**) from a PC antenna coated with $MnFe_2O_4$ NPs under fs laser pumping. (**c**) Waveforms of THz pulses generated from the uncoated PC antenna and the PC antenna coated with $MnFe_2O_4$ NPs. (**d**) The emission spectra of THz pulses generated from the uncoated PC antenna and the PC antenna coated with $MnFe_2O_4$ NPs.

electric field $\vec{E}_{THz}$ of THz radiation as generated from a PC antenna[14,25,29] is expressed as $\vec{E}_{THz}(t,\vec{r}) = \frac{1}{4\pi\varepsilon_0 c^3 r^3} \cdot \vec{r} \times \left(\vec{r} \times \frac{d\vec{j}(t)}{dt} \right)$. Here, $\vec{r}$ is the vector in the direction of the observation and $\vec{j}(t)$ is the time-dependent photocurrent density. According to this equation, the correlation between the electric field of THz radiation and the photocurrent density can be described by $\vec{E}_{THz}(t) \propto \frac{d\vec{j}(t)}{dt}$[14]. Therefore, the electric field of THz radiation is enhanced by increasing the photocurrent density in the PC antenna. The coating of $MnFe_2O_4$ NPs on the PC antenna can increase the carrier density, so that the photocurrent density also increases in the PC antenna. The experimental results of the here used PC antennas demonstrate that addition of $MnFe_2O_4$ NPs can increase the THz radiation generation efficiency of PC antennas. In addition, the $MnFe_2O_4$ NPs improve the signal-to-noise ratio of the THz signal generated from the PC antenna, which plays an important role in the performance of THz systems. Therefore, the usage of $MnFe_2O_4$ NPOS substrates can improve the performance of THz systems.

Conclusion

In conclusion, we demonstrated that coating with $MnFe_2O_4$ NPs can be used to improve the performance of PC antennas in the THz region. Our experiments demonstrate that coatings with $MnFe_2O_4$ NPs provided a new approach to increase the photocurrent density on silicon under CW illumination. In order to understand the effect of $MnFe_2O_4$ NPs on photo-excited silicon, a semiconductor model was proposed to describe this phenomenon. We used this model to calculate the transmission amplitudes of THz pulses transmitted through NPOS and bare silicon substrates under laser irradiation with different powers. Because the effect of $MnFe_2O_4$ NPs on silicon significantly provides an enhanced attenuation of terahertz wave, NPOS has the potential to be used as an optical modulator in the THz region. This may lead to a cost-efficient component for THz-TDS systems operating

in transmission mode. Hence, $MnFe_2O_4$ NPs have the potential application to increase the overall performance of THz-TDS systems. Furthermore, $MnFe_2O_4$ NPs could be used for the implementation of novel optical devices.

Methods

Synthesis of monodisperse $MnFe_2O_4$ NPs. The synthesis method for monodisperse $MnFe_2O_4$ NPs (core diameter ~15 nm) is based on the previously published protocols from Sun and Zhang[11,33]. In order to acquire the desired size, the synthesis was separated into a seed synthesis process and a seed-mediated growth process.

Briefly, iron(III) acetylacetonate (Fe(acac)$_3$, 2 mmol), manganese(II) acetylacetonate (Mn(acac)$_2$, 1 mmol) and 1,2-hexadecanediol (10 mmol) were placed in a 100 mL three-neck flask in the presence of oleic acid (OLA, 6 mmol), oleylamine (OLAM, 6 mmol), and 10 mL of benzyl ether. Under magnetic stirring, the mixture was firstly degassed at 100 °C with vacuum for 30 min. Under the protection of nitrogen flow, the mixture was slowly heated up to 200 °C and aged for 2 h, and then heated again to 300 °C with keeping this temperature for 1 h. The reaction was stopped by removing the heating mantle, followed by the addition of ethanol (~40 mL) to precipitate black-colored seeds with centrifugation (3000 rpm, 10 min). After removing the supernatant, the precipitate was dissolved in hexane in the presence of 10 μL mixture of OLA and OLAM, which served for stabilizing the NPs. Centrifugation (3000 rpm, 10 min) was applied again in order to remove aggregates. The product, *i.e.* the supernatant with $MnFe_2O_4$ NPs of around 10 nm core diameter, was harvested by centrifugation (3000 rpm, 10 min) under the addition of sufficient ethanol. The NP precipitate was then redispersed in chloroform at a concentration of 20 mg/mL.

In order to produce $MnFe_2O_4$ NPs of 15 nm core diameter, a seed-mediated growth process was used by growing a shell on the previously described 10 nm diameter $MnFe_2O_4$ NPs seeds. Specifically, 2 mmol of Fe(acac)$_3$, 1 mmol of Mn(acac)$_2$, 10 mmol of 1,2-hexadecanediol were mixed with 50 mg $MnFe_2O_4$ seeds (dissolved in 2.5 mL CHCl$_3$), 2 mmol of OLA, 2 mmol of OLAM and 20 mL of benzyl ether. The mixture was magnetically stirred at 100 °C for 20 min under vacuum to remove CHCl$_3$. Under the protection of nitrogen flow, the temperature was raised slowly to 200 °C, and the solution was left for 1 h at this temperature. Then the temperature was again increased with the same heating speed up to reflux (~300 °C) for 30 min. The black-colored mixture was cooled down to room temperature (R.T.) by removing the heating mantle. The NPs were washed by repeated precipitation and redissolution as described above. Finally, the resulting 15 nm diameter $MnFe_2O_4$ NPs were dissolved in 20 mL of CHCl$_3$.

Fabrication of manganese ferrite nanoparticles on a silicon (NPOS). The monodisperse manganese ferrite NPs were immobilized on a silicon substrate to fabricate a NPOS system *via* a spin coating process[34]. Typically, a silicon substrate (resistivity >2000 Ω·cm, cut from a 0.5-mm thick wafer), was firstly cleaned 3 times with acetone solution. Then 50 μL of manganese ferrite NPs (dispersed in chloroform at a NP concentration of 2 mg/mL) was casted on the surface of the silicon substrate with a rotating speed of 100 rpm for 10 s.

References

1. Chatelain, A., Bonard, J. M., Buttet, J. & Monot, R. Small particles and inorganic clusters. Preface. *Eur Phys J D* **9,** U1–U1 (1999).
2. Lee, J., Mahendra, S. & Alvarez, P. J. J. Nanomaterials in the Construction Industry: A Review of Their Applications and Environmental Health and Safety Considerations. *Acs Nano* **4,** 3580–3590 (2010).
3. Rizzo, A. *et al.* Blue light emitting diodes based on fluorescent CdSe/ZnS nanocrystals. *Appl Phys Lett* **90,** 051106 (2007).
4. Daniel, M. C. & Astruc, D. Gold nanoparticles: Assembly, supramolecular chemistry, quantum-size-related properties, and applications toward biology, catalysis, and nanotechnology. *Chem Rev* **104,** 293–346 (2004).
5. Ashraf, S. *et al.* Gold-Based Nanomaterials for Applications in Nanomedicine. *Top Curr Chem* **370,** 169–202 (2016).
6. Azzazy, H. M. E. & Mansour, M. M. H. *In vitro* diagnostic prospects of nanoparticles. *Clin Chim Acta* **403,** 1–8 (2009).
7. Zhang, C. L. *et al.* Gold Nanoclusters-Based Nanoprobes for Simultaneous Fluorescence Imaging and Targeted Photodynamic Therapy with Superior Penetration and Retention Behavior in Tumors. *Advanced Functional Materials* **25,** 1314–1325 (2015).
8. Goesmann, H. & Feldmann, C. Nanoparticulate Functional Materials. *Angewandte Chemie, International Edition* **49,** 1362–1395 (2010).
9. Petryayeva, E. & Krull, U. J. Localized surface plasmon resonance: Nanostructures, bioassays and biosensing-A review. *Anal Chim Acta* **706,** 8–24 (2011).
10. Khalid, W. *et al.* Immobilization of Quantum Dots via Conjugated Self-Assembled Monolayers and Their Application as a Light-Controlled Sensor for the Detection of Hydrogen Peroxide. *ACS Nano* **5,** 9870–9876 (2011).
11. Zhang, Q. *et al.* Model Driven Optimization of Magnetic Anisotropy of Exchange-Coupled Core-Shell Ferrite Nanoparticles for Maximal Hysteretic Loss. *Chem Mater* **27,** 7380–7387 (2015).
12. Pelaez, M. *et al.* A review on the visible light active titanium dioxide photocatalysts for environmental applications. *Appl Catal B-Environ* **125,** 331–349 (2012).
13. Horiuchi, N. View From … Teranano 2011 Terahertz Nano-Exploration. *Nat Photonics* **6,** 82–83 (2012).
14. Jepsen, P. U., Cooke, D. G. & Koch, M. Terahertz spectroscopy and imaging - Modern techniques and applications. *Laser Photonics Rev* **5,** 124–166 (2011).
15. Ferguson, B. & Zhang, X. C. Materials for terahertz science and technology. *Nature Materials* **1,** 26–33 (2002).
16. Lai, W. E., Zhang, H. W., Zhu, Y. H. & Wen, Q. Y. A Novel Method of Terahertz Spectroscopy and Imaging in Reflection Geometry. *Appl Spectrosc* **67,** 36–39 (2013).
17. Cai, Y. *et al.* Design and performance of singular electric field terahertz photoconducting antennas. *Appl Phys Lett* **71,** 2076–2078 (1997).
18. Jepsen, P. U., Jacobsen, R. H. & Keiding, S. R. Generation and detection of terahertz pulses from biased semiconductor antennas. *Journal of the Optical Society of America B* **13,** 2424–2436 (1996).
19. Zhang, J., Hong, Y., Braunstein, S. L. & Shore, K. A. Terahertz pulse generation and detection with LT-GaAs photoconductive antenna. *IEE Proceedings - Optoelectronics* **151,** 98–101 (2004).
20. Castro-Camus, E., Lloyd-Hughes, J. & Johnston, M. B. Three-dimensional carrier-dynamics simulation of terahertz emission from photoconductive switches. *Phys Rev B* **71** (2005).
21. Kashiwagi, T. *et al.* Generation of electromagnetic waves from 0.3 to 1.6 terahertz with a high-Tc superconducting $Bi_2Sr_2CaCu_2O_8+δ$ intrinsic Josephson junction emitter. *Appl Phys Lett* **106,** 2394 (2015).
22. Carey, J. J. *et al.* Terahertz pulse generation in an organic crystal by optical rectification and resonant excitation of molecular charge transfer. *Appl Phys Lett* **81,** 4335–4337 (2002).

23. Zhong, H., Karpowicz, N. & Zhang, X. C. Terahertz emission profile from laser-induced air plasma. *Appl Phys Lett* **88** (2006).
24. Kadowaki, K. *et al.* Quantum terahertz electronics (QTE) using coherent radiation from high temperature superconducting $Bi_2Sr_2CaCu_2O_8$+ delta intrinsic Josephson junctions. *Physica C* **491,** 2–6 (2013).
25. Awad, M., Nagel, M., Kurz, H., Herfort, J. & Ploog, K. Characterization of low temperature GaAs antenna array terahertz emitters. *Appl Phys Lett* **91** (2007).
26. Han, S. P. *et al.* Compact fiber-pigtailed InGaAs photoconductive antenna module for terahertz-wave generation and detection. *Opt Express* **20,** 18432–18439 (2012).
27. Mittendorff, M. *et al.* Large area photoconductive terahertz emitter for 1.55 mu m excitation based on an InGaAs heterostructure. *Nanotechnology* **24** (2013).
28. Tanoto, H. *et al.* Nano-antenna in a photoconductive photomixer for highly efficient continuous wave terahertz emission. *Scientific Reports* **3** (2013).
29. Gao, Y. H. *et al.* Analysis of terahertz generation via nanostructure enhanced plasmonic excitations. *Journal of Applied Physics* **106** (2009).
30. Tong, J. Y., Muthee, M., Chen, S. Y., Yngvesson, S. K. & Yan, J. Antenna Enhanced Graphene THz Emitter and Detector. *Nano Letters* **15,** 5295–5301 (2015).
31. Young, C. D. Exploring terahertz pulse enhancement through gold nanoparticle deposition. *Dissertations & Theses - Gradworks* (2009).
32. Park, S. G., Choi, Y., Oh, Y. J. & Jeong, K. H. Terahertz photoconductive antenna with metal nanoislands. *Opt Express* **20,** 25530–25535 (2012).
33. Sun, S. *et al.* Monodisperse MFe_2O_4 (M = Fe, Co, Mn) Nanoparticles. *J. Am. Chem. Soc.* **126,** 273–279 (2004).
34. Sabir, N. *et al.* Photo-electrochemical Bioanalysis of Guanosine Monophosphate Using Coupled Enzymatic Reactions at a CdS/ZnS Quantum Dot Electrode. *Small* **11,** 5844–5850 (2015).

Acknowledgements

Author Contributions

W.L. and Q.Z. designed the research work, Q.Z. applied for all types of NPs, W.L. and O.A. performed the experiments and characterizations. W.P., P.P., B.P. and H.Z. revised the manuscript. All the authors contributed to the mechanism analysis and reviewed the manuscript.

Additional Information

Supplementary information accompanies this paper at http://www.nature.com/srep

Competing Interests: The authors declare no competing financial interests.

How to cite this article: Lai, W. *et al.* Enhanced Terahertz Radiation Generation of Photoconductive Antennas Based on Manganese Ferrite Nanoparticles. *Sci. Rep.* **7**, 46261; doi: 10.1038/srep46261 (2017).

Publisher's note: Springer Nature remains neutral with regard to jurisdictional claims in published maps and institutional affiliations.

Supporting Information

Enhanced Terahertz Radiation Generation of Photoconductive Antennas Based on Manganese Ferrite Nanoparticles

Weien Lai, Oday Mazin Abdulmunem, Pablo del Pino, Beatriz Pelaz, Wolfgang J. Parak, Qian Zhang and Huaiwu Zhang

1. Dynamic Light Scattering (DLS) measurements

The average size distribution of $MnFe_2O_4$ NPs in chloroform was determined by DLS (shown in Figure S1). The measurements were repeated three times. The mean diameter d_h in chloroform as derived from the number distribution was determined to be 14.8 nm. This demonstrates that the NPs were well dispersed in organic solvent without aggregation.
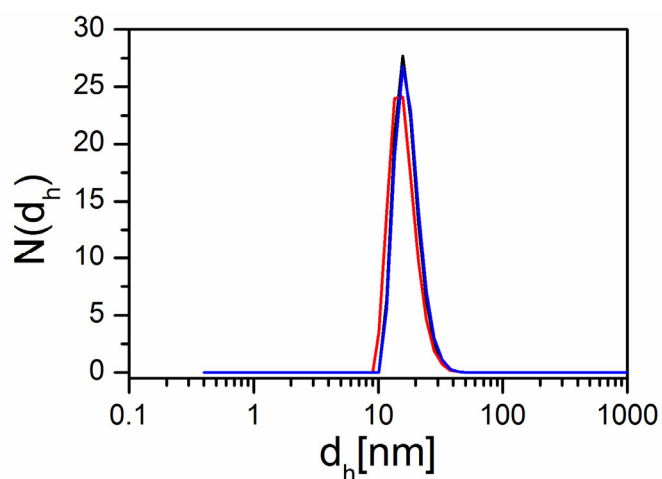

Figure S1. Number distribution $N(d_h)$ of the solution-based diameter of $MnFe_2O_4$ NPs dispersed in chloroform. The mean diameter is about 14.8 nm.

2. Inductively coupled plasma mass spectrometry (ICP-MS) measurement

The elemental composition of the $MnFe_2O_4$ NPs and the NP concentration in solution were measured by ICP-MS. The NP sample was prepared with the following protocol for ICP-MS measurements. Briefly, 10 μL of $MnFe_2O_4$ NPs in organic solvent was added into a tube, the solvent was evaporated, and 400 μL of fresh prepared aqua regia (HCl/ HNO_3 =3:1 (v/v)) was injected for the digestion. During this time, the NP dissolved into small fragments. After 4 hours digestion, 9.6 mL of 2 % HCl solution was added to the tube. Addition of

the acids resulted in a 1000 times total dilution. Finally, the diluted solution was injected into the ICP-MS equipment (Agilent 7700) for measuring the content of manganese and iron. The result of the element concentration was provided in ppb (parts per billion, 1 ppb corresponds to 1 μg/L).

Table S1. The elemental composition of the NPs as analyzed by ICP-MS. $C_{(Fe)}$ and $C_{(Mn)}$ refer to the mass concentrations of Fe and Mn, respectively.

Sample material (in $CHCl_3$)	Fe (mg/mL)	Mn (mg/mL)	Total (mg/mL)	$C_{(Fe)}$: $C_{(Mn)}$
$MnFe_2O_4$ NPs	3.56	1.65	7.25	2.12

3. Characterization of $MnFe_2O_4$ NPs on the silicon

Manganese ferrite nanoparticles on the silicon (NPOS) were characterized by scanning electron microscopy (SEM, FEI-Sirion 200). The $MnFe_2O_4$ NPs layer was obvious, as shown in Figure S2.
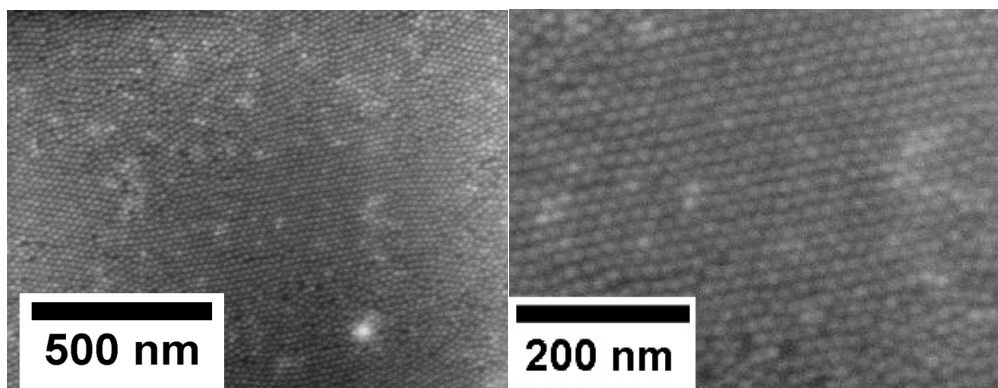

Figure S2. SEM images of $MnFe_2O_4$ NPs on the substrate.

4. Amplitude transmissions measurements based on different types of NPs

In this experiment, a series of NPs of materials others than $MnFe_2O_4$ were studied as comparison. Herein, we investigated four different types of NPs as control group to confirm the importance of the combination of

elements concerning the modification of THz antennas. The control samples were silver nanoparticles (Ag NPs, $d_c \approx 12$ nm), iron oxide nanoparticles (Fe$_3$O$_4$ NPs, $d_c \approx 27$ nm), titanium dioxide nanoparticles (TiO$_2$ NPs, $d_c \approx$ 11 nm), and gold nanoparticles (Au NPs, $d_c \approx 16$ nm), respectively. The core diameters d_c of all samples were determined by transmission electron microscopy (TEM).

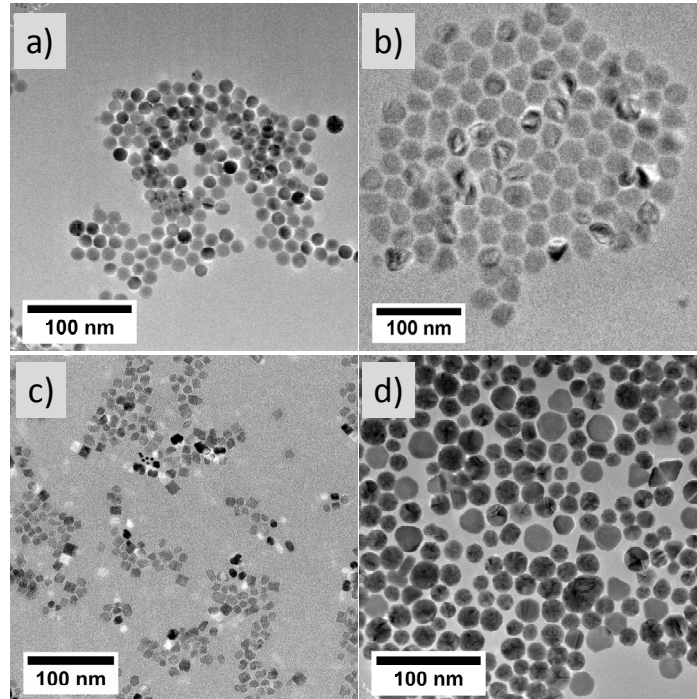**Figure S3.** TEM images of four different types of NPs. a) Ag NPs; b) Fe$_3$O$_4$ NPs; c) TiO$_2$ NPs and d) Au NPs. All the samples were dispersed in chloroform before the actual TEM measurements carried out in vacuum. The scale bars indicate 100 nm.
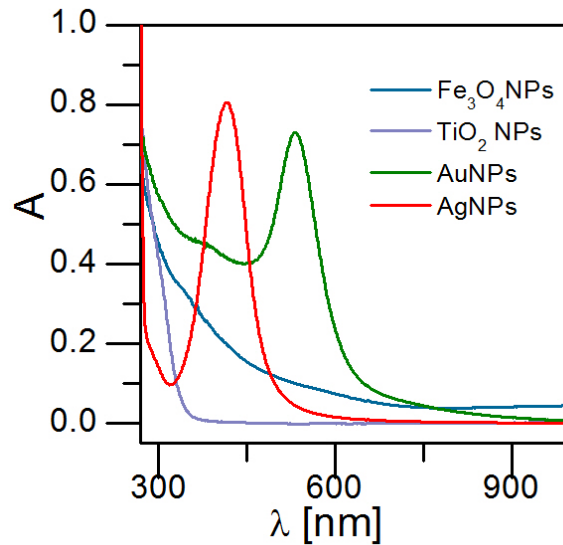
Figure S4. UV-Vis absorption spectra of four different types of NPs dispersed in chloroform: Fe_3O_4 NPs, TiO_2 NPs, Au NPs, and Ag NPs. From the spectra one can see that none of the samples has specific absorption at 808 nm, which means that there is no signal interference with the terahertz amplitude transmission experiments.

With the same fabrication process as used for the $MnFe_2O_4$ NPs, the four different types of NPs were immobilized with same molar concentration on silicon substrates in order to achieve Ag NPs on silicon, Fe_3O_4 NPs on silicon, TiO_2 NPs on silicon, and Au NPs on silicon, respectively. These four substrates immobilized with the different types of nanomaterials were tested concerning the transmissions of THz pulses. As a result transmission was found to be almost identical and constant ($T \approx 1$) with increasing the power of laser irradiation, similar as recorded for $MnFe_2O_4$ NPs on silicon. Afterwards, under laser irradiation with different powers, THz amplitude transmissions through silicon coated with the five different types of NPs (Ag NPs, Fe_3O_4 NPs, TiO_2 NPs, Au NPs, and $MnFe_2O_4$ NPs), as well as through a bare silicon substrate, were measured by using terahertz time-domain spectroscopy (THz-TDS) in transmission modes. Under laser irradiation with different powers the THz amplitude transmissions through the four control samples (silicon coated with Ag NPs, Fe_3O_4 NPs, TiO_2 NPs and Au NPs), as well as for the bare silicon, slightly decreased with increasing laser power from zero to 1.4 W (shown in Figure S5). However, the THz amplitude transmission through silicon coated with $MnFe_2O_4$ NPs was sharply decreased with increasing laser power, whereby the transmission value

dropped to a minimum under the laser power of about 0.34 W. These experimental results demonstrated that within 5 different NP materials tested, the MnFe$_2$O$_4$ NPs had the best performance on enhancing the surface carrier concentration.

All the samples as investigated above contained metals (Ti, Ag, Au, Fe and Mn). The work function of metal materials on top of semiconductors can influence the band structure of the semiconductor at the interface between metal and semiconductor.[1-5] When the work function of a metal is lower than that of an adjacent semiconductor ($W_m < W_s$), many electron carriers are accumulated at the interface. The accumulated carriers induce an increased carrier density at the interface in the semiconductor, resulting in enhancement of the conductivity along the semiconductor surface.[1-5] In comparison with the work functions of the other investigated materials, the work function of Mn (W_{Mn}) is the lowest, as shown in Figure S6. In this case, the work function of Mn is lower than that of silicon ($W_{Mn} < W_{si}$). W_{Mn} is of influence for the work function of MnFe$_2$O$_4$. In addition, the work function of GaAs was described in reference.[6] When a material contacts a semiconductor, the work function of contacted material is one factor which affects the change of band structure of the semiconductor. However, according to some references,[1,2,4,5,7,8] the surface state of contacted material is another key factor affecting change of band structure of semiconductors. In the nano region, surface states of nanomaterials (such as NPs) have a significant effect on surface electrical properties of semiconductors. Surface states of nanoparticles originate from the surface atoms of NPs, which present weak and unsaturated bonding states, which drastically influence their surface properties. The different NPs have different surface states, which resulted in different effects on semiconductors. The surface state of MnFe$_2$O$_4$ NPs perhaps has a significant effect on the semiconductor substrate. In conclusion, MnFe$_2$O$_4$ NPs can provide more enhancement of the conductivity along the semiconductor surface as compared to the other NPs investigate here. Therefore, we chose MnFe$_2$O$_4$ NPs in this study for all detailed measurements.
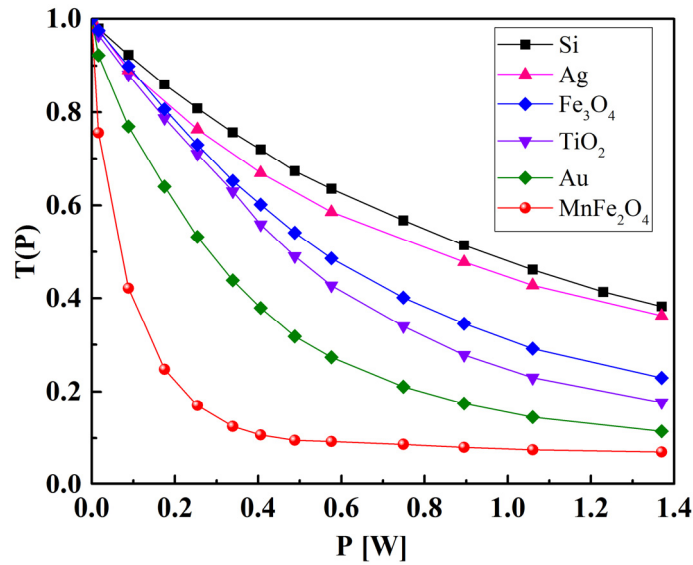
Figure S5. Amplitude transmissions of the terahertz pulses transmitted through the silicon coated with NPs and the bare silicon under laser irradiation with different powers P, respectively.
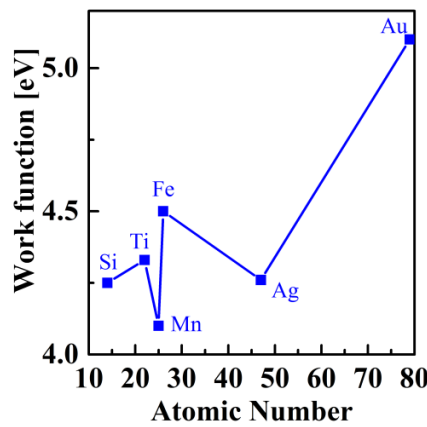
Figure S6. Work functions of materials [1-5]

Besides, in order to exclude the effect of magnetic response of NPs on the surface photoconductivity of the semiconductors, different composite magnetic nanoparticles (NPs) with similar size were compared, including $MnFe_2O_4$ NPs, Fe_3O_4 NPs and $CoFe_2O_4$ NPs. From Figure S7 we can see, all of them exhibit excellent monodispersity with uniform size around 15 nm, and the M-H curves showed superparamagnetic behaviour with similar smooth loops. The saturation magnetization (Ms) of $MnFe_2O_4$ NPs is a little bit higher than the

others; while, the THz transmission measurement based on $MnFe_2O_4$ NPs present significantly improvement compared to other two types of magnetic NPs, as shown in Figure S8. Therefore, the influence of magnetic response of nanoparticles on surface photoconductivity of the semiconductors seems negligible.
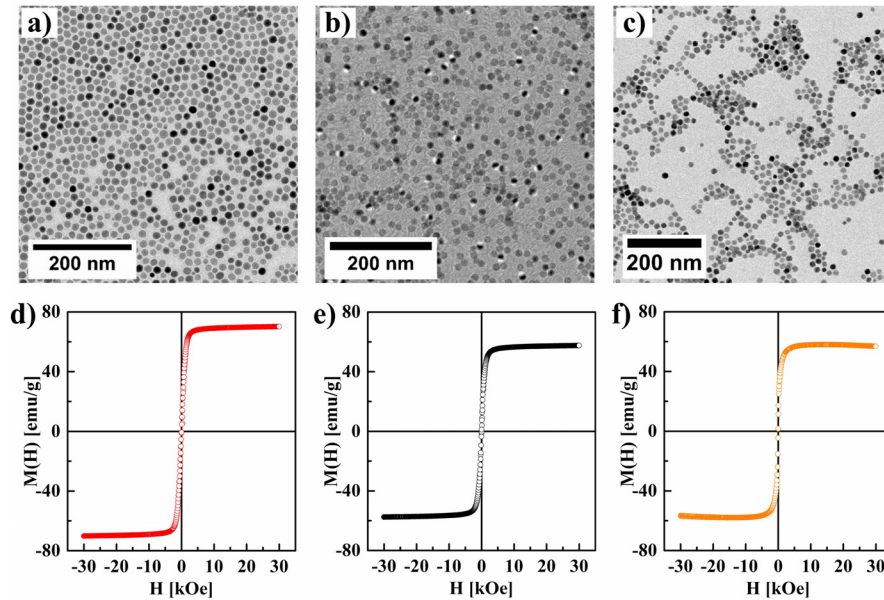
Figure S7. TEM images of three magnetic NPs. a) $MnFe_2O_4$ NPs; b) Fe_3O_4 NPs and c) $CoFe_2O_4$ NPs. All the samples were dispersed in chloroform before the actual TEM measurements carried out in vacuum. Magnetization versus magnetic field M(H) curve of three magnetic NPs, d) $MnFe_2O_4$ NPs; e) Fe_3O_4 NPs and f) $CoFe_2O_4$ NPs, measured at 300 K using a SQUID magnetometer.
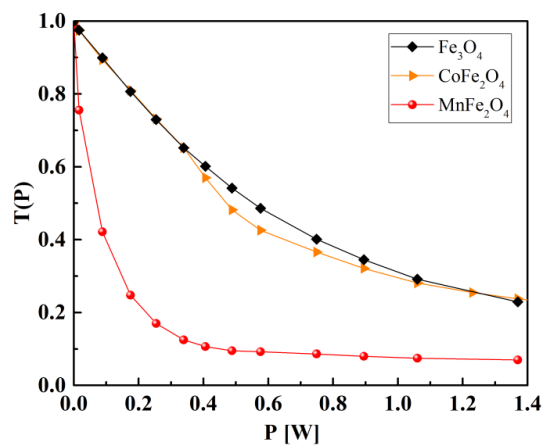
Figure S8. Amplitude transmissions of the terahertz pulses transmitted through the silicon coated with NPs ($MnFe_2O_4$ NPs, Fe_3O_4 NPs and $CoFe_2O_4$ NPs) under laser irradiation with different powers P, respectively.

5. Proposed theory: simulations based on band bending induced by MnFe$_2$O$_4$ NPs on silicon.

To account for the effect MnFe$_2$O$_4$ NPs on silicon in our observations, we propose the following model. When the silicon substrate is under laser irradiation, the volume of photo-excited carriers is defined by the irradiated area and the penetration depth of the laser beam. To account for the optical properties of the silicon under laser irradiation, the silicon can approximately be divided into a conducting layer and a lossless layer. Hereby, the thickness of the conducting layer is defined by the penetration depth of the laser beam, and the thickness of the lossless layer is defined by the part of the substrate with no laser irradiation. When the silicon is under laser irradiation, a carrier gradient exists between the surface and the interior part of the silicon, which can change the energy band structure of the interface between air and silicon. Therefore, photo-excited carriers in the silicon substrate diffuse from the surface into the interior to reach an equilibrium state.[1-5] Meanwhile, the photo-excited carriers induce a change of conductivity in the conducting layer of silicon. The optical system of NPOS substrates under laser irradiation can be approximately divided into a lossless layer of the silicon and a conducting layer consisting of the NPs and the photo-doped silicon layer. In the aforementioned experiment, the wavelength of the CW laser irradiating samples was 808 nm. According to the absorption spectrum of the MnFe$_2$O$_4$ NPs in Figure 1c, there was no apparent absorption of the MnFe$_2$O$_4$ NPs at 808 nm, so that the number of photo-excited carriers from the MnFe$_2$O$_4$ NPs was negligible. Therefore, the conductivity of NPOS substrates under laser irradiation is mainly dominated by the conductivity of the conducting layer in the silicon.[2,4,9] However, the surface atoms of the MnFe$_2$O$_4$ NPs present an unsaturated bonding state and have high chemical potential.[10-12] These surface atoms of the MnFe$_2$O$_4$ NPs change the energy band structure of the interface between the MnFe$_2$O$_4$ NPs and the silicon. The surface state of the MnFe$_2$O$_4$ NPs directly causes band bending of the interface between NPs and silicon. It also influences the quasi-Fermi level splitting in NPOS substrates under laser irradiation. Due to the effect of the surface states of the MnFe$_2$O$_4$ NPs, the diffusion of the photo-excited carriers in the silicon is more restricted to the surface, than in the case of substrates without NPs. The photo-excited carriers in silicon mainly accumulate at the interface between the MnFe$_2$O$_4$ NPs and silicon. The accumulated carriers induce an increased photo-carrier density on the interface between the MnFe$_2$O$_4$ NPs and silicon, resulting in enhancement of the conductivity on the silicon surface. In the

comparison with NPOS substrates, the photo-excited carriers of bare silicon substrates mostly diffuse from the surface into the interior because of the existence of a carrier gradient between surface and interior in the bare silicon. Therefore, under laser irradiation with the same power, the conductivity of the conducting layer in the bare silicon is much lower than that of the conducting layer in NPOS substrates. Actually, the conducting layer in the bare silicon is much thicker than that in NPOS substrates. However, photo-excited carriers of the bare silicon mostly diffuse from the surface into the interior, and a part of photo-excited carriers decay in the diffusion process. Hence, the part of the conducting layer in the bare silicon, which exceeds the thickness of the conducting layer in NPOS substrates, has low conductivity and could be almost negligible. Therefore, the thickness of the conducting layer of the NPOS substrate and the bare silicon could be approximately same in the simulations.

In the model for NPOS substrates under laser irradiation, the electrical properties of silicon can be described by holes in the valence band and electrons in the conduction band.[2,5] Concentrations of holes and electrons are dominated by the quasi-Fermi levels of holes and electrons in the quasi-thermal equilibrium. In terms of the quasi-Fermi levels of holes and electrons, the conductivity σ in silicon can be written as:

$$\sigma = e \cdot (\mu_n + \mu_p) \cdot n_i \cdot e^{\frac{\Delta E_{n,h}}{2 \cdot K_B T}}$$

Where e is the electron charge, μ_n is the mobility of electrons, μ_p is the mobility of holes, n_i is intrinsic carrier concentration of silicon, $\Delta E_{n,h}$ is the separation energy ($\Delta E_{n,h} = E_{Fn} - E_{Fh}$) between the electron quasi-Fermi level E_{Fn} and hole the quasi-Fermi level E_{Fh}, K_B is the Boltzmann constant, and T is the Kelvin temperature, respectively.

Quasi-Fermi levels: describes the populations of electrons are displaced from equilibrium in each the conduction - valence bands, caused by the external voltage, or exposure to light of energy (E>Eg).
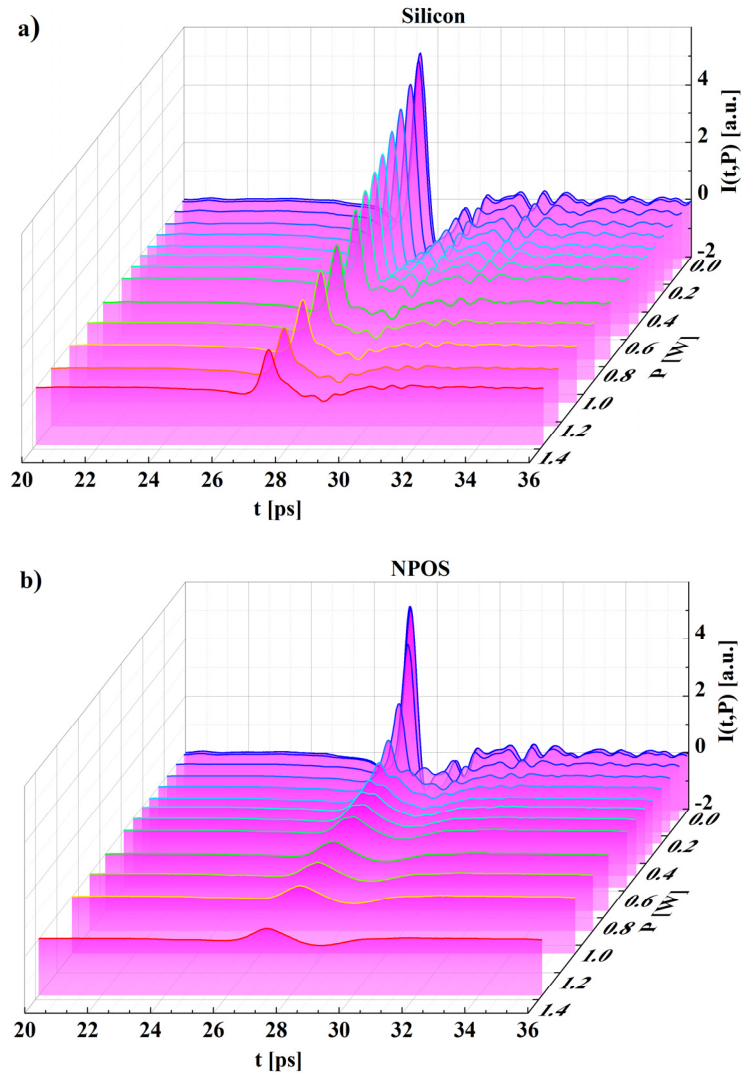
Figure S9. Waveforms of the THz pulses transmitted through the silicon and NPOS under the laser irradiation with different powers.

6. Numerical Methods

The simulations of the proposed model were performed by electromagnetic simulation software. We chose the thickness of the conducting layer of the silicon defined by the penetration depth of the laser beam, which was about 5 μm. The thickness of the lossless layer of silicon was 510 μm. In that way, the total thickness of the silicon used in the experiment consists of the thicknesses of the conducting layer and the lossless layer of silicon. By this means, we determined the silicon conductivity with dependence on the laser beam power. The

parameters of silicon are from the literature values: $\mu_n = 1400 \text{ cm}^2 / (\text{V} \cdot \text{s})$, $\mu_p = 450 \text{ cm}^2 / (\text{V} \cdot \text{s})$,

$N_c = 3.22 \times 10^{19} \text{ cm}^{-3}$, $N_v = 1.83 \times 10^{19} \text{ cm}^{-3}$ and $E_g = 1.12 \text{ eV}$ for silicon at room temperature.

References

1 Neamen, D. *Semiconductor Physics And Devices*. (McGraw-Hill, Inc., 2002).

2 Kittel, C. *Introduction to solid state physics*. (Wiley, 2004).

3 Young, C. D. Exploring terahertz pulse enhancement through gold nanoparticle deposition. *Dissertations & Theses - Gradworks* (2009).

4 Fox, M. *Optical properties of solids*. Vol. 3 (Oxford University Press, 2010).

5 Sze, S. M. *Semiconductor devices: physics and technology*. (John Wiley & Sons, 2008).

6 Haneman, D. Photoelectric emission and work functions of InSb, GaAs, Bi_2Te_3 and germanium. *Journal of Physics & Chemistry of Solids* **11**, 205,IN201,209-208,IN202,214 (1959).

7 Grundmann, M. *The physics of semiconductors:an introduction including Nanophysics and applications*. (Springer, 2014).

8 Sze, S. M. & Mattis, D. C. *Physics of Semiconductor Devices*. (Wiley-Interscience, 2007).

9 Weis, P. *et al.* Spectrally Wide-Band Terahertz Wave Modulator Based on Optically Tuned Graphene. *Acs Nano* **6**, 9118-9124 (2012).

10 Antonov, V. N., Harmon, B. N. & Yaresko, A. N. Electronic structure and x-ray magnetic circular dichroism in Fe3O4 and Mn-, Co-, or Ni-substituted Fe3O4. *Phys Rev B* **67** (2003).

11 Bateer, B. *et al.* Synthesis, size and magnetic properties of controllable MnFe2O4 nanoparticles with versatile surface functionalities. *Dalton T* **43**, 9885-9891 (2014).

12 Singh, D. J., Gupta, M. & Gupta, R. First-principles investigation of MnFe2O4. *Phys Rev B* **65** (2002).

Bibliography

[1] Lee Yun-Shik. Principles of terahertz science and technology. *NY: Springer*, pages 105–122, 2008.

[2] Andrew D Jameson. *Generating and using terahertz radiation to explore carrier dynamics of semiconductor and metal nanostructures*. PhD thesis, 2012.

[3] Jin Keun Seo, Eung Je Woo, Ulrich Katscher, and Yi Wang. *Electro-magnetic tissue properties MRI*, volume 1. World Scientific, 2014.

[4] Belén Andrés García. Enhancing the radiated power in the terahertz band. 2013.

[5] B Knoll, F Keilmann, A Kramer, and R Guckenberger. Contrast of microwave near-field microscopy. *Applied physics letters*, 70(20):2667–2669, 1997.

[6] Don Arnone, Craig Ciesla, and Michael Pepper. Terahertz imaging comes into view. *Physics World*, 13(4):35, 2000.

[7] AG Markelz, A Roitberg, and Edwin J Heilweil. Pulsed terahertz spectroscopy of dna, bovine serum albumin and collagen between 0.1 and 2.0 thz. *Chemical Physics Letters*, 320(1):42–48, 2000.

[8] M Walther, B Fischer, M Schall, H Helm, and P Uhd Jepsen. Far-infrared vibrational spectra of all-trans, 9-cis and 13-cis retinal measured by thz time-domain spectroscopy. *Chemical Physics Letters*, 332(3):389–395, 2000.

[9] Gilad Haran, Wei-Dong Sun, Klaas Wynne, and Robin M Hochstrasser. Femtosecond far-infrared pump-probe spectroscopy: a new tool for studying low-frequency vibrational dynamics in molecular condensed phases. *Chemical physics letters*, 274(4):365–371, 1997.

[10] JT Kindt and CA Schmuttenmaer. Far-infrared dielectric properties of polar liquids probed by femtosecond terahertz pulse spectroscopy. *The Journal of Physical Chemistry*, 100(24):10373–10379, 1996.

[11] Daniel M Mittleman, Rune Hylsberg Jacobsen, Ramesh Neelamani, Richard G Baraniuk, and Martin C Nuss. Gas sensing using terahertz time-domain spectroscopy. *Applied Physics B: Lasers and Optics*, 67(3):379–390, 1998.

[12] Ali Mazin Abdul-Munaim, Marco Reuter, Oday Mazin Abdulmunem, Jan C Balzer, Martin Koch, and Dennis G Watson. Using terahertz time-domain spectroscopy to discriminate among water contamination levels in diesel engine oil. *Transactions of the ASABE*, 59(3), 2016.

[13] Aurele JL Adam, Paul CM Planken, Sabrina Meloni, and Joris Dik. Terahertz imaging of hidden paint layers on canvas. *Optics Express*, 17(5):3407–3416, 2009.

[14] Payam Mousavi, Frank Haran, David Jez, Fadil Santosa, and John Steven Dodge. Simultaneous composition and thickness measurement of paper using terahertz time-domain spectroscopy. *Applied optics*, 48(33):6541–6546, 2009.

[15] D Banerjee, W Von Spiegel, MD Thomson, S Schabel, and HG Roskos. Diagnosing water content in paper by terahertz radiation. *Optics Express*, 16(12):9060–9066, 2008.

[16] VP Wallace, AJ Fitzgerald, S Shankar, N Flanagan, R Pye, J Cluff, and DD Arnone. Terahertz pulsed imaging of basal cell carcinoma ex vivo and in vivo. *British Journal of Dermatology*, 151(2):424–432, 2004.

[17] EP MacPherson. Biological applications of terahertz pulsed imaging and spectroscopy, 2005.

[18] Anthony J Fitzgerald, Vincent P Wallace, Mercedes Jimenez-Linan, Lynda Bobrow, Richard J Pye, Anand D Purushotham, and Donald D Arnone. Terahertz pulsed imaging of human breast tumors 1. *Radiology*, 239(2):533–540, 2006.

[19] David F Plusquellic, Karen Siegrist, Edwin J Heilweil, and Okan Esenturk. Applications of terahertz spectroscopy in biosystems. *ChemPhysChem*, 8(17):2412–2431, 2007.

[20] William R Tribe, David A Newnham, Philip F Taday, and Michael C Kemp. Hidden object detection: security applications of terahertz technology. In *Integrated Optoelectronic Devices 2004*, pages 168–176. International Society for Optics and Photonics, 2004.

[21] DM Mittleman, M Gupta, Ramesh Neelamani, RG Baraniuk, JV Rudd, and M Koch. Recent advances in terahertz imaging. *Applied Physics B*, 68(6):1085–1094, 1999.

[22] N Krumbholz, T Hochrein, N Vieweg, T Hasek, K Kretschmer, M Bastian, M Mikulics, and M Koch. Monitoring polymeric compounding processes inline with thz time-domain spectroscopy. *Polymer Testing*, 28(1):30–35, 2009.

[23] Yiwen Sun, Ming Yiu Sy, Yi-Xiang J Wang, Anil T Ahuja, Yuan-Ting Zhang, and Emma Pickwell-MacPherson. A promising diagnostic method: Terahertz pulsed imaging and spectroscopy. *World journal of radiology*, 3(3):55, 2011.

[24] Carl Sagan and WW Kellogg. The terrestrial planets. *Annual review of astronomy and astrophysics*, 1(1):235–266, 1963.

[25] Richard T Hall and Jerome M Dowling. Pure rotational spectrum of water vapor. *The Journal of Chemical Physics*, 47(7):2454–2461, 1967.

[26] David H Auston. Picosecond optoelectronic switching and gating in silicon. *Applied Physics Letters*, 26(3):101–103, 1975.

[27] Alfred P DeFonzo and Charles R Lutz. Optoelectronic transmission and reception of ultrashort electrical pulses. *Applied Physics Letters*, 51(4):212–214, 1987.

[28] BB Hu, JT Darrow, X-C Zhang, DH Auston, and PR Smith. Optically steerable photoconducting antennas. *Applied physics letters*, 56(10):886–888, 1990.

[29] AS Weling, BB Hu, NM Froberg, and DH Auston. Generation of tunable narrow-band thz radiation from large aperture photoconducting antennas. *Applied physics letters*, 64(2):137–139, 1994.

[30] Masahiko Tani, Osamu Morikawa, Shuji Matsuura, and Masanori Hangyo. Generation of terahertz radiation by photomixing with dual-and multiple-mode lasers. *Semiconductor Science and Technology*, 20(7):S151, 2005.

[31] Bradley Ferguson and Xi-Cheng Zhang. Materials for terahertz science and technology. *Nature materials*, 1(1):26–33, 2002.

[32] Rüdeger Köhler, Alessandro Tredicucci, Fabio Beltram, Harvey E Beere, Edmund H Linfield, A Giles Davies, David A Ritchie, Rita C Iotti, and Fausto Rossi. Terahertz semiconductor-heterostructure laser. *Nature*, 417(6885):156–159, 2002.

[33] Ronald Ulbricht, Euan Hendry, Jie Shan, Tony F Heinz, and Mischa Bonn. Carrier dynamics in semiconductors studied with time-resolved terahertz spectroscopy. *Reviews of Modern Physics*, 83(2):543, 2011.

[34] DH Auston. Subpicosecond electro-optic shock waves. *Applied Physics Letters*, 43(8):713–715, 1983.

[35] David H Auston, KP Cheung, JA Valdmanis, and DA Kleinman. Cherenkov radiation from femtosecond optical pulses in electro-optic media. *Physical Review Letters*, 53(16):1555, 1984.

[36] Peter R Smith, David H Auston, and Martin C Nuss. Subpicosecond photoconducting dipole antennas. *IEEE Journal of Quantum Electronics*, 24(2):255–260, 1988.

[37] Ch Fattinger and D Grischkowsky. Terahertz beams. *Applied Physics Letters*, 54(6):490–492, 1989.

[38] Shantanu Gupta, John F Whitaker, and Gerard A Mourou. Ultrafast carrier dynamics in iii-v semiconductors grown by molecular-beam epitaxy at very low substrate temperatures. *IEEE Journal of Quantum Electronics*, 28(10):2464–2472, 1992.

[39] RW Wood. A suspected case of the electrical resonance of minute metal particles for light-waves. a new type of absorption. *Proceedings of the Physical Society of London*, 18(1):166, 1902.

[40] RH Ritchie. Surface plasmons in solids. *Surface Science*, 34(1):1–19, 1973.

[41] S Pillai and MA Green. Plasmonics for photovoltaic applications. *Solar Energy Materials and Solar Cells*, 94(9):1481–1486, 2010.

[42] D Grischkowsky, Søren Keiding, Martin Van Exter, and Ch Fattinger. Far-infrared time-domain spectroscopy with terahertz beams of dielectrics and semiconductors. *JOSA B*, 7(10):2006–2015, 1990.

[43] Daniel M Mittleman, Rune H Jacobsen, and Martin C Nuss. T-ray imaging. *IEEE Journal of selected topics in quantum electronics*, 2(3):679–692, 1996.

[44] Daniel M Mittleman, Stefan Hunsche, Luc Boivin, and Martin C Nuss. T-ray tomography. *Optics letters*, 22(12):904–906, 1997.

[45] JM Chamberlain. Where optics meets electronics: recent progress in decreasing the terahertz gap. *Philosophical Transactions of the Royal Society of London A: Mathematical, Physical and Engineering Sciences*, 362(1815):199–213, 2004.

[46] Masayoshi Tonouchi. Cutting-edge terahertz technology. *Nature photonics*, 1(2):97–105, 2007.

[47] P Uhd Jepsen, David G Cooke, and Martin Koch. Terahertz spectroscopy and imaging–modern techniques and applications. *Laser & Photonics Reviews*, 5(1):124–166, 2011.

[48] DH Auston and PR Smith. Generation and detection of millimeter waves by picosecond photoconductivity. *Applied Physics Letters*, 43(7):631–633, 1983.

[49] D Auston. Impulse response of photoconductors in transmission lines. *IEEE Journal of Quantum Electronics*, 19(4):639–648, 1983.

[50] DH Auston, KP Cheung, and PR Smith. Picosecond photoconducting hertzian dipoles. *Applied physics letters*, 45(3):284–286, 1984.

[51] Lionel Duvillaret, Frederric Garet, and J-L Coutaz. A reliable method for extraction of material parameters in terahertz time-domain spectroscopy. *IEEE Journal of selected topics in quantum electronics*, 2(3):739–746, 1996.

[52] Masaya Nagai, Koichiro Tanaka, Hideyuki Ohtake, Toshiaki Bessho, Toshiharu Sugiura, Tomoya Hirosumi, and Makoto Yoshida. Generation and detection of terahertz radiation by electro-optical process in gaas using 1.56 μ m fiber laser pulses. *Applied physics letters*, 85(18):3974–3976, 2004.

[53] Oday Mazin Abdulmunem, Norman Born, Martin Mikulics, Jan Christof Balzer, Martin Koch, and Sascha Preu. High accuracy terahertz time-domain system for reliable characterization of photoconducting antennas. *Microwave and Optical Technology Letters*, 59(2):468–472, 2017.

[54] P Uhd Jepsen, Rune Hylsberg Jacobsen, and SR Keiding. Generation and detection of terahertz pulses from biased semiconductor antennas. *JOSA B*, 13(11):2424–2436, 1996.

[55] Zhisheng Piao, Masahiko Tani, and Kiyomi Sakai. Carrier dynamics and terahertz radiation in photoconductive antennas. *Japanese Journal of Applied Physics*, 39(1R):96, 2000.

[56] Daniela Dragoman and Mircea Dragoman. Terahertz fields and applications. *Progress in Quantum Electronics*, 28(1):1–66, 2004.

[57] G Rodriguez and AJ Taylor. Screening of the bias field in terahertz generation from photoconductors. *Optics letters*, 21(14):1046–1048, 1996.

[58] JE Pedersen, VG Lyssenko, JM Hvam, P Uhd Jepsen, SR Keiding, CB So/rensen, and PE Lindelof. Ultrafast local field dynamics in photoconductive thz antennas. *Applied physics letters*, 62(11):1265–1267, 1993.

[59] AC Warren, JM Woodall, JL Freeouf, D Grischkowsky, DT McInturff, MR Melloch, and N Otsuka. Arsenic precipitates and the semi-insulating properties of gaas buffer layers grown by low-temperature molecular beam epitaxy. *Applied Physics Letters*, 57(13):1331–1333, 1990.

[60] MR Melloch, JM Woodall, ES Harmon, N Otsuka, F Pollak, DD Nolte, RM Feenstra, and MA Lutz. Annual review of material science. 1995.

[61] LG Lavrent'eva, MD Vilisova, VV Preobrazhenskii, and VV Chaldyshev. Low-temperature molecular-beam epitaxy of gaas: effect of excess arsenic on the structure and properties of the gaas layers. *Russian physics journal*, 45(8):735–752, 2002.

[62] AI Veinger, SV Kozyrev, VV Chaldyshev, MD Vilisova, LG Lavrenteva, IV Ivonin, DI Lubyshev, VV Preobrazhenskii, and BR Semyagin. Magnet-dependent microwave absorption caused by superconducting in-ga-clusters in gaas grown by molecular-ray epitaxy. *FIZIKA TVERDOGO TELA*, 38(10):2897–2904, 1996.

[63] MR Melloch, N Otsuka, JM Woodall, AC Warren, and JL Freeouf. Formation of arsenic precipitates in gaas buffer layers grown by molecular beam epitaxy at low substrate temperatures. *Applied physics letters*, 57(15):1531–1533, 1990.

[64] Bijan Tadayon, Mohammad Fatemi, Saied Tadayon, F Moore, and Harry Dietrich. Electrical characterization of low temperature gaas layers, and observation of the extremely large carrier concentrations in undoped material. *Journal of Vacuum Science & Technology B: Microelectronics and Nanometer Structures Processing, Measurement, and Phenomena*, 10(3):1074–1077, 1992.

[65] OM Abdulmunem, KI Hassoon, J Völkner, M Mikulics, KI Gries, and JC Balzer. Photoconductive lt-gaas terahertz antennas: Correlation between surface quality and emission strength. *Journal of Infrared, Millimeter, and Terahertz Waves*, 38(5):574–582, 2017.

[66] Jean-Philippe Sylvestre, Suzie Poulin, Andrei V Kabashin, Edward Sacher, Michel Meunier, and John HT Luong. Surface chemistry of gold nanoparticles produced by laser ablation in aqueous media. *The Journal of Physical Chemistry B*, 108(43):16864–16869, 2004.

[67] Weien Lai, Oday Mazin Abdulmunem, Pablo Del Pino, Beatriz Pelaz, Wolfgang J Parak, Qian Zhang, and Huaiwu Zhang. Enhanced terahertz radiation generation of photoconductive antennas based on manganese ferrite nanoparticles. *Scientific Reports*, 7, 2017.

[68] Koichi Sasaki and Noriharu Takada. Liquid-phase laser ablation. *Pure and Applied Chemistry*, 82(6):1317–1327, 2010.

[69] Anne Hahn, Stephan Barcikowski, and Boris N Chichkov. Influences on nanoparticle production during pulsed laser ablation. *Pulse*, 40(45):50, 2008.

[70] NV Tarasenko, VS Burakov, and AV Butsen. Laser ablation plasmas in liquids for fabrication of nanosize particles. *Publications de l'Observatoire Astronomique de Beograd*, 82:201–211, 2007.

[71] Mihai Stafe, C Negutu, Niculae N Puscas, and IM Popescu. Pulsed laser ablation of solids. *Rom. Rep. Phys*, 62(4), 2010.

[72] Anagha Avinash Bhakay. *Preparation of Nanovehicles for Targeted Drug Delivery*. PhD thesis, New Jersey Institute of Technology, Otto H. York Department of Chemical, Biological and Pharmaceutical Engineering, 2009.

[73] S Iravani, H Korbekandi, SV Mirmohammadi, and B Zolfaghari. Synthesis of silver nanoparticles: chemical, physical and biological methods. *Research in pharmaceutical sciences*, 9(6):385, 2014.

[74] E Axente, M Barberoglou, PG Kuzmin, E Magoulakis, PA Loukakos, E Stratakis, GA Shafeev, and C Fotakis. Size distribution of au nps generated by laser ablation of a gold target in liquid with time-delayed femtosecond pulses. *arXiv preprint arXiv:1008.0374*, 2010.

[75] Kuk Ki Kim, Daehyun Kim, Sang Kyu Kim, Seung Min Park, and Jae Kyu Song. Formation of zno nanoparticles by laser ablation in neat water. *Chemical Physics Letters*, 511(1):116–120, 2011.

[76] Daria Riabinina, Jianming Zhang, Mohamed Chaker, Joëlle Margot, and Dongling Ma. Size control of gold nanoparticles synthesized by laser ablation in liquid media. *ISRN Nanotechnology*, 2012, 2012.

[77] Davoud Dorranian, Shiva Tajmir, and Farzane Khazanehfar. Effect of laser fluence on the characteristics of ag nanoparticles produced by laser ablation. *Soft Nanoscience Letters*, 2013, 2013.

[78] Renata Pasqualini. *Tissue-specific vascular endothelial signals and vector targeting*, volume 69. Academic Press, 2010.

[79] Dorian Hanaor, Marco Michelazzi, Cristina Leonelli, and Charles C Sorrell. The effects of carboxylic acids on the aqueous dispersion and electrophoretic deposition of zro 2. *Journal of the European Ceramic Society*, 32(1):235–244, 2012.

[80] Bruce J Berne and Robert Pecora. *Dynamic light scattering: with applications to chemistry, biology, and physics*. Courier Corporation, 2000.

[81] Jessica Rodríguez-Fernández, Jorge Pérez-Juste, Luis M Liz-Marzán, and Peter R Lang. Dynamic light scattering of short au rods with low aspect ratios. *The Journal of Physical Chemistry C*, 111(13):5020–5025, 2007.

[82] Mélanie Auffan, Jérôme Rose, Jean-Yves Bottero, Gregory V Lowry, Jean-Pierre Jolivet, and Mark R Wiesner. Towards a definition of inorganic nanoparticles from an environmental, health and safety perspective. *Nature nanotechnology*, 4(10):634–641, 2009.

[83] Prashant K Jain, Xiaohua Huang, Ivan H El-Sayed, and Mostafa A El-Sayed. Review of some interesting surface plasmon resonance-enhanced properties of noble metal nanoparticles and their applications to biosystems. *Plasmonics*, 2(3):107–118, 2007.

[84] Robert Williams Wood. On a remarkable case of uneven distribution of light in a diffraction grating spectrum. *Proceedings of the Physical Society of London*, 18(1):269, 1902.

[85] GKP Ramanandan, G Ramakrishnan, N Kumar, AJL Adam, and PCM Planken. Emission of terahertz pulses from nanostructured metal surfaces. *Journal of Physics D: Applied Physics*, 47(37):374003, 2014.

[86] Anthony Mark Fox. *Optical Properties of Solids*, volume 3. Oxford University Press, USA, 2003.

[87] Xuanhua Li, Jinmeng Zhu, and Bingqing Wei. Hybrid nanostructures of metal/two-dimensional nanomaterials for plasmon-enhanced applications. *Chemical Society Reviews*, 45(11):3145–3187, 2016.

[88] CF Bohren, DR Huffman, and Z Kam. Book-review-absorption and scattering of light by small particles. *Nature*, 306:625, 1983.

[89] Uwe Kreibig and Michael Vollmer. *Optical properties of metal clusters*, volume 25. Springer Science & Business Media, 1995.

[90] Olivier Pluchery. Optical properties of gold nanoparticles. *Gold Nanoparticles for Physics, Chemistry and Biology*, pages 51–54, 2012.

[91] Mark Fox. *Optical Properties of Solids*, volume 3. Oxford University Press, 2010.

[92] Oday Abdulmunem, Khaleel Hassoon, Mahmoud Gaafar, Arash Rahimi-Iman, and Jan C Balzer. Tin nanoparticles for enhanced thz generation in tds systems. *Journal of Infrared, Millimeter, and Terahertz Waves*, 38(10):1206–1214, 2017.

[93] Harry A Atwater and Albert Polman. Plasmonics for improved photovoltaic devices. *Nature materials*, 9(3):205–213, 2010.